Internal Electric Field Manipulation in Nanostructures

vorgelegt von
Master of Science
Sarah Kristina Schlichting
geb. in München

von der Fakultät II - Mathematik und Naturwissenschaften
der Technischen Universität Berlin
zur Erlangung des akademischen Grades

Doktor der Naturwissenschaften
- Dr. rer. nat. –

genehmigte Dissertation

Promotionsausschuss:

Vorsitzender: Prof. Dr. M. Lehmann
Gutachter: Prof. Dr. A. Hoffmann
Gutachter: Prof. Dr. A. Waag

Tag der wissenschaftlichen Aussprache: 24.04.2018

Berlin 2018

Abstract

Recently, an unconventional approach [the so-called Internal-Field-Guarded-Active-Region Design (IFGARD)] for the elimination of the crystal polarization field induced quantum confined Stark effect (QCSE) in polar semiconductor heterostructures was developed. This thesis demonstrates by means of micro-photoluminescence techniques the successful tuning as well as the elimination of the QCSE in strongly polar $[000\bar{1}]$ wurtzite GaN/AlN nanodiscs causing a reduction of the exciton life times by up to four orders of magnitude. The IFGARD based elimination of the QCSE is independent of any specific crystal growth procedures. Furthermore, the cone-shaped geometry of the utilized nanowires (which embed the investigated IFGARD nanodiscs) facilitates the experimental differentiation between quantum confinement- and QCSE-induced emission energy shifts. Due to the IFGARD, both effects become independently adaptable.

Within the IFGARD nanodiscs, several exciton recombination pathways are determined. For the first time, an evolution from a biexponential decay process at the low energy luminescence flank of the NDs to a triexponential decay process on the high energy side of the ND luminescence is observed. This evolution becomes detectable due to the absence of the built-in polarization fields. By combining the results of scanning tunneling electron microscopy, µ-photoluminescence and temperature dependent time resolved photoluminescence measurements, the three recombination pathways are assigned to excitons in different types of nanodisc-monolayer-thickness fluctuations and surface states joined by relaxation processes.

Zusammenfassung

Kürzlich wurde ein unkonventioneller Ansatz, das sogenannte „Internal-Field-Guarded-Active-Region Design“ (IFGARD) für die Eliminierung des durch das Kristallpolarisationsfeld induzierten „quantum confined Stark effects“ (QCSE) in polaren Halbleiterheterostrukturen vorgestellt. Die vorliegende Arbeit demonstriert mithilfe von Mikro-Photolumineszenzmessungen die erstmalige, erfolgreiche, experimentelle Umsetzung des IFGARDs am Beispiel von stark polaren $[000\bar{1}]$ Wurtzit GaN/AlN Nanodisks. Durch die erfolgreiche Eliminierung des QCSE verkürzen sich die Exzitonenlebensdauern um bis zu vier Größenordnungen. Dabei erfordert die auf IFGARD basierende Aufhebung des QCSE keine neuartigen oder anspruchsvolleren Kristallwachstumsprozeduren. Außerdem ermöglicht die Trichterform der untersuchten Nanodrähte (welche die IFGARD Nanodisks beinhalten) die experimentelle Differenzierung der durch das „quantum Confinement“- oder durch den QCSE induzierten Energieverschiebung der Nanodiskemission. Durch das IFGARD werden beide Effekte erstmalig voneinander unabhängig anpassbar.

In den Nanodisks wurden mehrere, unterschiedliche exzitonische Rekombinationskanäle nachgewiesen. Dabei konnten erstmalig Übergänge von einem biexponentiellen Verhalten der Zerfallstransienten, die auf der niederenergetischen Seite der Nanodisklumineszenz auftraten hin zu einem triexponentiellen Zerfall auf der hochenergetischen Seite der Nanodisklumineszenz beobachtet werden – eine Beobachtung, die durch die Abwesenheit der in konventionellen Proben inhärenten elektrischen Polarisationsfelder möglich wurde. Mithilfe kombinierter Charakterisierung der IFGARD-Proben durch Rastertunnelelektronenmikroskopie, µ-Photolumineszenz- und zeitaufgelöster µ-Photolumineszenzspektroskopie wurden die exzitonischen Rekombinationskanäle Ladugsträgern in unterschiedlichen Arten von Nanodiskdickenfluktuationen und Oberflächenzuständen in Kombination mit Relaxationsprozessen zugeordnet.

Content

1. Introduction 11
1.1 Thesis structure 12
2 AlN and GaN 14
2.1 Wurtzite crystal structure 14
2.2 Piezoelectric- and pyroelectric polarization 15
2.2.1 Quantum-confined Stark effect 17
2.2.2 Theoretical background 19
2.3 Band structure 23
3 Experimental methods 24
3.1 Micro-photoluminescence 24
3.2 Time-resolved photoluminescence 26
3.2.1 ns-range setup 26
3.2.2 µs-range setup 27
4 IFGARD 29
4.1.1 Original IFGARD 29
5 Samples 38
5.1 GaN/AlN-IFGARD nanodiscs [45] 38
5.2 Morphology of the NW samples [45] 39
6 Analysis and discussion 43
6.1 Micro-photoluminescence [45] 43
6.1.1 Estimation of the electric field strength [45] 49
6.1.2 Influence on the changing full width at half maximum 51
6.1.3 Power dependent photoluminescence [45] 62
6.1.4 Temperature dependent photoluminescence 69
6.2 Time-resolved photoluminescence 76
6.2.1 Temperature dependent time-resolved photoluminescence 77
6.2.2 Decay times as a function of the emitted ND luminescence 82
6.2.3 Multiexponential decay process 91
6.2.4 Fundamental differences in the transients for the quantum-confined Stark effect- and confinement regime [45] 94

6.3 IFGARD nanodiscs in comparison with “conventional” structures 96
7 Conclusion 99
7.1 Outlook 101
7.1.1 Interesting aspects and discussion for a real device 101
8 Publications and conference contributions 104
9 Acknowledgment/Danksagung 108
10 Bibliography 110
11 List of figures 119
12 List of tables 124

1. Introduction

Group-III-nitride semiconductors are key materials for visible and ultraviolet LEDs, LDs [1]–[3], and quantum-light sources [4]–[6]. In particular GaN as well as AlN favorably crystalize in the wurtzite crystal structure [7]. Hence, heterostructures based on these materials suffer from a strong electric field induced by a piezo- and pyroelectric polarization parallel to the most natural crystal growth direction [0001], the so called *c*-axis [8]–[12]. The polarization-induced internal fields cause a redshift of the exciton emission energy inside these heterostructures, known to be the prominent feature of the quantum-confined Stark effect (QCSE) [13]–[17], which is accompanied by a drastic decrease of the spatial electron-hole overlap in the direction of the *c*-axis [4], [9], [18]–[27]. Different approaches to eliminate or to diminish the electric field in group-III-nitride heterostructures (across the optically active region) have been investigated, such as growth on non- or semi-polar crystal planes [28], [29], forcing the growth of the cubic zinc blende phase [30], or by screening the fields with doping-induced free carriers [31]. Generally, approaches to avoid the preferential [0001] wurtzite crystal growth are challenging, slow, and they often produce a reduced crystal quality [32]–[37]. A more promising method to control the internal electric field is the Internal-Field-Guarded-Active-Region Design (IFGARD) [38], [39], theoretically developed by Hönig et al. [40]. As described in detail in chapter 4, a conventional structure of a GaN quantum well (QW) embedded in AlN barriers is complemented in the IFGARD structure by additional GaN guard layers enclosing the AlN barriers. This is not intuitive as the additional GaN guard layers reabsorb a particular percentage of the photons generated in the QW. But as shown in this thesis, the overall gain based on the elimination of the polarization field in the QW and the resulting boost in the exciton recombination probability, can overcompensate the reabsorption losses by the guard layers, if the thickness of the guard layer in the emission direction is smaller than $1/10^{th}$ of the emitted wavelength [41]–[44]. However, it was numerically demonstrated by Hönig et al. that IFGARD can lead to a constant piezo- and pyroelectric polarization potential inside of a QW, which results in flat conduction- and valence-band edges therein. This elimination of the electric field inside the QW results in a higher spatial overlap of the electron and hole wave functions, and hence in a drastic rise of the exciton recombination probability.

As calculated in Ref. [40] this maximized exciton recombination probability implicates a gain in the emitted single photons by 2 orders of magnitude.

It is important to note that the IFGARD approach does not require a change in the underlying conventional growth procedures; hence, no degradation of the crystal quality occurs as frequently observed for non- and semi-polar growth. Maintaining the initial crystal growth method is a big advantage of the present concept compared to any other alternative approaches that aim to reduce or even eliminate the internal polarization fields in semiconductor heterostructures [32]–[37].

This thesis shows the successful implementation of the IFGARD concept for the example of nanowires (NWs) containing GaN nanodiscs (NDs). In particular, this work demonstrates the reduction of the internal electric field inside of the GaN NDs down to zero, which reveals the advantage of the IFGARD over alternative, more conservative design concepts. Furthermore, the identification of the individual contributions of either the pure QCSE or the pure confinement effect based on two sample series with varying barrier and ND thickness gets possible.

Parts of this work have been published in [38], [40], [45]. Some section headers refer to [45], which means that these chapters comprise word-for-word contents of my first author publication, reference [45].

1.1 Thesis structure

The thesis is organized as follows: Chapter 2 starts with the basic properties of AlN and GaN including the wurtzite crystal structure, piezoelectric- and pyroelectric polarization, and band structure to give the reader the necessary fundamental knowledge to understand the advantages of IFGARD. In Chapter 3, a description of the used µ-photoluminescence (µ-PL) techniques is given followed by a detailed description of IFGARD in chapter 4. The description of IFGARD is divided into two cases: quantum dots (QDs) and quantum wells (QWs), followed in chapter 5 by the presentation of the investigated IFGARD NDs in NWs, which represent a hybrid between the laterally infinite QWs and the comparably slim QDs. The analysis and discussion of the recorded data are presented in chapter 6. This chapter is divided into three main parts: the µ-PL results, the TRPL results and the comparison to

literature values for polar as well as non-polar GaN QWs. A comparison of the experimental results with numeric simulations is content of the chapter 6.1. Finally, chapter 7 concludes und summarizes all results by showing an overview graph that comprises the most important key results determined for the investigated IFGARD NDs. Furthermore, chapter 7 includes an outlook. The outlook picks up some interesting issues concerning IFGARD. In this context, the right choice of the substrate, the reabsorption of photons in the top guard layer and the advantage of low current operated devices are discussed to convince, hopefully, even skeptical readers.

2 AlN and GaN

The aim of this chapter is to summarize the basic properties of GaN and AlN and the challenges that go along with those materials for the use in opto-electronic devices giving a good background knowledge to understand the results discussed in this thesis.

2.1 Wurtzite crystal structure

GaN as well as AlN preferably crystalize in the wurtzite structure [46], [47]. In principle, GaN and AlN may also crystalize with a zinc blende structure under certain conditions like high pressure, while GaN can also crystalize in the rock salt configuration. Although the unprefered crystal structures exhibit properties which may be useful as, e.g., in zinc blende crystal based hetero structures, the crystal polarization is not as detrimental as in wurtzite crystals [24], [48], [49], it needs an elaborate growth procedure that generates additional costs and challenges making the zinc blende crystal structure unsuitable for industrial use yet. Since the samples studied in this thesis exhibit the industrially more relevant wurtzite crystal structure, this chapter starts with the description of it.

The wurtzite crystal structure comprises two hexagonal close-packed layers of metal (here Al or Ga) and nitrogen ions, which are shifted relative to each other by 5/8 of the lattice constant *c*. Consequently, the crystal shows alternating layers of metal and nitrogen atoms, an ABAB stacking, exhibited in Figure 2.1. Thus, the wurtzite crystal belongs to the space group C_{6v}^4, point group C_{6v} and has a rotation symmetry of C_3 [50]. Furthermore, each metal atom is surrounded by four nitrogen atoms and vice versa, forming a tetrahedron with an angle of 109.47° (ideal wurtzite structure) between the nearest neighbors. The bonds are formed by sp^3- hybridized orbitals [50].

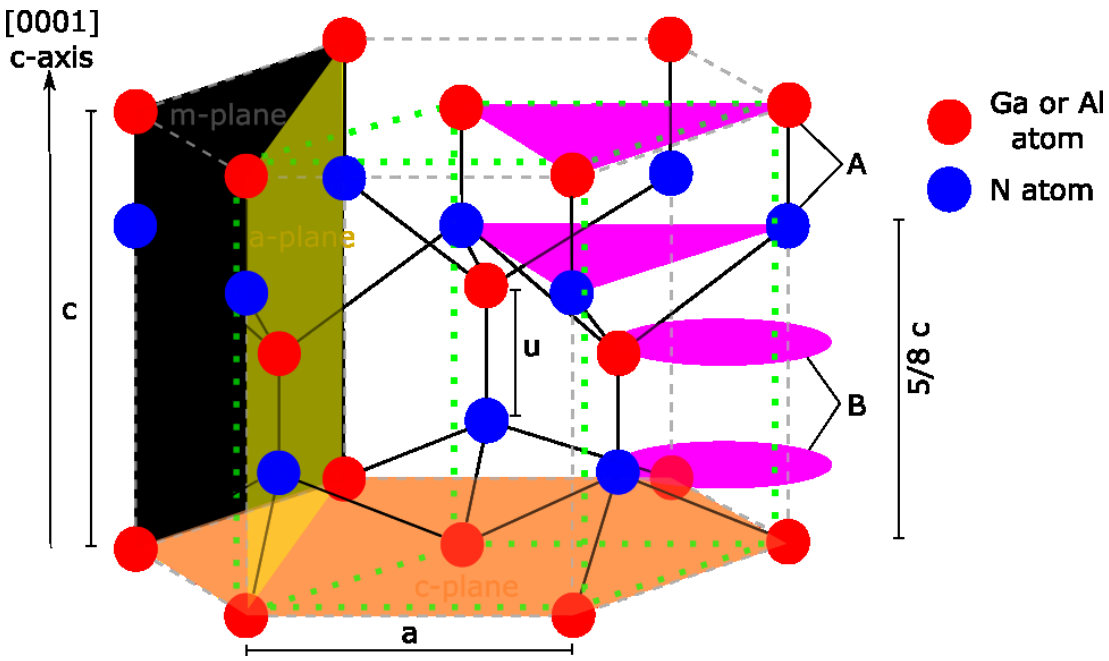

Figure 2.1: Schematic illustration of a Ga-polar wurtzite crystal structure including Ga or Al atoms (positively charged, red), N atoms (negatively charged, blue), lattice constants a and c, the material specific internal lattice parameter u, the unit cell (green), a-plane, m-plane, c-plane, ABAB stacking and tetrahedron.

Table 2.1: Lattice parameters a and c and internal lattice parameter u of AlN and GaN [51].

Wurtzite, 300 K	AlN	GaN
a [Å]	3.112	3.189
c [Å]	4.982	5.185
c/a (exp.)	1.6010	1.6259
c/a (cal.)	1.6190	1.6336
u	0.380	0.367

2.2 Piezoelectric- and pyroelectric polarization

Group-III-nitrides exhibit strongly polar wurtzite crystals. Two different effects cause this crystal polarization: pyroelectric, also known as spontaneous and piezoelectric polarization (Figure 2.2). For visualization, Figure 2.2 shows the wurtzite double tetrahedron with metal (red) and nitrogen (blue) ions for an ideal wurtzite crystal (Figure 2.2 a), an in the growth plane (x-y-plane) by externally applied stress compressively strained wurtzite crystal (Figure 2.2 b, piezoelectric polarization) and an intrinsically polarized wurtzite crystal (Figure 2.2 c, pyroelectric polarization). The pyroelectric polarization exists without applying any external stress. In an ideal

wurtzite crystal, [Figure 2.2 a)] the tetrahedron has exactly the same bond length as well as bond angle between the nearest neighbor atoms [7]. This ideal wurtzite crystal is defined over the ratio of the lattice constants c/a = $(8/3)^{1/2}$ = 1.633 [7], [8], [12] and an ideal internal parameter u = 3/8 [52]. In Figure 2.3 the nearest (blue) and second nearest neighbors (red) to a metal atom (yellow) in a wurtzite crystal are highlighted. However, even in a perfect wurtzite crystal structure, the distance in c-direction from one atom to its second nearest neighbor is 13% shorter than to the center of charges of its other second nearest neighbors [8]. For the equilibrium of the crystal lattice, the internal lattice parameter u gets larger (Figure 2.2 c and Table 2.1). This leads to a residual dipole moment, the pyroelectric polarization.

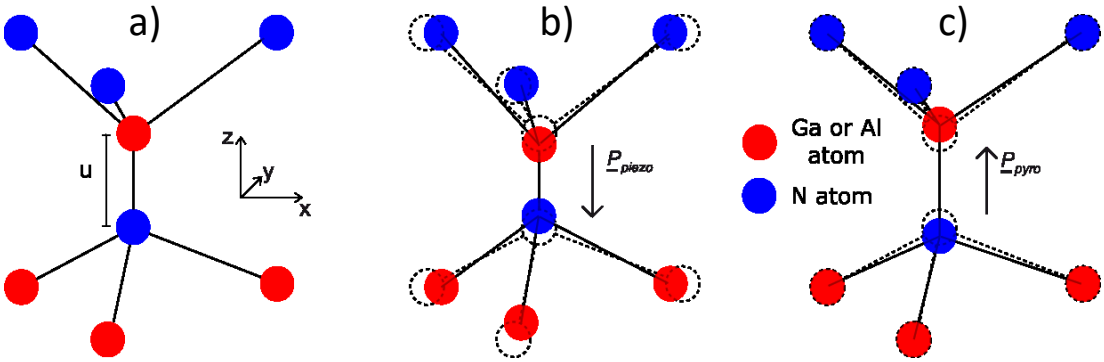

Figure 2.2: Double tetrahedrons of the wurtzite crystal structure including Ga or Al ions (positively charged, red), N ions (negatively charged, blue) and the material specific internal lattice parameter u. Coordinates for orientation: z-axis corresponds to the growth direction [0001] (c-axis). Left: ideal double tetrahedron, middel: compressively (x-y-plane) strained double tetrahedron (piezoelectric polarization), right: intrinsic deviation from the ideal double tetrahedron (constitutes the spontaneous polarization).

In the case of GaN it is c/a= 1.627 and u=0.377, whereas AlN shows an even higher deviation from the ideal wurtzite crystal structure with c/a= 1.601 and u=0.382 caused by the different electronegativities of the cations [7]. Hence, GaN and AlN have different pyroelectric polarizations ($P_{sp}^{AlN} = -0{,}09\ \frac{C}{m^2}$ and $P_{sp}^{GaN} = -0{,}034\ \frac{C}{m^2}$), which induce a built-in field in the GaN/AlN heterostructure.

Additionally, if GaN is embedded in AlN, like in this thesis, it is necessary to consider the externally applied stress due to the lattice mismatch of about 2.5 % (AlN: a = 311.2 pm, c = 498.2 pm; GaN: a = 318.9 pm, c = 518.5 pm at 300 K [46]). This lattice mismatch leads to a biaxial, compressive strain in the growth plane (x-y-plane) [53] and a relaxation (extension) in the growth direction (c-axis, z-axis) causing an extended internal lattice parameter u of the tetrahedrons in the wurtzite crystal.

Consequently, the centers of charges of metal and nitrogen ions shifts (Figure 2.2 b) (piezoelectricity) and cause additional space charges at the heterointerfaces leading to an increased built-in piezo polarization field affecting such GaN/AlN heterostructures.

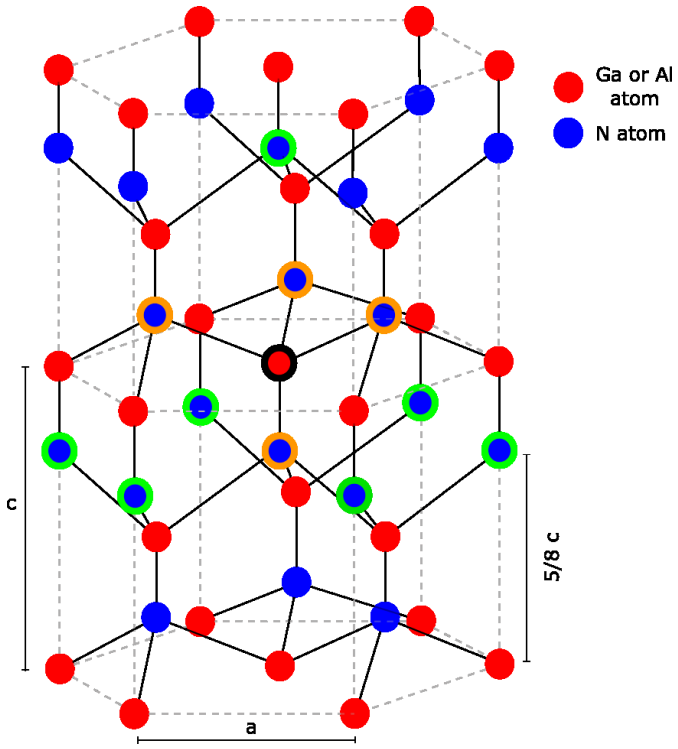

Figure 2.3: Illustration of a wurtzite crystal structure with Ga or Al ions (positively charged, red), N ions (negatively charged, blue), lattice constants a and c, central metal atom (black framed), nearest neighbors nitrogen atoms (orange framed) and second nearest neighbors (green framed).

2.2.1 Quantum-confined Stark effect

The pyroelectric and piezoelectric polarization generate considerable electric space charges at any c-plane interface between the matrix material, e.g., AlN and the nanostructure, e.g., a GaN quantum well. This causes an electric field across the nanostructure in the growth direction (c-axis) of several MV/cm that has an immense influence on the charge carriers in the nanostructure. As exhibited in Figure 2.4 b), the inherent electric field represents an incline of the valence and conduction band edges compared to the case without any interface charges. This field induced band bending implicates a smaller band gap between the conduction and valance band

plus a spatial separation of an electron and a hole confined inside the nanostructure. Hence, the energetic spacing between electron and hole decreases and shows a red-shift in photoluminescence spectra relative to the primary band gap of the actual material (here GaN). An upper limit for the red-shift Δ*E*X is given in Ref. [53] for a 2-nm-thick GaN/AlN QW by the potential drop inside the nanostructure to be Δ*E*X < 2.1 eV [53]. Furthermore, the spatial separation provokes a decreasing electron-hole wave function overlap resulting in a smaller oscillator strength of excitonic complexes and thus in a higher exciton lifetime. Of course, the charge carrier overlap additionally depends on the size of the nanostructure [54]. In comparison, as shown in Figure 2.4 a), without any interface charges the nanostructure would not suffer from a band bending and therefore, it would not suffer from the spatial separation of electron and hole—meaning the absence of red-shifted PL spectra and increased exciton life times. Both effects together, the red-shift and the spatial charge carrier separation (by confining electrons and holes to different sides of the nanostructure) are called quantum-confined Stark effect (QCSE).

It should be noted that, if we produce a large number of screening charge carriers in the nanostructure through high excitation power, the QCSE can be (partly) compensated [Figure 2.4 c)], visible as a power dependent blue-shift of the emission energy in the PL spectra. Therefore, it is important to classify whether the screened or unscreened luminescence of a nanostructure is investigated in an experiment.

As described and shown (Figure 2.4) in this chapter, the QCSE plays a key role when concerning the use of group III-nitrides for opto-electronic devices , as usually a high photon output is needed. For this reason it is indispensable to study possibilities to eliminate the QCSE, or even better, to find a way to tune it in a favored way. Exactly this is possible with the concept of the IFGARD, explained in chapter 4-5 and shown in chapter 6.

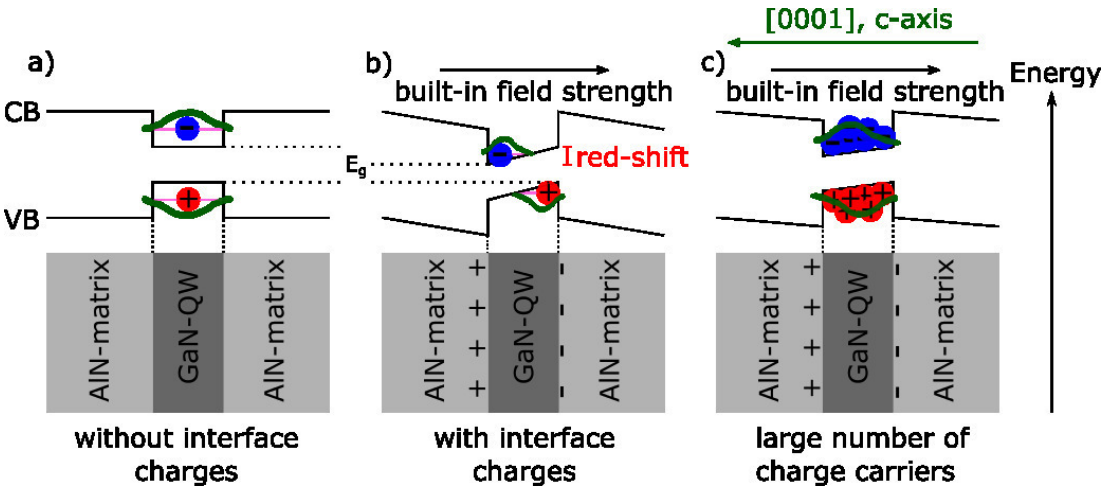

Figure 2.4: Schematic illustration of a GaN QW in an AlN matrix without surface charges a), with surface charges b) illustrating the QCSE and the screening of the QCSE through a large number of charge carriers c).

2.2.1.1 Electric dipole moment

Due to the QCSE (explained in the previous chapter 2.2.1) the electron-hole pairs in the QW suffer from a spatial charge separation in the c growth direction [see Figure 2.4 b)]. Hence, the centers of charge are not in coincidence and cause an electric dipole moment. Consequently, this built-in electric dipole moment is a measure of the separation of the electrons and holes in the nanostructure.

In general the electric dipole moment $\vec{p}$ is defined by the distance $\vec{r}$ between a positive and a negative charge q and -q

$$\vec{p} = q\vec{r} \,. \tag{2.1}$$

For a continuous charge density $\rho(\vec{r})$ distributed in a volume V it is

$$\vec{p} = \int_V d^3 \cdot \rho(\vec{r}) \cdot \vec{r} \,. \tag{2.2}$$

2.2.2 Theoretical background

The task of this chapter is to give an overview of the theoretical background of strain and polarization calculations in wurtzite crystal structures, which are the basis of calculating the built-in electric fields in wurtzite group III-nitrides and subsequently the electric dipole moments of the confined excitonic complexes.

2.2.2.1 Strain field calculation

To describe the electronic properties of a nanostructure it is inevitable to calculate the strain field inside a nanostructure and in its vicinity. The strain manipulates the electronic structure indirectly by strain-induced piezoelectric polarization and directly by shifting the band edges.

One way to calculate the strain of a nanostructure is by using a continuum mechanical model [55]. In such a model, the strain is considered for a continuum mass and not for each atom separately. For the wurtzite crystal, the stiffness tensor in the continuum is described only by five independent stiffness modules C_{11}, C_{33}, C_{44}, C_{12}, C_{13}.

Hook's law defines how stress $\hat{\varepsilon}$ creates strain $\hat{\sigma}$ according to the material stiffness $\hat{C}$:

$$\begin{pmatrix}\sigma_{11}\\ \sigma_{22}\\ \sigma_{33}\\ \sigma_{23}\\ \sigma_{13}\\ \sigma_{12}\end{pmatrix} = \hat{C}\begin{pmatrix}\varepsilon_{xx}\\ \varepsilon_{yy}\\ \varepsilon_{zz}\\ 2\varepsilon_{yz}\\ 2\varepsilon_{xz}\\ 2\varepsilon_{xy}\end{pmatrix}, \tag{2.5}$$

with σ_{ij} and ε_{ij} (I = 1, 2, 3; j = 1, 2, 3) being the components of the stress $\hat{\varepsilon}$ and strain $\hat{\sigma}$ tensor, respectively.

If the fundamental equation

$$\frac{\partial\sigma_{i1}}{\partial x}+\frac{\partial\sigma_{i2}}{\partial y}+\frac{\partial\sigma_{i3}}{\partial z}=0\,,(i=1,2,3) \tag{2.6}$$

is solved, the components of the tensor of strain can be computed. x, y, and z are Cartesian coordinates.

For wurtzite crystals with the z-axis along the [0001] direction, the stiffness tensor is:

$$\hat{C}=\begin{pmatrix}C_{11} & C_{12} & C_{13} & 0 & 0 & 0\\ C_{12} & C_{11} & C_{13} & 0 & 0 & 0\\ C_{13} & C_{13} & C_{33} & 0 & 0 & 0\\ 0 & 0 & 0 & C_{44} & 0 & 0\\ 0 & 0 & 0 & 0 & C_{44} & 0\\ 0 & 0 & 0 & 0 & 0 & \frac{C_{11}-C_{12}}{2}\end{pmatrix}. \tag{2.7}$$

In Table 2.2, the elastic stiffness coefficients for wurtzite AlN and GaN are shown.

Table 2.2: Elastic stiffness coefficients in GPa for wurtzite AlN and GaN [40], [56].

	C_{11}	C_{33}	C_{44}	C_{12}	C_{13}
AlN	396	373	116	137	108
GaN	390	398	105	145	106

2.2.2.2 Polarization calculation

In order to describe the electronic states and energies of a nanostructured semiconductor material with the k·p method, which was used to compute the numeric results presented in chapters 4, it is necessary to solve the Schrödinger equation [57]

$$\hat{H}\phi = \left(\frac{\hat{p}^2}{2m_0} + \frac{\hbar}{m_0}\vec{k}\hat{p} + \frac{\hbar^2 k^2}{2m_0} + V\right)\phi = E\phi\,. \tag{2.8}$$

With the Hamiltonian operator $\hat{H}$, the electron wavefunction ϕ and the total energy E, while the Hamilton operator is given by the momentum operator $\hat{p}$, the free electron mass m_0, the reduced Planck constant $\hbar = h/2\pi$, the wave vector $\vec{k}$ and the potential V.

V describes the potential landscape seen by the charge carriers. Therefore, it includes the polarization fields created by the wurtzite crystal structure, as explained in chapter 2.2. Here, the total polarization $\vec{P}_{total}$ of a wurtzite crystal is given by the sum of the piezoelectric polarization $\vec{P}_{piezo}$ and the pyroelectric polarization $\vec{P}_{pyro}$

$$\vec{P}_{total} = \vec{P}_{piezo} + \vec{P}_{pyro}\,. \tag{2.10}$$

As explained in chapter 2.2 , the pyroelectric polarization is parallel to the c-axis (z-direction, see Figure 2.2) of a wurtzite crystal:

$$\vec{P}_{pyro} = \begin{pmatrix} 0 \\ 0 \\ P_{pyro} \end{pmatrix}. \tag{2.11}$$

The piezoelectric polarization $\vec{P}_{\text{piezo}}$ and the stress tensor $\hat{\varepsilon}$ are linked by the electro-mechanical tensor $\hat{e}$

$$\vec{P}_{piezo} = \begin{pmatrix} P_{piezo,x} \\ P_{piezo,y} \\ P_{piezo,z} \end{pmatrix} = \hat{e}\begin{pmatrix} \varepsilon_{xx} \\ \varepsilon_{yy} \\ \varepsilon_{zz} \\ 2\varepsilon_{yz} \\ 2\varepsilon_{xz} \\ 2\varepsilon_{xy} \end{pmatrix}. \tag{2.12}$$

The electro-mechanical tensor $\hat{e}$ for wurtzite crystals with z-axis growth direction along [0001] has only three independent entries

$$\hat{e} = \begin{pmatrix} 0 & 0 & 0 & 0 & e_{15} & 0 \\ 0 & 0 & 0 & e_{15} & 0 & 0 \\ e_{31} & e_{31} & e_{33} & 0 & 0 & 0 \end{pmatrix}. \tag{2.13}$$

Table 2.3 lists the components for AlN and GaN, respectively. Here, e_{33} and e_{31} have contrarious algebraic signs. Therefore, besides the phenomenological explanation of the piezoelectric polarization in chapter 2.2, a biaxial compression in the x-y plane leads to a positive electric polarization along the z-axis, since inserting the electro-mechanical tensor $\hat{e}$ (5.13) provides

$$\vec{P}_{piezo} = \begin{pmatrix} P_{piezo,x} \\ P_{piezo,y} \\ P_{piezo,z} \end{pmatrix} = \begin{pmatrix} e_{15}\varepsilon_{zx} \\ e_{15}\varepsilon_{yz} \\ e_{31}(\varepsilon_{xx} + \varepsilon_{yy}) + e_{33}\varepsilon_{zz} \end{pmatrix}. \tag{2.14}$$

Table 2.3: Pyroelectric polarization in C/m² and piezoelectric modules $e_{33, 31, 15}$ in C/m² for wurtzite AlN and GaN [40].

	P_{pyro}	e_{33}	e_{31}	e_{15}
AlN	-0.090	1.56	-0.536	-0.418
GaN	-0.034	0.895	-0.527	-0.326

The existence of a polarization gradient, e.g., at heterointerfaces causes a space charge density defined by

$$\rho = -\nabla \vec{P}_{total} \,. \tag{2.15}$$

From this equation it is obvious that at a wurtzite material interface between AlN and GaN, the differences in pyroelectric and piezoelectric polarization (see Table 2.2 and Table 2.3) induce charge densities [58], given by:

$$\rho_{total} = \rho_{piezo} + \rho_{pyro} \,. \tag{2.16}$$

If the total surface charge ρ_{total} is known, solving the Poisson equation

$$\varepsilon_0 \vec{\nabla}\left[\varepsilon_r(\vec{r})\vec{\nabla}V(\vec{r})\right] = \rho(\vec{r})$$

provides the possibility to determine the potential V, as the Poisson equation is numerically solvable, with the vacuum permittivity ε_0 and the relative permittivity ε_r of the materials. The potential V is added to the Hamilton operator in the Schrödinger equation (2.8) representing the band-edge bending of the potential landscape by the polarization of the wurtzite crystal structure.

2.3 Band structure

The III-V compound semiconductors GaN and AlN have direct band gaps, as their valance band edge maxima and conduction band minima with band gap energies of 3.51 eV and 6.23 eV [46] are at the Γ point. Figure 2.5 shows the band structures of a) GaN and b) AlN with the corresponding energy values listed in Table 2.4. The energetically highest valance bands in GaN and AlN are formed by the binding 2p states of the nitrogen ions whereas the conduction bands originate from the antibinding 4s states of gallium or the antibinding 3s states of aluminum. The three upper most valence bands are called A, B and C band. The upper valance band splitting originates from the crystal field leading to a splitting of heavy (HH) and light hole (LH) bands. The third splitting is caused by the spin-orbit interaction (SO). The essential difference between GaN and AlN is the symmetry ordering of the three valance bands while the conduction bands both have a Γ_7 symmetry. For GaN, the three upper most valance bands have a symmetry ordering of Γ_9, Γ_7, Γ_7 in contrast to AlN that exhibits a Γ_7, Γ_9, Γ_7 symmetry ordering (see Figure 2.5). Tension and compression influence the distances between those three valance bands as well as the band gap to the conduction band.

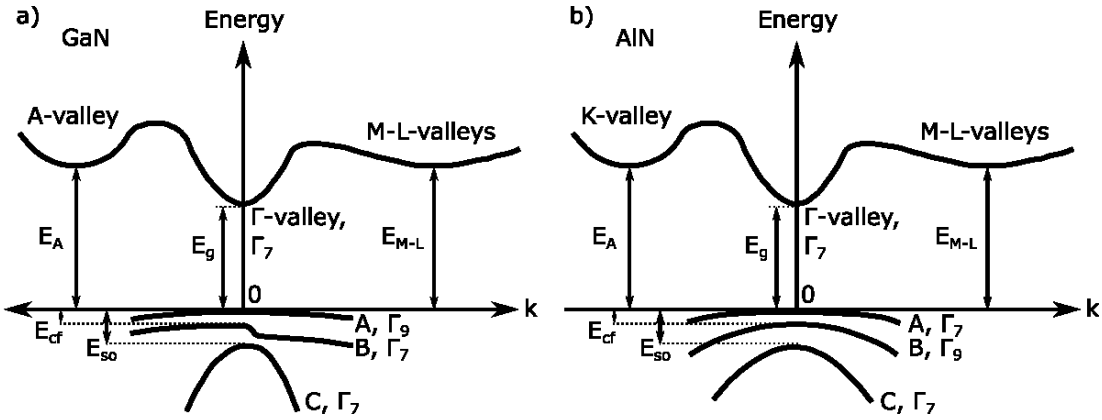

Figure 2.5: Band structure for a) GaN and b) AlN depicted with the energy gaps for the A-valley E_A, the Γ-valley E_g, the M-L valley E_{M-L} and the energy splitting in the valance bands A, B and C. The energy values are given in Table 2.4 [60]–[62].

Table 2.4: Band structure relevant energies in eV for the A-valley E_A, the Γ-valley E_g, the M-L valley E_{M-L} and the energy splitting in the valance band resulting from the crystal field E_{cf} and spin-orbit interaction E_{so} for GaN and AlN [40], [53], [61] [40], [62].

in eV	E_A	E_g	E_{M-L}	E_{cf}	E_{so}
AlN	7.2	6.25	6.9	-0.169	0.019
GaN	4.7-5.5	3.51	4.5-5.3	0.010	0.017

3 Experimental methods

The purpose of this chapter is to present the applied experimental techniques. To demonstrate the fundamental validity of the IFGARD, basic photoluminescence techniques had been used. The fundamental optical properties of the IFGARD NWs had been investigated by means of micro-photoluminescence (µ-PL) and time resolved photoluminescence (TRPL) measurements. For the TRPL measurements, two different setups enabled the detection of exciton decay times from the ps up to the µs range. In the following sections, the techniques are explained in more detail. For all experiments, the samples were mounted into a micro He-flow cryostat providing measurement temperatures from 4 K up to 400 K.

3.1 Micro-photoluminescence

The micro-Photoluminescence (µ-PL) measurements had been carried out to investigate the optical properties of the IFGARD NWs. In the µ-PL setup, the NWs had been excited by a frequency quadrupled emission line of a 76 MHz pulsed 1032 nm faser laser with a pulse width of 5 ps resulting in an excitation wavelength of 258 nm. In doing so, the excitation power was varied between 0.035 µW and 500 µW with continuous filter wheels. The spectra were dispersed within a 0.85 m single monochromator by a 150 l/mm (500 nm blazed) grating. The photons were detected with an UV-enhanced Si-charge-coupled device (CCD) array. All spectra were calibrated with an Hg-lamp and vacuum corrected.

A schematic illustration of the µ-PL setup is shown in Figure 3.1. The faser laser has two exits, one for the frequency doubled 516 nm wavelength emission and one for the original 1032 nm wavelength emission. The 1032 nm laser beam is required for the time resolved photoluminescence measurements (explained in chapter 3.2.1) as it serves in that context as the start signal for the time correlated single-photon counting technique (TCSPC).

For the excitation of the specimen the 1032 nm pulsed laser excitation first got frequency doubled by a second harmonic generator (SHG) within the faser laser. Second, the 516 nm frequency doubled emission got once more frequency doubled by an external SHG in the set-up. The so generated 258 nm laser beam is sent through

motorized continuous filter wheels for power dependent µ-PL measurements. After that, the laser light is guided through a beam splitter and focused via a microscopic lens (microspot lens by Thorlabs, 20x magnification, numerical aperture 0.4, laser focus spot ≈ 2 µm) on the sample, which is mounted in a helium-flow microscopy cryostat (ST-500, by Janis) providing measurement temperatures from approximately 4 K up to 400 K. The cryostat is positioned on a 2-axis motorized stage and the lens is mounted on a 3-axis piezo stage allowing a scanning of the specimen's surface. Hence, precise mapping of the specimen is possible over a large sample area collecting spectra depending on the position on the sample. However, mapscans of the samples have not been used as a characterization method in this work, as they were only used to position the laser spot on the sample. For this positioning, a customized Köhler illumination combined with a CMOS camera module enables direct imaging of the samples surface. The beam splitters for the Köhler illumination and the CMOS camera are removed during the photoluminescence measurements. Emitted photons from the sample are collected in a back scattering geometry by the same microscopic Thorlabs lens as used for the excitation. The emitted light is guided via the remaining beam splitter to a focus lens in front of the monochromator. The photons are detected with a nitrogen cooled UV-enhanced Si-charge-coupled device (CCD) array.

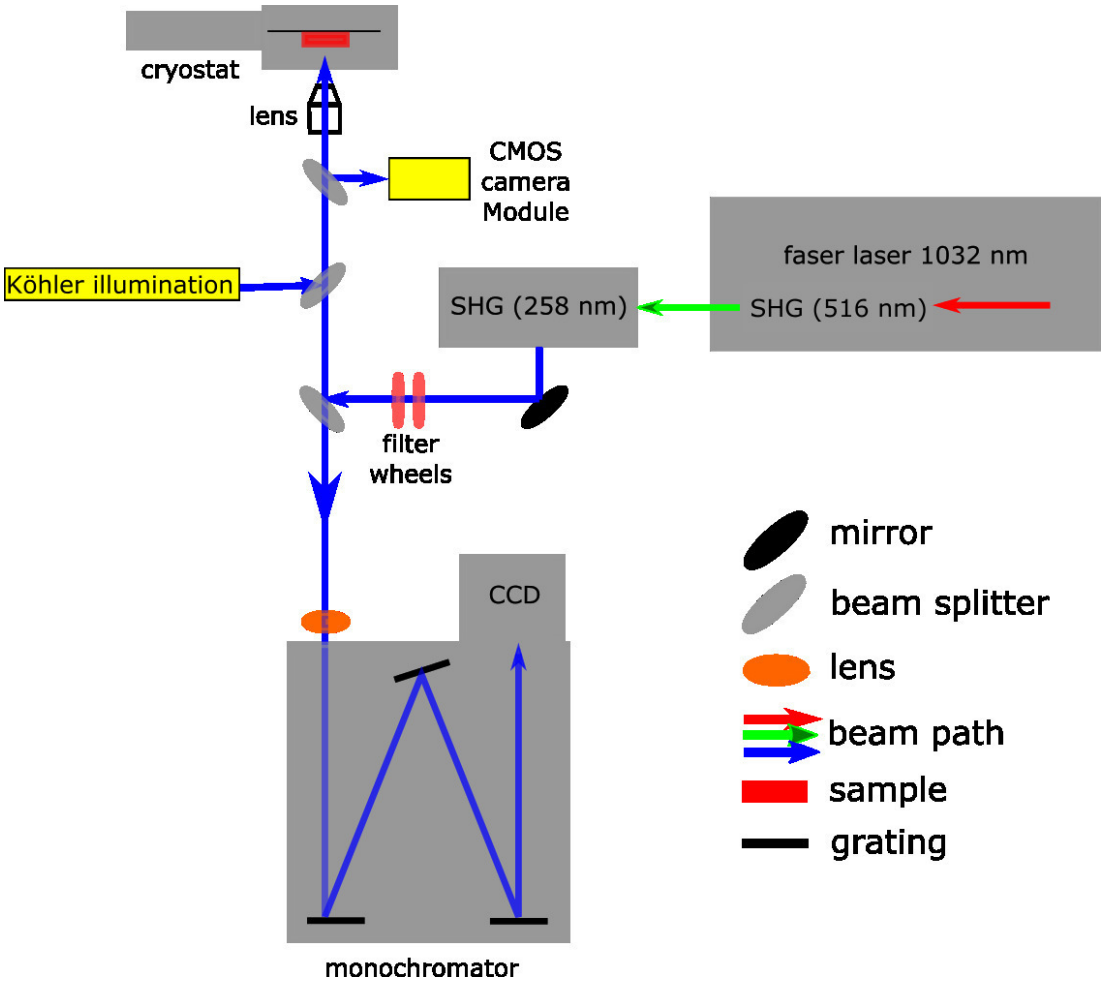

Figure 3.1: Schematic sketch of the µ-PL set-up.

3.2 Time-resolved photoluminescence

Time-resolved Photoluminescence (TRPL) measurements were performed to study the decay dynamics of the excitons in the NDs. As the decay time varies drastically for the different samples it was necessary to use two different set-ups: one for the ns and another for the µs range. The PL transients were corrected with the specific response characteristic of the respective set-up.

3.2.1 ns-range setup

In the ns-range TRPL setup, the samples were mounted in the same setup as described in chapter 3.1. By flipping one mirror, it is possible to change the µ-PL setup (Figure 3.1) into the TRPL set-up (Figure 3.2). The TRPL setup is than coupled with a subtractive double monochromator (McPherson 2035) (each 0,35m long) containing a 300 nm blazed 2400 l/mm grating as a dispersing element. A time-correlated single

photon counting (TCSPC) technique (coupled with a TCSPC measurement card and a fast TCSPC photodiode module) is used in combination with a PMA hybrid photomultiplier detector records the PL transients with approximately 30 ps time resolution. Besides, the original laser pulse with a wavelength of 1032 nm is used as the start signal detected by a TCSPC diode for realization of the time resolved measurements.

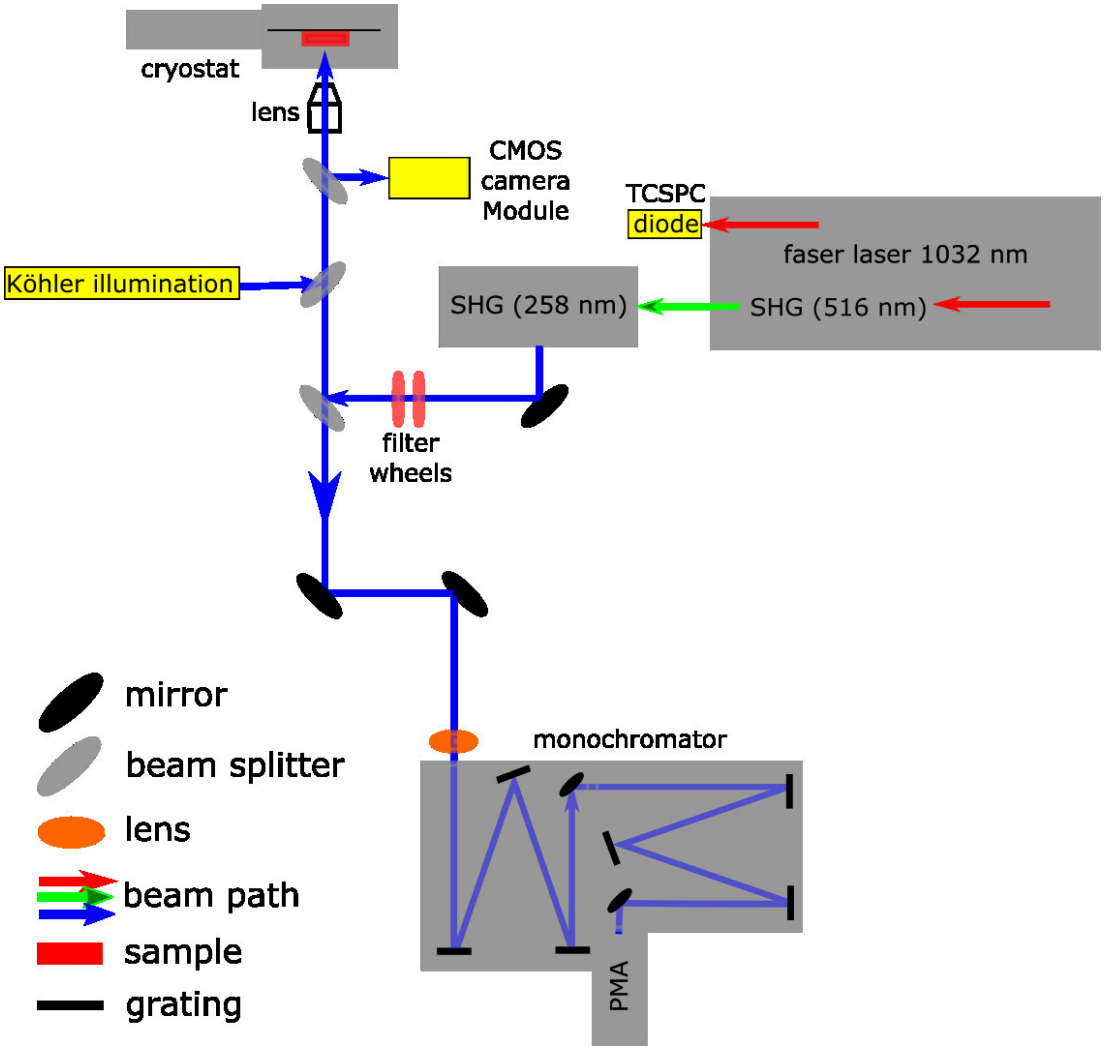

Figure 3.2: Schematic sketch of the ns-range TRPL set-up.

3.2.2 µs-range setup

A scheme of the µs-range TRPL set-up is illustrated in Figure 3.3. The measurements were performed with a 350 nm, pulsed dye laser (100 Hz, 20 ns pulse width) whereas the dye laser is pumped by a 308 nm (100 Hz) XeCL-Excimer laser. The emitted laser beam is guided through manual filter wheels, for varying the excitation power, a

beam splitter, and mirrors to the specimen in a helium-flow microscopy cryostat (by Oxford). With an UV-enhanced lens in front of the cryostat, the laser beam is focused on the sample and the emitted photons from the sample are collected (back scattering geometry) towards an additive double monochromator. A small mirror (diameter of 5 mm) reflects the laser light on the sample and blocks its direct reflection towards the monochromator, which also blocks a particular percentage of photons generated in the sample. Two monochromators with focal lengths of 1 m and a holographic 1800 l/mm grating each are combined to one additive double monochromator dispersing the light coming from the sample. For recording the PL transients a multichannel plate detector combined with a photon counting technique was used. To generate a start signal, the laser beam is guided through a beam splitter to a TCSPC diode directly after the dye laser.

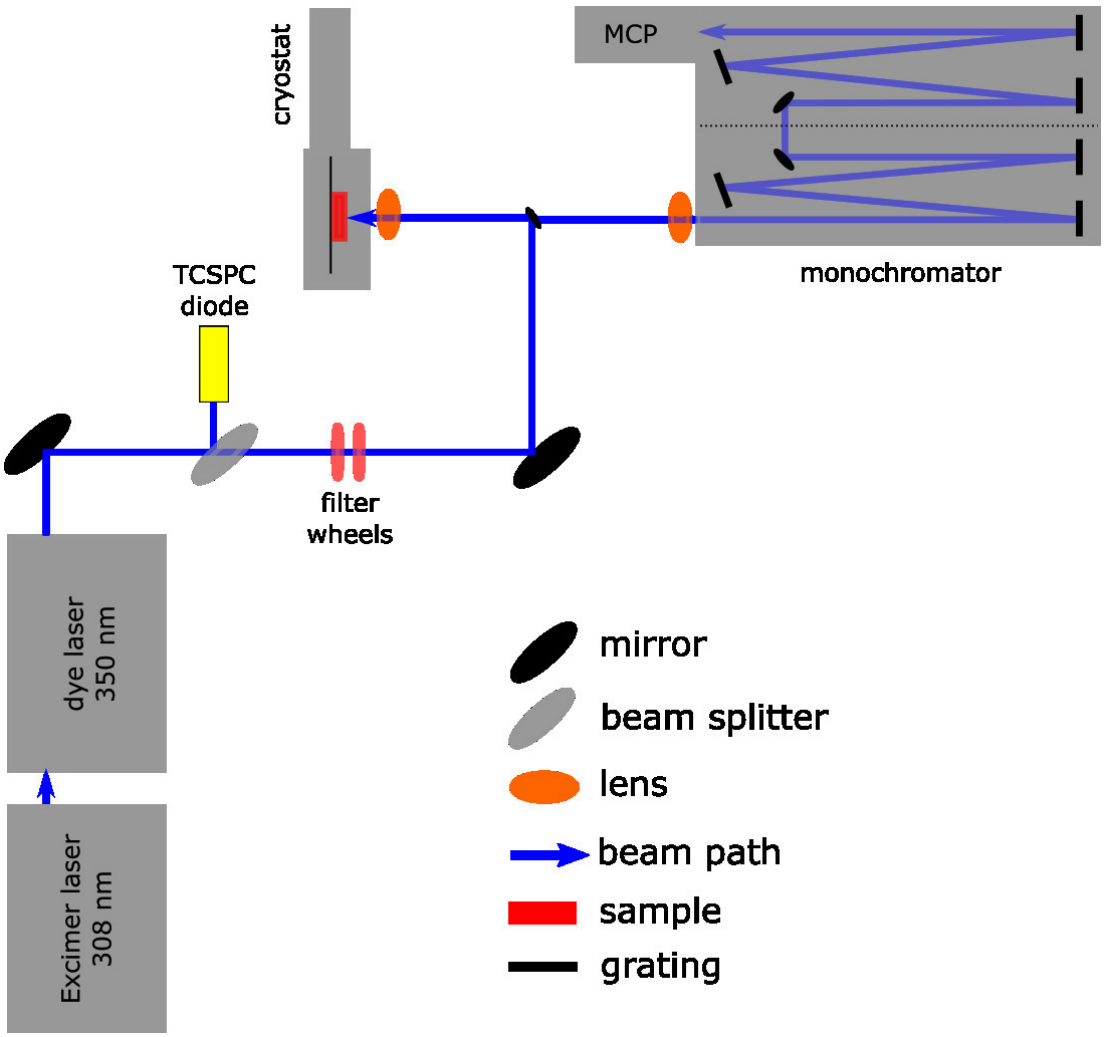

Figure 3.3: Schematic sketch of the µs-range TRPL set-up.

4 IFGARD

Different approaches for reducing the built-in electric field in wurtzite crystals have been tested in the last decades [28]–[31], [63]. All of those already tested approaches suffer from different disadvantages concerning the crystal quality, inappropriate requirements on the growth procedure, or being cumbersome in the realization and those circumstances make these approaches unconvertible for a commercial use [33]–[37], [64]. In this thesis, a new method is presented, that solves these issues. A special design, the Internal field guarded active region design (IFGARD) for polar crystal materials, like wurtzite makes it possible to form any particular built-in potential landscape or to eliminate the built-in electric field in nanostructures without having any special requirements on the production, hence, it is suitable for the industrial use [38]–[40]. This design leads to an enhanced overlap of the electron and hole wave functions, which causes a boost in the exciton annihilation rates and a reduction in the electric dipole moment of excitonic complexes confined in IFGARD nanostructures. Besides, the reduction of the electric dipole moment implicates a decrease in the electrostatic coupling of close-by defects with fluctuating charge. Additionally, the reduction of the spatial separation of electrons and holes reduces the coupling to phonons, which is important for the room temperature operation of sensitive devices like, e.g., single- and entangled-photon sources.

In the following chapter, the design is explained in detailed for a quantum dot (QD) and a quantum well (QW) based on the publication [40]. Due to the fact, that the samples, experimentally investigated in this thesis, exhibit a nanowire (NW) structure, chapter 5.2 describes the IFGARD structured NWs, experimentally investigated here.

4.1.1 Original IFGARD

The IFGARD was invented by our group members G. Hönig, G. Callsen and A. Hoffmann [38]–[40] in 2015. They considered the design for QD and QW structures based on GaN embedded in AlN. This does not mean, that this concept is only suited for this material system; in fact, it is applicable for any polar material like ,e.g., ZnO/(Zn,Mg)O, [111]-(In,Ga)As/GaAs, and GaN/(Al,Ga)N as well as nanostructures

like QDs, QWs, nanowires, etc.. This chapter explains the underlying principle of the IFGARD exemplarily for GaN/AlN QDs and QWs.

4.1.1.1 IFGARD for Quantum dots

Figure 4.1 demonstrates the IFGARD principle for a wurtzite GaN QD. The left side shows a conventional 2-nm-high GaN QD (dark gray) grown in c-direction, embedded in an AlN matrix (light gray). On the right hand side, the IFGARD is shown for the same QD. The specific design is characterized by an embedding of the conventional structure in so called GaN guard layers [40]. For this design, no particular requirement for the growth procedure is needed and it is possible to resort to well-established growth methods for GaN and AlN. This gives the advantage to have no additional costs for the implementation of the IFGARD for devices, besides the absence of a degraded crystal quality. Keeping the most-natural crystal growth is a big advantage of the IFGARD over any other alternative approaches [28]–[31] to reduce the internal polarization fields in semiconductor heterostructures. Nevertheless, IFGARD is not intuitive as the additional GaN guard layer reabsorbs a particular percentage of the photons generated in the QD. But as discussed by Hönig et al. [40] and demonstrated by the experimental results of this thesis, the overall gain based on the elimination of the polarization field in, e.g., the QD with the resulting boost of the exciton recombination probability [Figure 4.1 f)] overcompensates the reabsorption losses by the guard layers, if the thickness of the guard layer in the emission direction is below the emitted wavelength—in the investigated samples it was approximately 1/10th of the wavelength. It was numerically demonstrated that this IFGARD can lead to a homogeneous piezo- and pyroelectric polarization potential inside a quantum structure, which is illustrated in the color plot Figure 4.1 e) [compare the color plot of the conventional QD Figure 4.1 b)]. This goes along with flat conduction- and valance-band edges in the QD structure [Figure 4.1 c)]. The suppression of the electric field in the QD results in a higher spatial overlap of the electron-hole wave function, which induces a drastic rise of the exciton recombination probability [Figure 4.1 c)]. As calculated in Ref. [40], this raised exciton recombination probability implicates a gain in the emitted single photons by approximately 2 orders of magnitude due to an oscillator strength increment factor of 100. Note that the emission energy of the

IFGARD QD is 4.2 eV, which is 700 meV higher than the emission energy of the QCSE-red-shifted emission energy of the conventional QD (3.5 eV).

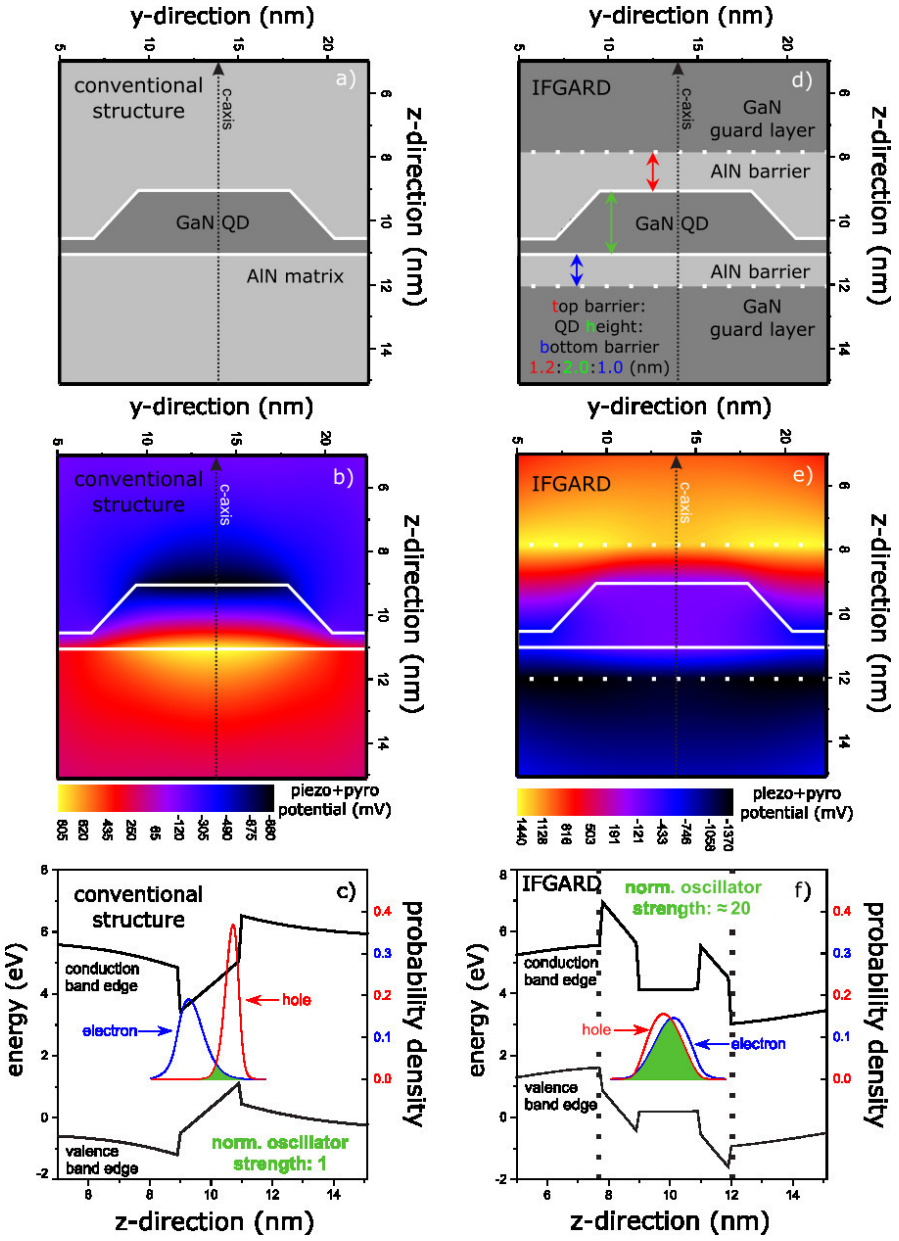

Figure 4.1: Left side: Conventional GaN/AlN QD structure grown along the most natural growth direction [0001]. 2D scan of the layer sequence a), a contour plot showing the sum of the piezo- and pyroelectric potential revealing a gradient illustrated by the color change from yellow to black inside the QD b), and a band edge scan through the QD center with the typical tilt c). The overlap of the electron (blue) and hole (red) wave functions as a measure of the transition probability in the QD is green. The potential gradient inside the QD b) is responsible for the charge carrier separation c) resulting in a reduced transition probability for conventional QDs. Right side: IFGARD GaN/AlN QD structure grown along the most natural growth direction [0001]. 2D scan of the layer sequence d), a contour plot showing the sum of the piezo- and pyroelectric potential exhibiting a constant electric potential illustrated by the homogeneous purple color inside the IFGARD QD e), and a band edge scan through the IFGARD QD center with the flat band edges f) resulting in an immense increase of the transition probability due to the increased overlap (green) of the electron (blue) and hole (red) wave-function [45].

Delineated in Figure 4.1 a) are the different dimensions of the top barrier t (red), QD height h (green), and the bottom barrier b (blue). This labeling is important for understanding Figure 4.2, which shows another parameter that is important to take into account for tuning the electric field inside an IFGARD QD: the AlN barrier thickness. Hönig et al. performed a numeric study on the dependence of the electric potential inside a 3-nm-high IFGARD QD on the AlN barrier thickness (0.5 nm up to 2.5 nm), presented in Figure 4.2. The AlN barrier thickness first was varied symmetrically (t=b) and second asymmetrically (t≠b). As apparent in Figure 4.2, the minimum absolute potential drop of -5 mV arises from an asymmetric barrier thickness of 1.5 nm above and 2 nm beneath the QD or vice versa (called “stack inversion”, green and black curves). Whether the thicker barrier or thinner barrier is beneath the QD influences the absolute potential value but not the potential drop inside the QD. The bowing in the electric potential becomes dominant when achieving flat-band conditions. Its origin is the strain field within the QD, which causes this piezoelectric potential gradient.

For the symmetric barrier thickness variation, 2 nm to 1.5 nm barrier thicknesses exhibit the smallest potential drop. In comparison to the conventional case (orange dashed line in Figure 4.2) with a potential drop of -2112 mV, the IFGARD QD with the optimal asymmetric barrier thicknesses shows an oscillator strength that is 100 times larger.

Remarkably, passing over from thicker to thinner symmetric AlN barrier thicknesses changes the electric potential gradient from negative to positive values. The achievable positive as well as negative potential drops inside the QD could be used for flat band conditions under adequate operation voltages in electrical driven devices.

Furthermore, the IFGARD narrows the ensemble luminescence peak of nanostructures by several aspects. First of all, without the QCSE, the luminescence energy of nanostructures is less affected by monolayer fluctuations of the nanostructure thickness, which is shown for the investigated NDs in chapter 6.1. Second, if, e.g., a QD is occupied by more than one exciton, multiexcitons are formed, which recombine with a different emission energy compared to single exciton recombination in a QD. This can result in an emission broadening of strongly pumped

QD ensemble peaks. Such a high carrier injection is typically used for screening of the built-in electric field, gaining higher photon emission rates, which becomes obsolete by the IFGARD. Third, the emission energy is pump power dependent, due to the screened QCSE, which is also not the case with the IFGARD. Finally, without such strong electric dipole moments of the excitonic complexes, an electrostatic coupling to charged defects in the vicinity of the nanostructures or coupling to phonons (described by the Huang-Rhys factor) becomes minimized too. In sum, the recombination rate gets drastically enhanced, ensemble luminescence energetically narrows, and the photon emission becomes less temperature sensitive. IFGARD devices are, therefore expected to become faster in their response to modulated pump sources and the quantum efficiency rises as parasitic decay channels become less efficient.

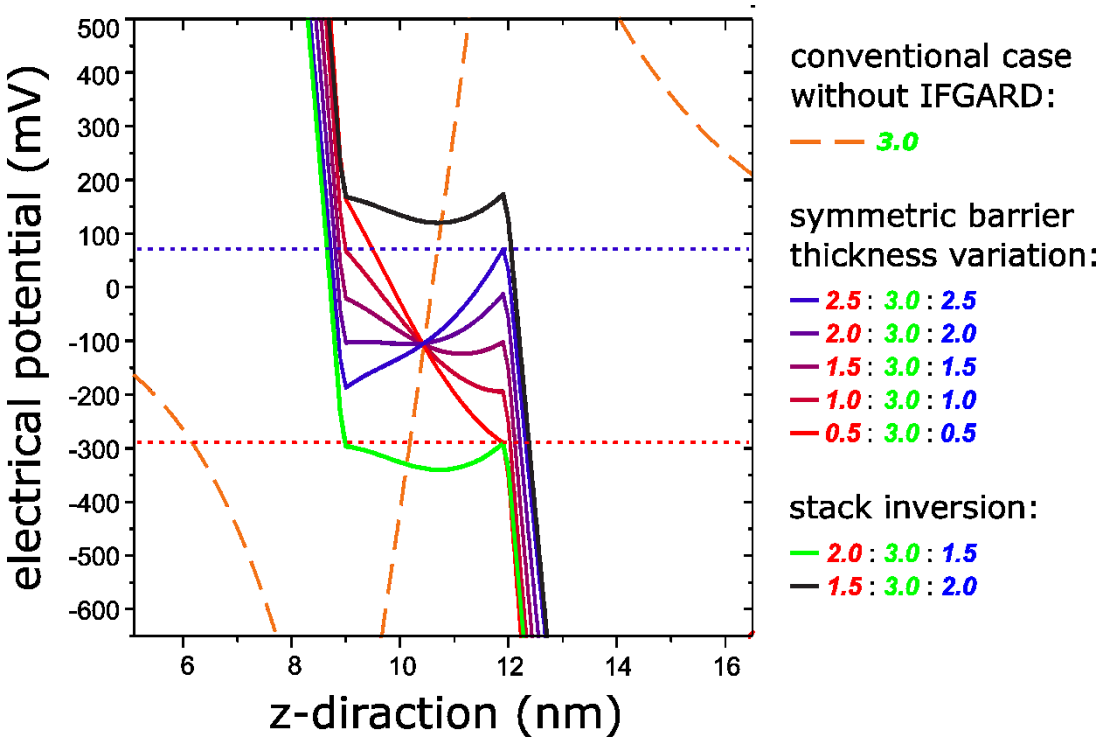

Figure 4.2: The sum of the piezo- and pyroelectric potential across an IFGARD QD for different layer dimensions in comparison to the conventional case without IFGARD (dashed line). The height of the GaN QD is kept constant at 3 nm, the AlN barrier thickness was varied symmetrically (red = blue number) and asymmetrically including a "stack inversion" *[45].*

4.1.1.2 IFGARD for Quantum wells

The IFGARD can also be applied to QWs as depicted in Figure 4.3. In Figure 4.3 a 2-nm-thick IFGARD QW structure embedded in 1-nm-thick AlN barriers, again with the preferred [0001] stack direction is sketched. The interface charges are represented by algebraic + (red) and - (black) signs. As sketched in Figure 4.3, the IFGARD QW is comparable with a stack of infinite open-circuit plate-type capacitators.

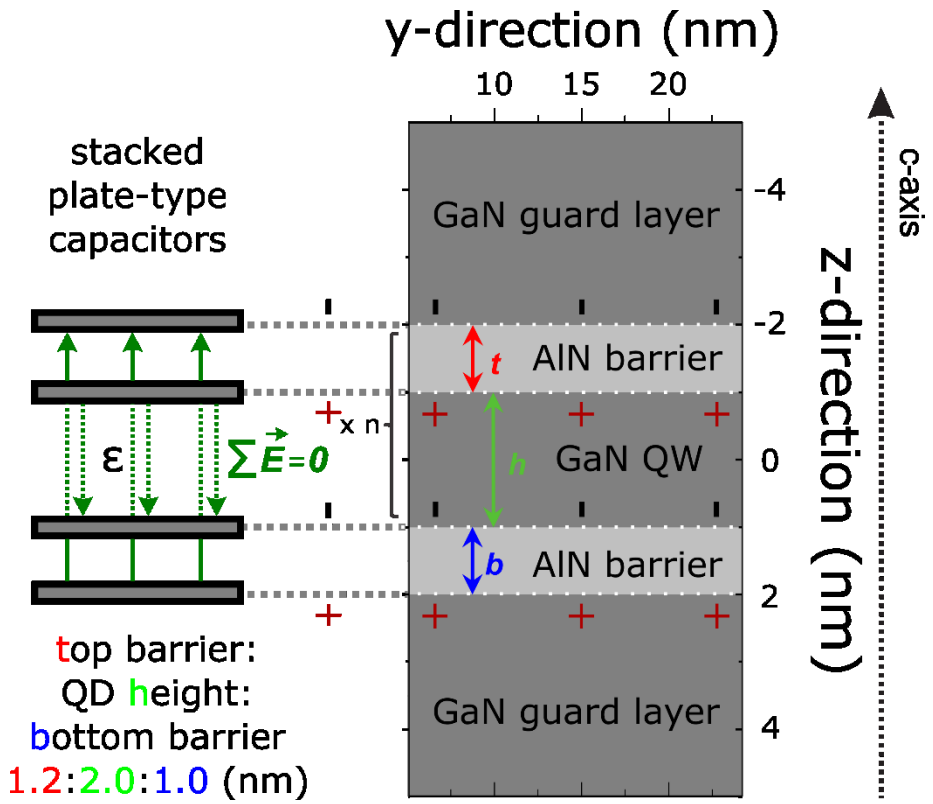

Figure 4.3: Comparison of an IFGARD QW with an electronic analogon – stacked, plate-type capacitors with distances t, h and b, and the permittivity ε. The distances between the capacitor plates are equivalent to the top barrier of 1 nm, the QW thickness of 2 nm and the bottom barrier of 1 nm. The interface charges, resulting from the polarization, are marked with positive (+, red) and negative (-, black) mathematic signs. Green arrows represent the corresponding electric fields inside the capacitor plates, showing a field annihilation within the inner plates (QW).

Each charged capacitor plate represents a space charge density at the interfaces GaN-AlN and AlN-GaN due to the spontaneous and piezoelectric crystal polarization. The capacitor plate distances match the thickness of the barriers or the QW and the green arrows depict the electric field in the inner and outer capacitors. The opposite directed electric fields in the inner capacitor annihilate each other as they do in the GaN QW. However, the electric field strength E within an laterally infinite capacitor

$$E = \frac{Q}{\varepsilon_0 \varepsilon_r A} =: \frac{\sigma_A}{\varepsilon_0 \varepsilon_r},$$

with the electrical charge Q, the vacuum permittivity ε_0, the relative permittivity ε_r, the area A of the capacitor plate, and σ_A defined as the plate/space charge density, is independent of the distance between the capacitor plates. That means, neither the GaN QW nor the AlN barrier thickness have an influence on the electric field inside an infinite QW, as the sum of the electric field strengths (green arrows in Figure 4.3) in the QW remains zero. The same is true for the electric field in the AlN barriers, the non-zero electric field does not change for varying barrier thicknesses. It is important to note, that the independence of the layer dimension is contrary to the case of QDs. In a QD it is possible to tune the electric field across the QD, as the QD profile has a

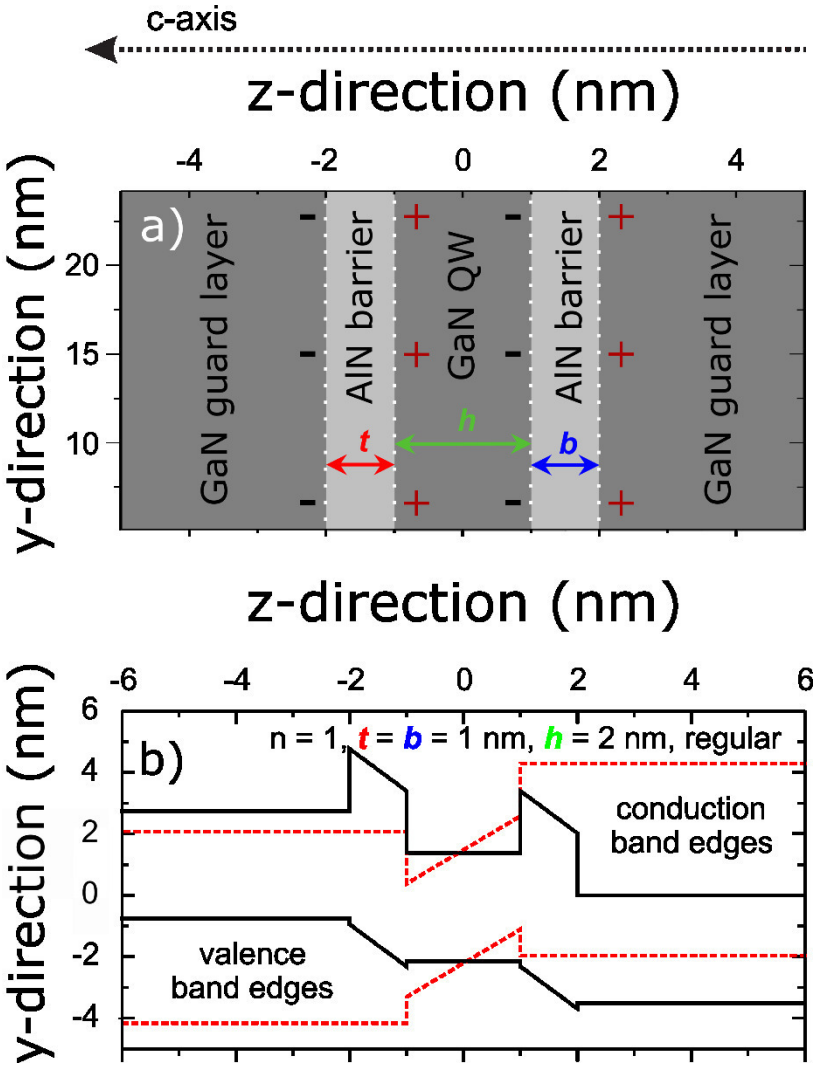

Figure 4.4: Illustration of the IFGARD stack sequence a) in comparison to the conduction- and valence band edges b). In the IFGARD sequence a), grown along the most natural c- axis, the interface charges caused by the crystal polarization are marked with positive (+, red) and negative (-, black) signs.

trapeze shape. The less-polar side facets provoke different amounts of space charges at the top and bottom of the QD interface. This tunability in “non-infinite” quantum structures becomes important in chapter 5, where the specific shape of the investigated IFGARD samples is crucial.

Figure 4.4 compares the band edge characeristics of a 2-nm-thick IFGARD QW with 1-nm-thick AlN barriers (black) to a conventional 2-nm-thick QW (red). The IFGARD QW shows a constant electric potential (zero field strength) inside the QW and a non-zero, constant electric field strength within each barrier. The electric field inside the AlN barriers is equal due to identic space charge densities at the interfaces between the QW and barrier material on either of both sides. The constant non-zero electric field in the AlN barriers leads to a net potential offset on both boundaries of the calculated area. (Von Neumann boundary conditions are used in the simulation to mimic a much larger simulation area circumventing artificially induced band edge tilts due to Dirichlet boundary conditions in such small calculation areas.) As found for the QDs in chapter 4.1.1.1, the conventional QW (red) exhibits a huge built-in electric field.

Even the use of stacked IFGARD QWs (one fundamental stack consists of one barrier with one QW) is feasible without changing the flat band edge profile in each QW. Possible IFGARD stacks are illustrated in Figure 4.5. Figure 4.5 a) shows an exemplary IFGARD stack with three 1-nm-thick QWs and a constant barrier thickness of 0.5 nm. By altering the barrier thickness [Figure 4.5 b) - d)], the height of each energy step to the next QW is affected. Furthermore, by variation of the Al(x)Ga(x-1)N compositions, the band edge bending can be tuned [Figure 4.5 d)]. This becomes relevant if a pre-tilt of the band structure is desired, that will be compensated by an applied voltage. A positive or negative pre-tilt of the band structure is possible by the choice of the Al(x)Ga(x-1)N composition.

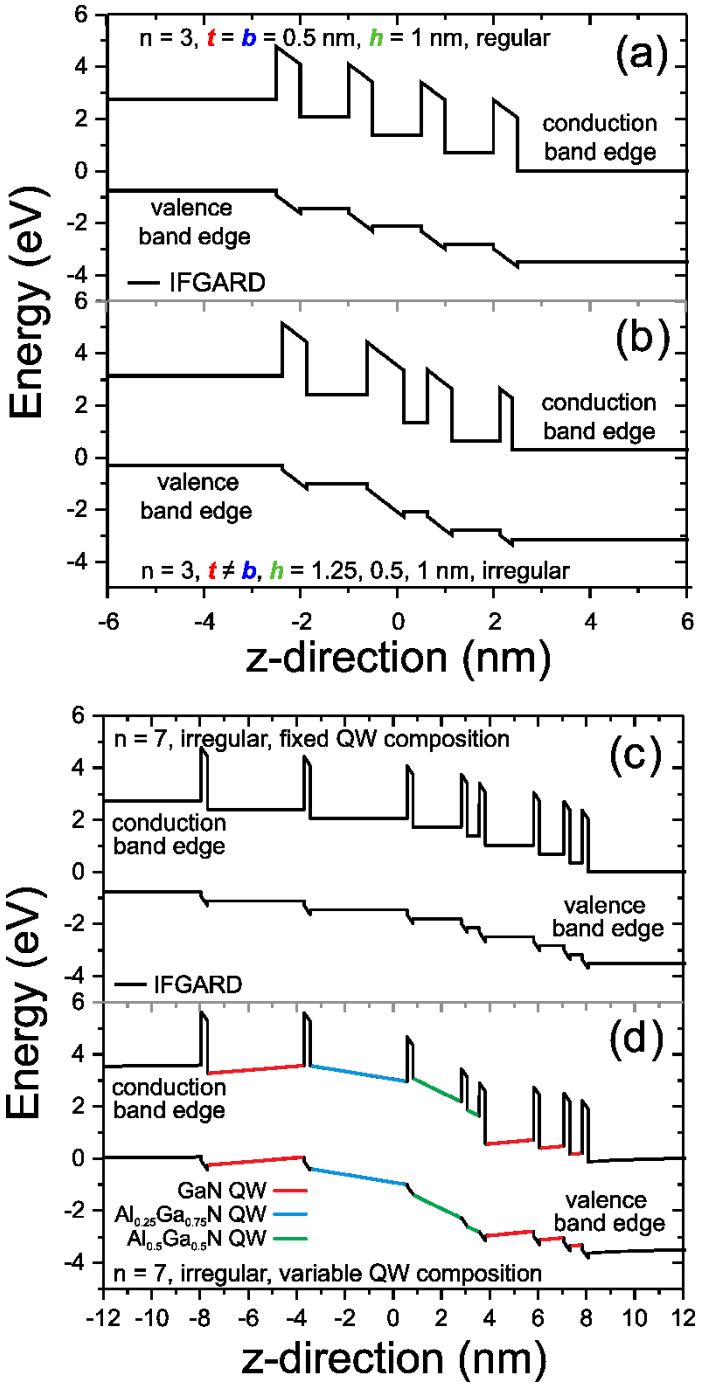

Figure 4.5: Applicability of the IFGARD for multiple QWs with fixed or variable QW composition showing the universal validity of the IFGARD and the possibility to create potential landscapes by composition variation d).

5 Samples

This chapter describes the experimentally investigated GaN/AlN nanodiscs (NDs) in GaN nanowires (NWs) samples. First, information about the growth procedures are given and the nominal layer thicknesses within the analyzed sample series are introduced. Second, the morphology of the IFGARD structured NWs is characterized by carried out scanning electron microscopy (SEM) studies. Here, the SEM images account for rough information regarding the length, diameter and crystal structure.

5.1 GaN/AlN-IFGARD nanodiscs [45]

The investigated GaN nanowires are grown by plasma assisted molecular beam epitaxy ($T_{substrate}$= 750°C, T_{Ga}= 916°C, T_{Al}= 1069°C) on Si (111) substrates [21], [31], [65]. Plasma-assisted molecular beam epitaxy (PAMBE) features a self-assembled growth of GaN NWs on Si(111) without needing a catalyst material [66]–[69]. The advantage of self-assembled NWs over growth techniques with a catalyst material as, e.g., Ni in vapor-liquid-solid (VLS) [70], is the higher structural quality [71]. By utilizing c-plane growth, the side-facets of the grown NWs are formed by non-polar crystal planes [72], [73]. Table 5.1 lists all investigated samples, with their individual sample number, incorporated AlN barrier thickness, and GaN ND thickness. Anticipating the findings in regard to the built-in field strengths in the samples, those are divided into a “barrier series”, representing the so called “QCSE regime”, and a “ND series”, representing the so called “confinement regime”. These regime names correspond to the remaining electric field or the total elimination of the electric field inside the NDs. In the latter case, without built-in fields, the electronic sample properties are purely affected by the confinement of the charge carriers. A more detailed explanation of the design and morphology is given in the following chapter 5.2.

Table 5.1: List of samples with the sample description, the sample number and the corresponding barrier (t = b) and QW thicknesses.

sample description 40xAlN/GaN	sample number	t,b, barrier thickness-AlN (nm)	h, QW-thickness-GaN (nm)
barrier series	N160302	1	4
QCSE regime	N160225	2	4
	N160215	4	4
	N160229	6	4
QW series	N16071210B1	1	1
confinement	N1607190A1	1	2
regime	N1607080A1	1	3

5.2 Morphology of the NW samples [45]

First, the morphology of the GaN NWs is investigated by SEM measurements[1]. Figure 5.1 shows: schematic sketches of the NWs including NDs with the IFGARD a) & c), the corresponding calculated band structure b), and exemplary SEM images d) to k) for all samples of the QCSE regime. The nanowires grow along the polar [000-1] axis of their wurtzite crystal structure. The center of the nanowires consists of 40x-stacks of GaN NDs exhibiting the IFGARD, with each ND being embedded in AlN barriers. The first GaN guard layer (which is equal to the GaN NW base) has a thickness of 650 nm. The nanowire ends on a 20 nm GaN Guard layer to realize the IFGARD. It is most important to understand that the fundamental stack element consists of one AlN barrier followed by one GaN ND [40] being repeated 40-times to enhance the optical signal and hence to clearly separate the ND luminescence from the luminescence of the two GaN guard layers encapsulating the ND stack on both ends.

By analyzing SEM images exemplarily shown in Figure 5.1 d) to k) for the samples within the QCSE regime, the NWs are found to exhibit diameters between 60 to100 nm and a total length of up to 1 µm (see summarizing Table 5.2). Furthermore, a continuous increase of the average NW diameter from 61 nm to 94 nm for thicker AlN barriers (see Table 5.2) is visible.

[1] The SEM investigation had been performed by Dr. Jörg Schörmann and Dr. Jörg Teubert in the Justus-Liebig Universität Giessen.

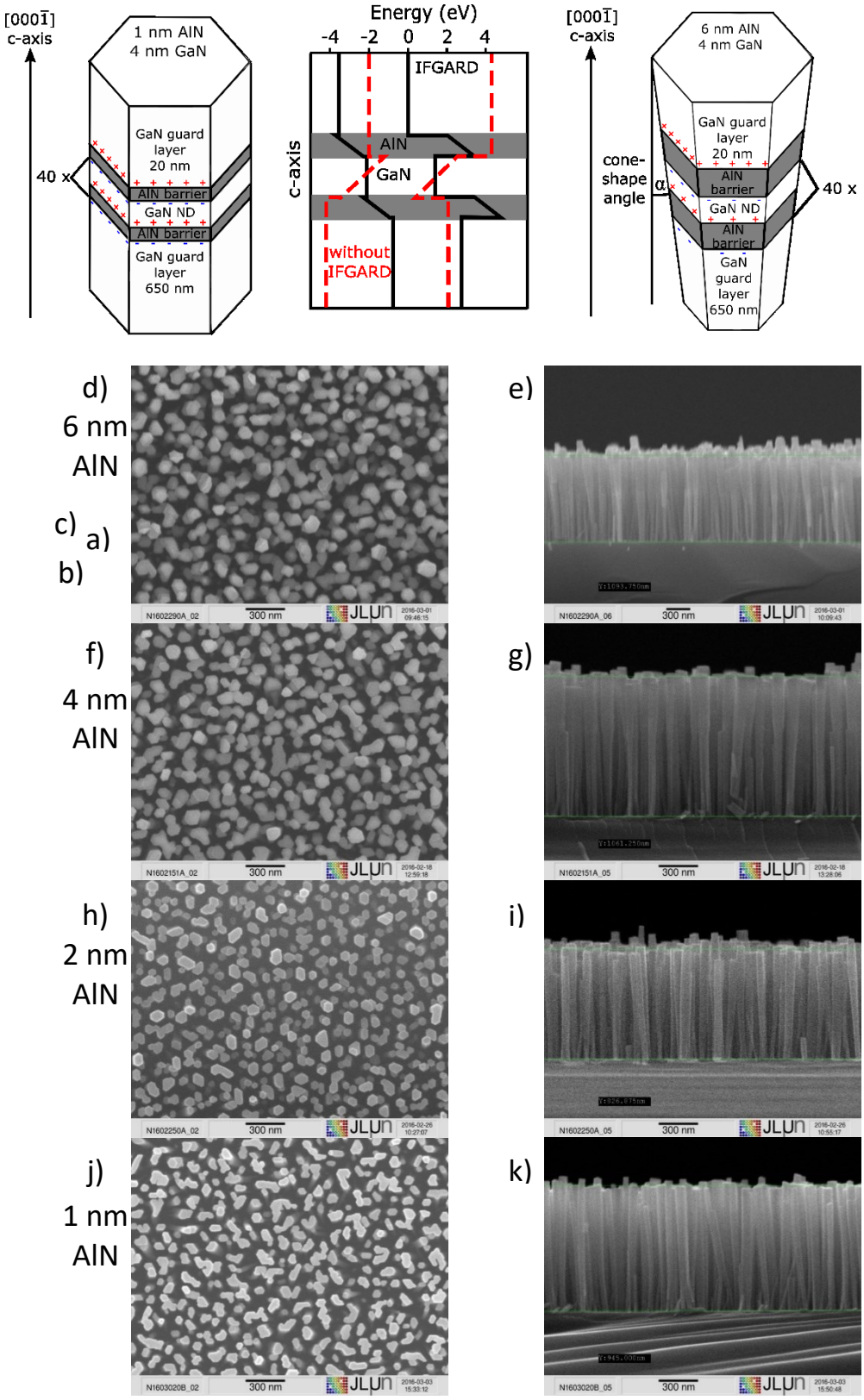

Figure 5.1: Schematic sketches of the NWs with AlN barrier thicknesses of 1 nm a) and 4 nm c), each with 4-nm-thick GaN NDs. Arithmetic signs (red +, blue -) mark the positions of interface space charges. b) shows the respective band structure for 1-nm-thick barriers illustrating the flat conduction and valance band edges (black) in comparison to a conventional structure without guard layers (red), which exhibits band banding due to the QCSE (calculated with the NextNano software) [45]*. d) to k) show SEM images of samples with AlN barrier thicknesses of 6 nm [d), e)], 4 nm [f), g)], 2 nm [h), i)] and 1 nm [j), k)] each with a ND thickness of 4 nm. The SEM images illustrate the changing cone-shape angle α and the coalescence of some NWs.*

The top view SEM images [Figure 5.1 d), f), h), and j)] reveal the typical hexagonal shape of wurtzite crystal based nanostructures. Noticeable, for the smallest barrier thickness of 1-nm AlN most of the NWs are coalesced [Figure 5.1 d), f), h) and j)]. This fusion of NWs leads to a higher possibility of structural defects in the affected region [74].

Due to the lateral growth of the AlN barriers, the nanowires exhibit a cone-shaped structure [Figure 5.1 c)] [75], [76]. Considering the conservation of a constant interface-charge density, the particular cone-shape leads to different net interface charges [red +, blue - in Figure 5.1 c)] at either side of each AlN barrier; because the top interface to the GaN is larger than the interface to the GaN below each AlN barrier. This total interface-charge discrepancy is the perfect feature to proof the influence of the IFGARD on the electric field within the NDs, as in this case the flatness of the band-edge [Figure 5.1 b)] depends on the barrier thickness - similar to what Hönig et al. discussed in Ref. [40] for IFGARD-based quantum dots. Hence, it becomes possible to control the built-in electric field in the NDs by adjusting the AlN barrier thickness and thus the net interface charges. Furthermore, thicker AlN barriers lead to a pronounced cone-shape of the whole nanowire further enhancing the built-in electric field strengths. The angle α of the cone-shaped nanowire in Figure 5.1 c) gets smaller with reduced AlN barrier thickness until the cone-shape turns into a straight shape [compare Figure 5.1 e), g), i), c) with k) and a)]. Consequently, we produced two samples series, a barrier series, where the AlN barrier thickness varies between 6 nm and 1 nm with a constant GaN ND thickness of 4 nm and a ND series with a constant AlN barrier thickness of 1 nm and varied GaN ND thicknesses of 3, 2, and 1 nm. As a ND thickness of 4 nm is very large if compared to the exciton-Bohr radius (effective Bohr-radius $a^* = \frac{m_e}{m^*}\varepsilon_r a_0$ [4], [77]–[81]), without built-in electric fields an emission energy close to the GaN band gap of approximately 3.5 eV is expected. Hence, for the barrier series (QCSE regime samples) with emission energies smaller than 3.5 eV a shift towards higher emission energies (limited by 3.5 eV) for decreased AlN barrier thicknesses is expected.

Starting with the thinnest, 1-nm-thick AlN barriers with minimized built-in fields in the NDs, the emission energy can be tuned to higher energies by means of the confinement effect when smaller ND thicknesses are used. Hence, the samples of this

series are called confinement regime samples. By utilizing these two series, it will be possible to separately investigate the influences of the QCSE and the confinement effect.

An obvious difference in the investigated samples to the IFGARD explained in chapter 4 is, that the Si (111) substrate of the investigated samples does not exhibit the same material as the NDs (GaN) and, therefore, does not represent an extension of the bottom guard layer. In general, IFGARD nanostructures should exhibit the same substrate material as used for the active region (here, GaN NDs), which has to be used for the guard layers too in order to avoid a negative influence of interface charges at the guard layer interface to the substrate. Nevertheless, the space charges at the bottom of the NWs (at the (111) Si to (0001) GaN interface) do not affect the built-in fields in the NDs, which is caused by the small lateral dimension of the NW pedestal: The Interface charges at the 40 nm measuring Si substrate to GaN NW pedestal interface can be considered as a point charge due to the large distance of 650 nm to the ND stack (thickness of the GaN bottom guard layer). The resulting net pedestal charge causes a field strength that diminishes over the 650 nm distance to the IFGARD-ND stack by r^{-3} and has therefore only a negligible influence on the entire ND luminescence. This point-charge approximation would not be valid for IFGARD QWs, where the distance to the wafer interface would be small if compared to the wafer diameter. Hence, in such QW samples the bottom hetero-interface should be avoided, e.g., by homo-epitaxial growth or a subsequent laser lift-off process [82], seeking to reestablish the fundamental symmetry of the IFGARD approach.

Table 5.2: NW diameter and length scales for different AlN thicknesses and a constant GaN ND thickness of 4 nm.

AlN barrier thickness	GaN NW diameter in nm	smallest NW diameter in nm	Biggest NW diameter in nm	NW length in nm (nominal)
1 nm	61	40	81	871
2 nm	73	53	101	912
4 nm	88	67	118	994
6 nm	94	73	118	1076

6 Analysis and discussion

In this chapter, a detailed analysis and discussion of the experimental results provide the evidence of the successful implementation of the IFGARD. Therefore, micro-photoluminescence (µ-PL) and time-resolved micro photoluminescence (TRPL) techniques were used, which were explained in chapter 3. This chapter 6 is split into three parts presenting the µ-PL, the TRPL data and a comparison of these data with the literature.

The different µ-PL spectra are discussed in terms of the influence of the samples' built-in electric fields, monolayer (ML), and alloy fluctuations, surface states, and ND states. Therefore, power and temperature dependent µ-PL measurements as well as scanning transmission electron microscopy (STEM) had been performed. The STEM results provide with their monolayer (ML) resolution a detailed insight into diameter variations of the NWs along the c-axis, into variations of the nanodisc thickness, and the AlN barriers, besides information regarding the interface between NDs and barriers.

The TRPL measurements show multi-exponential decay processes (see chapter 6.2). To classify the different recombination pathways in the IFGARD NWs, power and temperature dependent TRPL measurement as well as TRPL measurements as a function of the emitted energy are analyzed.

Finally, a comparison of the presented results with the literature will be given to demonstrate that the IFGARD shows emission energies like non-polar QWs. Such an elimination of the built-in electric field has never been shown before within nanostructure samples with a maintained wurtzite c-plane layered growth.

6.1 Micro-photoluminescence [45]

Figure 6.1 exhibits an overview of micro-photoluminescence (µ-PL) spectra for all samples recorded at an excitation power of 15 µW. The spectra are not normalized, hence, their absolute intensities can be quantitatively compared to each other. Please note that the excitation power of 15 µW does not represent the lowest used excitation power of 0.035 µW causing an already blue-shifted photoluminescence-peak position due to a partial QCSE screening by the excited charge carriers [83]–[85]

(compare the green marked data in Figure 6.14). 15 µW excitation-power spectra are chosen for this plot as they represent a trade-off between energetically well separated luminescence maxima for all samples with enough intensity to be plotted on a linear scale.

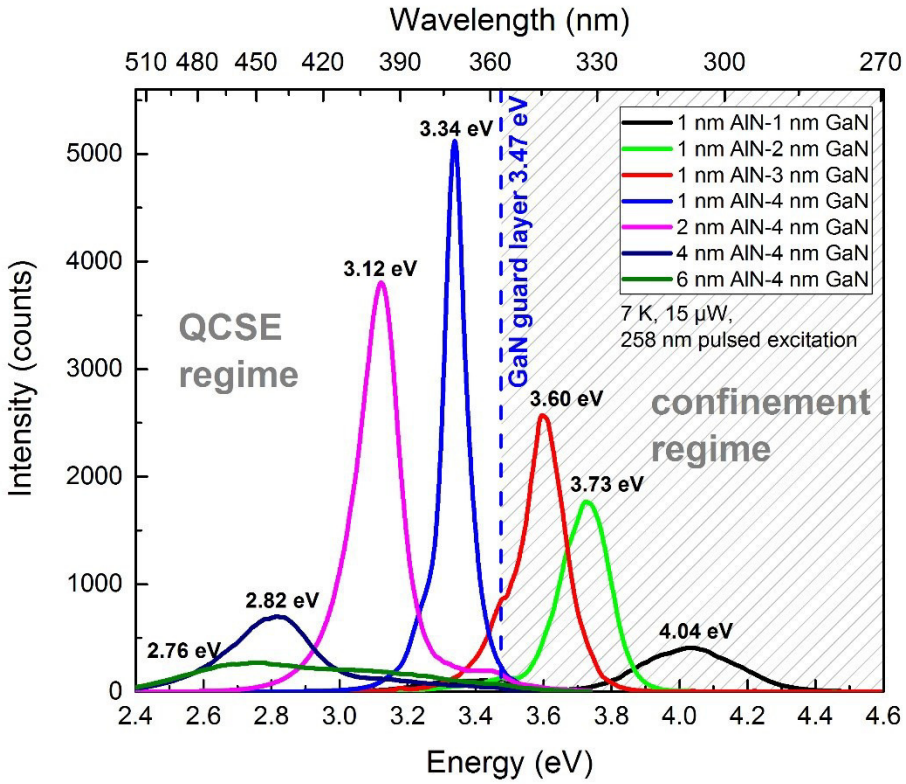

Figure 6.1: Comparison of µ-PL spectra for all investigated samples at 15 µW excitation power. In all samples, the dominant GaN ND luminescence is accompanied by the GaN-guard-layer luminescence (marked by the dashed, blue line), which divides the samples series into the so called QCSE regime and the confinement regime.

It is important to note that a 4-nm-thick GaN ND is not able to significantly quantum-confine excitons by its dimensions in absence of the QCSE [4], [77]–[79]. Therefore, all IFGARD samples with a ND thickness of 4 nm would (without the cone-shape of the embedding NWs) emit at a luminescence energy close to the free-exciton-emission energy of bulk GaN (3.48 eV [86], [87]). This free exciton emission energy is marked by the luminescence of the bulk-like GaN guard layers in all recorded spectra (blue, dashed line) and represents the transition between the QCSE and the confinement regime.

In Figure 6.1, the emission peak energy of the GaN-NDs in the QCSE regime (nominal GaN-ND thickness is constant at 4 nm with varied AlN-barrier thickness: 6 nm, 4 nm,

2 nm and 1 nm) shifts from 2.76 eV to 3.34 eV (for an excitation power of 15 µW) for decreased barrier thicknesses. Additionally, a drastic increase of the absolute intensity is observable with decreasing barrier thicknesses. Both, the emission energy shift as well as the intensity enhancement are caused by the reduction of the QCSE within the NDs. This gets confirmed by the decreased charge carrier screening of the built-in fields visible in the power dependent µ-PL measurements (chapter 6.1.3) and the drastically reduced recombination time in the TRPL measurements (chapter 6.2) with decreasing AlN barrier thicknesses.

Within the QCSE regime, the built-in electric field strength is a consequence of two effects: first, the unequally sized AlN-GaN interfaces due to the cone-shape of the NWs on either side of each AlN barrier lead to a non-zero net-polarization field inside the NDs, similar to the IFGARD quantum dot case theoretically described by Hönig et al. [40] as the total number of space charges on both interfaces differ from each other. Second, the pronounced cone-shape angle α (compare Figure 2.1) in the samples with thicker AlN barriers causes more unequal AlN-GaN interfaces further strengthening the net-polarization as explained in the first case. Hence, the whole QCSE regime features a strong dependence of the ND luminescence energy on the AlN barrier thickness in Figure 6.1 and strong screening effects by enhanced excitation powers, Figure 6.14.

Besides the aforementioned influence of the decreasing QCSE on the spectra in Figure 6.1, an increased overlap between the electron and hole occupation probability density is obtained, leading to an enhanced exciton-decay rate (chapter 6.2). In turn, this leads to a strong increase in absolute intensity for the samples with decreased AlN-barrier widths in the QCSE regime. Additionally, the decreased electric dipole moment of the exciton couples less efficiently to defect charge fluctuations in the ND vicinity as well as phonons, which is one mechanism that reduces the FWHM (770 meV for 6nm barrier widths compared to 83 meV for 1nm barrier widths) for the emission peaks of the samples related to the QCSE regime [18]. Another effect that causes the huge FWHM of 770 meV for the 6-nm-thick AlN barriers originates from a ND thickness variation from 3 nm up to 5 nm along the NW (see chapter 6.1.2.1).

Furthermore, the 1-nm-thick AlN barriers and 4-nm-thick GaN NDs exhibit multiple LO-phonon replicas (Figure 6.2, E_{LO} = 94 meV) whereas all samples within the confinement regime do not show any phonon replicas. In Figure 6.2 three LO phonon replicas with an energy of 94 meV as it is typical for GaN [88] are visible. While the visibility of multiple LO-phonon replicas implicates a large Huang-Rhys-factor and confirms the existence of built-in excitonic electric dipole moments [88] within the QCSE-regime NDs, their non-visibility for the confinement-regime NDs indicates the absence of a built-in excitonic electric dipole moment.

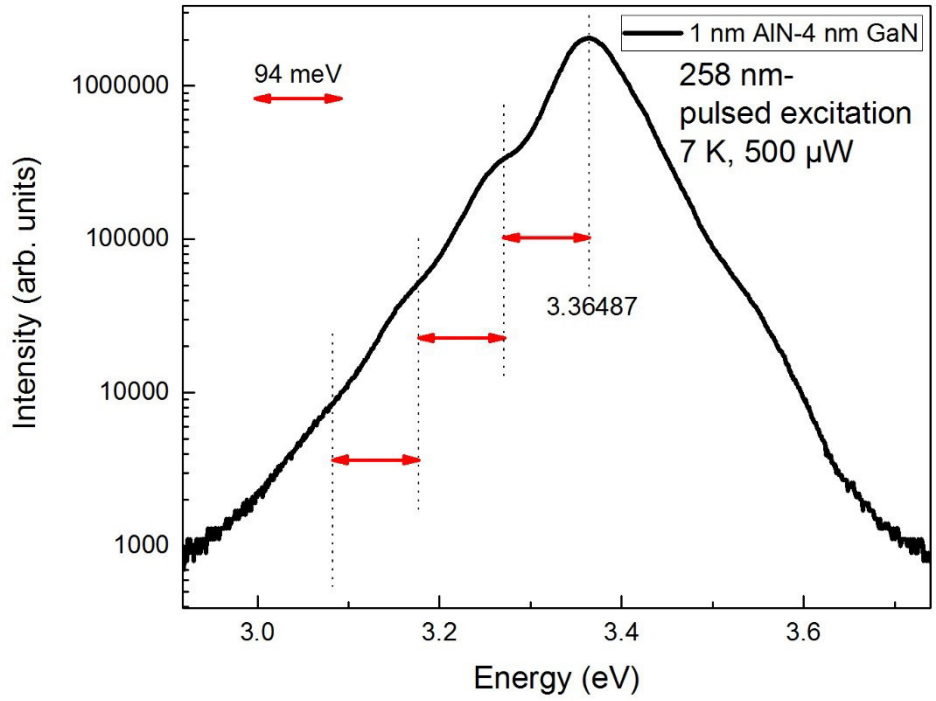

Figure 6.2: Multiple phonon replicas are visible for the 1-nm-thick AlN barriers sample within the QCSE regime only. The existence of multiple LO-phonon replicas indicates built-in excitonic electric dipole moments in the QCSE regime samples.

In Figure 6.1, the confinement regime samples show no indication of built-in fields and the overall emission blue shift from 3.60 eV to 4.04 eV for thinner NDs (thickness goes down from 4 nm to 1 nm) is solely caused by the quantum confinement without being affected by a counteracting QCSE red shift. This fact is demonstrated by the results of the power-dependent µ-PL measurements analyzed in chapter 6.1.3. Here, a screening of the internal electric field by excited charge carriers at high excitation powers becomes visible for the QCSE regime, but not for the confinement regime.

Nevertheless, the confinement regime samples are affected by a localized states filling effect resulting in an energy shift of up to 11 meV at high excitation power (see chapter 6.1.3). The findings for the confinement regime samples are similar to what was observed at non-polar GaN/AlN QWs, [29], [89]–[91] which, nevertheless, exhibit lower emission energies than the investigated IFGARD NDs.

When the thickness of the NDs in the confinement regime is decreased, the emission energy even exceeds 4 eV for moderately thin (1 nm) NDs due to the strong confinement in absence of the QCSE. However, the simultaneous reduction of the absolute intensity (for a constant pump power) can be straightforwardly understood: As the number of NDs (40) is conserved, the total photon- absorbing volume reduces together with the ND thickness. At the same time, the FWHM of the NDs' luminescence peaks within the confinement regime rises from 83 meV to 330 meV.

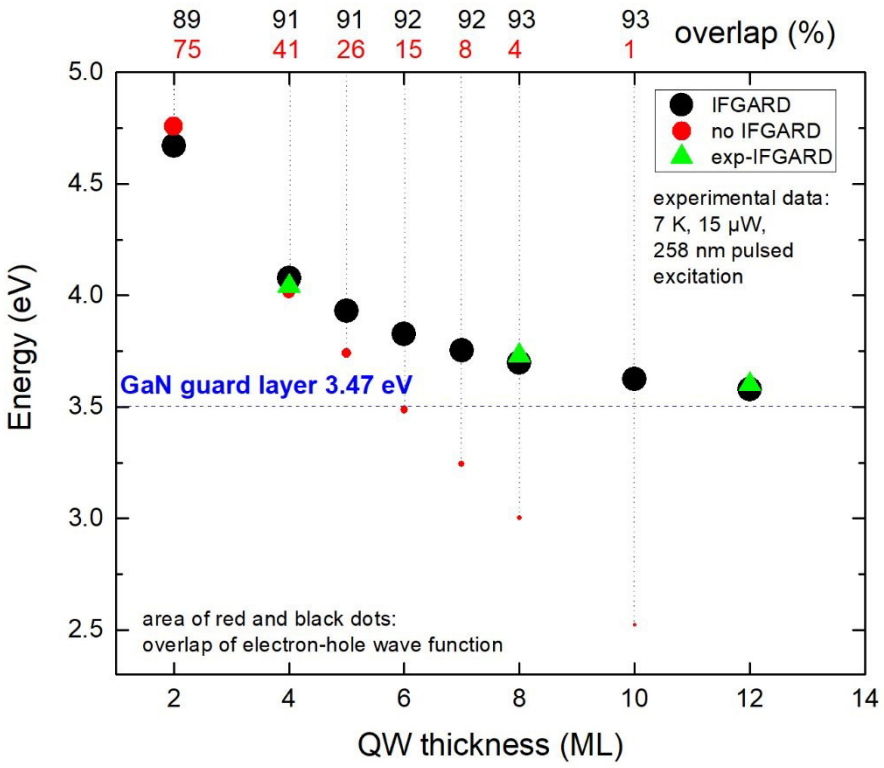

Figure 6.3: Comparison between numeric (black with IFGARD, red without IFGARD) and experimental data (green) illustrating the ND emission energies dependence on the ND thickness. Note, that the numeric "IFGARD" data was calculated for infinite quantum wells, hence, the built-in field strength was perfectly shielded (zero field strength). Whereas the calculated values for structures without IFGARD show an approximately linear trend crossing the GaN guard layer luminescence at 3.47 eV, the predicted IFGARD ND emission energies converge against the GaN guard layer luminescence. The Theoretical predictions for the IFAGRD are in perfect accordance to the experimental data recorded for the samples within the confinement regime–hence, these samples are without any built-in electric field.

This can be understood considering the quantitative STEM analysis (chapter 6.1.2.1) showing random ND-thickness fluctuations of ± 1 monolayer (ML) that have the strongest impact on the confinement energy of the excitons within the thinnest NDs (chapter 6.1.2.2.1 Figure 6.9) [92].

Figure 6.3 illustrates exciton emission energies in regard to the thickness of simulated IFGARD quantum wells (black dots) and conventional GaN quantum wells without the IFGARD layer sequence (red dots)[2] in an infinite AlN matrix. The experimentally determined emission energies of the samples with 1-nm-thick AlN barriers are included as green triangles. The varying sizes of the red and black dots are proportional to the electron-hole wave function overlap in % (the absolute values in % are given at the top horizontal scaling in black and red, respectively). While the "no IFGARD" data points follow an approximately linear decrease of the emission energy from 4.76 eV down to 2.52 eV with increasing QW thickness due to the QCSE, the IFGARD data points follow an approximately exponential trend from 4.67 eV down to 3.63 eV converging against the GaN guard layer luminescence energy of 3.47 eV (blue, dashed line) due to the pure quantum-confinement reduction. The QCSE-emission-energy redshift by 2.24 eV for the "no IFGARD" structures is accompanied by a decrease of the electron-hole wave function overlap from 75 % down to 1 %., which is approximately equivalent to a proportional decrease of the oscillator strength resulting in drastically reduced exciton recombination probabilities and large decay times in thicker conventional QWs/NDs. Remarkably, in comparison, the investigated IFGARD ND samples are expected to exhibit an insignificant increase of the overlap from 91 % up to 93 % besides their reduced redshift.

A perfect qualitative as well as quantitative agreement of the experimentally recorded emission energies of the confinement regime samples (green in Figure 6.3) with the numeric IFGARD data (black dots, with perfectly shielded built-in field strengths of zero) proves the pure influence of the confinement on the charge carriers in these samples without any QCSE. The samples within the confinement regime follow accurately the predicted emission energy shift in regard to the variation of the ND thicknesses. As the calculated electron-hole overlap for the three

[2] The numeric data in Figure 6.3 were calculated based on 8-band kp theory from Steffen Westerkamp, member of the working group of Prof. A. Hoffman in the Technischen Universität Berlin.

samples changes by approximately 2 % only, the found constantly short exciton life-times (presented in chapter 6.2) for the confinement regime samples can be understood.

6.1.1 Estimation of the electric field strength [45]

After having separated the QCSE from the confinement effect, the remaining internal electric field strength can be estimated for individual NDs of the QCSE regime simply by the energetic difference between the GaN-guard-layer-luminescence energy and the respective ND emission energy (Figure 6.4). This difference represents the energy of the electric dipole moment of one exciton in the built-in polarization field. As shown by Nakaoka et al. [93], the quadratic polarizability of the exciton is only of relevance for electric field strengths up to 100 kV/cm, causing energetic shifts of up to 3 meV. Therefore, we can safely neglect the polarizability of the ND exciton and roughly approximate it by a solid electric dipole moment. Here, we estimate the maximal possible dipole moment μ_z by the thickness of the NDs times the elemental charge e, being $\mu_z \approx 4\,\mathrm{nm} \cdot e$ for the QCSE regime [94]. Hence, the energetic luminescence offset to the 3.47 eV of the bulk-like GaN guard layers $E_{GaN} - E_{ND} = \mu_z F_z$ [95] has to be divided by μ_z to give an easy approximation of the built-in field strength (Figure 6.4). This approximation should become more reliable for higher field strengths, as the true electric dipole moment of the exciton converges towards the approximated $4\,\mathrm{nm} \cdot e$ with higher field strengths. Nevertheless, the estimated 2.61 MV/cm in the IFGARD QW with 6-nm-thick AlN barriers are still more than two-times smaller than the field strengths in comparably thick conventional GaN/AlN QWs [26], [96], [97]. Although, this discrepancy might lead to the assumption of smaller electric dipole moments, i.e., $\mu_z < 2\,\mathrm{nm} \cdot e$ this would be unrealistically small for a 4-nm-thick ND, demonstrating the IFGARD effectively reducing the field strength in all samples.

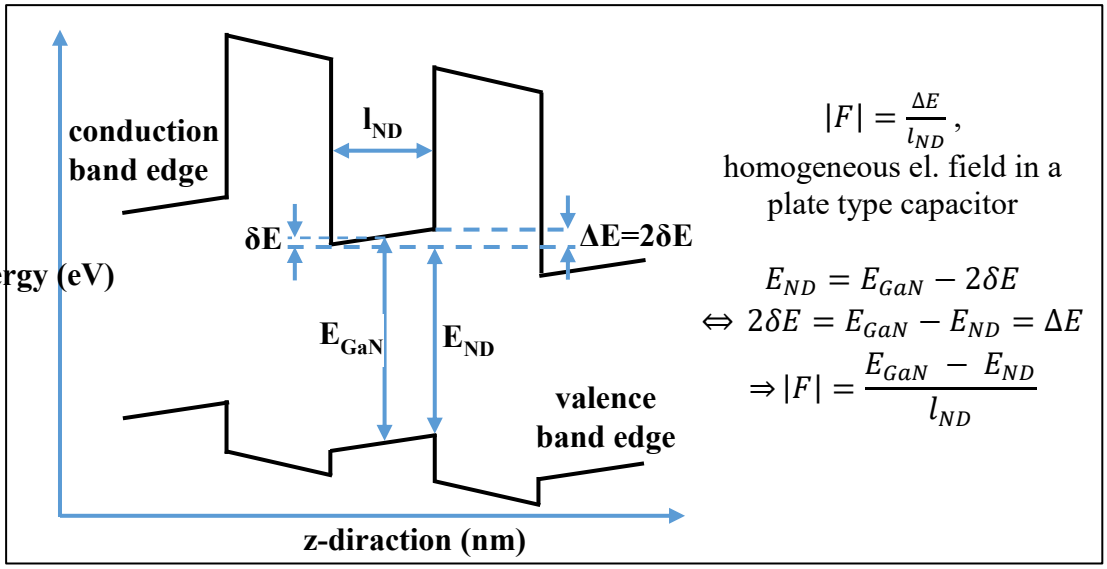

Figure 6.4: Approximation of the electric field strength for the QCSE regime samples showing the conduction and valance band edges for one ND in the z-direction with the ND thickness l_{ND}, the emission energy of the ND E_{ND}, the energy of the GaN guard layer E_{GaN} and the potential drop ΔE, besides, the equation for a homogeneous electric field in a plate type capacitor.

In Figure 6.4, the conduction and valance band edges for one ND together with the plate type capacitor approximation are sketched along the polar z-/growth-direction. In the picture, the ND thickness l_{ND}, the emission energy of the ND E_{ND}, the energy of the GaN guard layer E_{GaN} and the potential drop ΔE is shown. As the emission energy of the NDs within this approximation is directly proportional to the field strength, a clear tend – a decreasing electrical field for thinner AlN barriers – is derived as shown in Figure 6.5.

Figure 6.5 shows the increasing electric field strength from 0.38 MV/cm for the 1-nm-thick barriers up to 2.61 MV/cm for the 6-nm-thick barriers in the QCSE regime. Be aware, that due to the large thickness of the NDs, the excitons should not show a significant blue shift by quantum confinement and therefore should emit with an emission energy identic to the visible top GaN guard layer luminescence leading in this approximation to a field strength of zero.

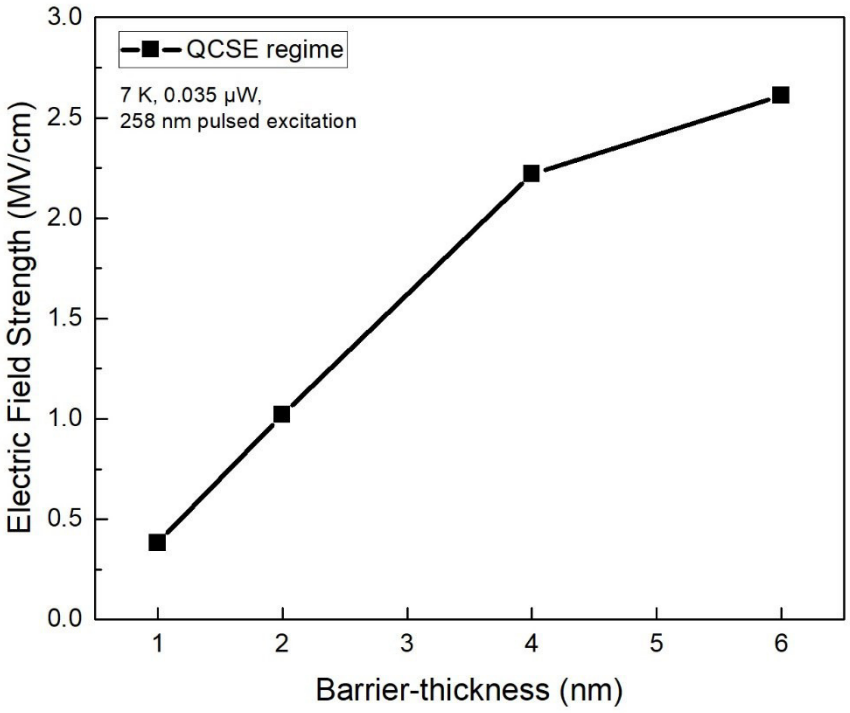

Figure 6.5: Estimated electric field strength vs. barrier thickness showing a decreasing electric field strength with a decreasing barrier thickness in the QCSE regime.

6.1.2 Influence on the changing full width at half maximum

This section discusses the origin of the FWHM dependence on emission energies in the spectra exhibited in Figure 6.1. Especially for the confinement regime samples, it needs to be discussed why the FWHM starts to increase again (chapter 6.1.2.2). The recorded spectra of the NW ensembles are a superposition of hundreds of stacked NDs each broadened by ND thickness fluctuations (ML fluctuations) [98]–[101]. Hence, STEM analyses were carried out to investigate this issue.

6.1.2.1 Scanning-transmission-electron microscopy [45]

To investigate alloy fluctuations, monolayer fluctuations or the influence of structural defects in the 40 times stacked NDs, scanning-transmission-electron microscopy (STEM) measurements were carried out[3]. STEM-images were recorded with a high-angle annular dark field detector (HAADF) for the 6-nm-thick and 1-nm-thick AlN

[3] The experiment as well as the data representation were done by Dr. Tim Grieb in the University Bremen.

barrier NWs, exemplarily. Therefore, the NWs were dispensed in isopropanol and transferred to a graphene TEM grid.

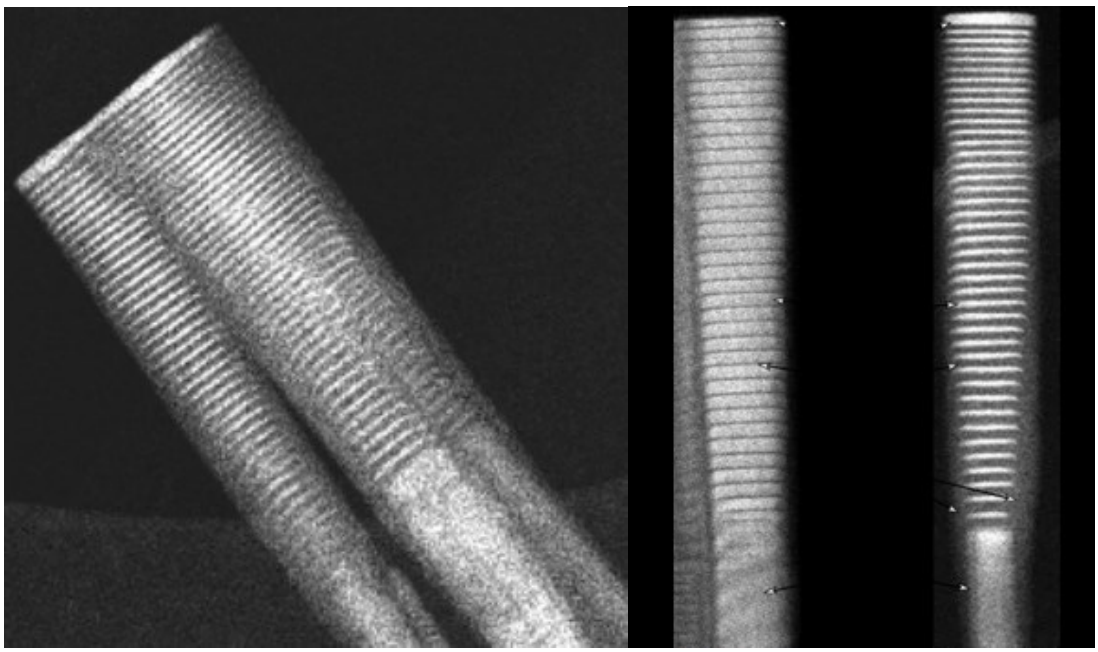

Figure 6.6: STEM image of three coalesced NWs with 6-nm-thick AlN barriers and 4-nm-thick GaN NDs (a). b) shows a comparison of NWs with 6-nm- and 1-nm-thick barriers with 4-nm-thick NDs each. Marked are the GaN guard layer, the GaN NDs (bright), the AlN barriers (dark), and the AlN shell.

Figure 6.6 (a) shows an example of three coalesced NWs with 6-nm-thick AlN barriers. Such coalesced NWs were already visible in the SEM top view images (see Figure 5.1d). Figure 6.6(b) directly compares a 6-nm-thick with a 1-nm-thick AlN barrier NW. The 40 NDs, the guard layers, the AlN barriers and the AlN shell are clearly resolved nicely showing the alternating, plain layers without structural defects. In contrast to the SEM images, here, a quantitative structure analysis is possible. For this purpose, the NDs in the two specific single NWs shown in Figure 6.6 were analyzed. (For the SEM analyses hundreds of NWs were measured to obtain an average diameter.) The STEM analyzed two NWs in Figure 6.6 exhibit different cone-shape angles. For the 6-nm-thick AlN barriers, the diameter increases from 38 nm at the bottom to 74 nm at the top of the NW. However, the 1-nm-thick AlN barrier NW shows a much smaller increase of the diameter from 28 to 36 nm. This is equivalent to the decrease of the cone-shape angle α for thinner barrier thicknesses as previously found by the SEM analyses (see Figure 5.1). Furthermore, the AlN shell [102] of the NWs with 6-nm-thick barriers features a thickness of 10.5 nm at the bottom and 1.3 nm at the top of

the NW. Figure 6.6 b) shows that the shell purely consists of AlN, as it was demonstrated by energy-dispersive X-ray spectroscopy (EDX) for similar samples grown by the same group [102] that produced the IFGARD samples investigated in this work. Figure 6.7 shows a detailed analysis of the thicknesses of barriers and NDs along the two NWs. For both barrier thicknesses, 6 nm and 1 nm, the ND thickness as well as the barrier thickness reduces towards the top of the NW. Such a thickness variation may occur from a change in the growth rate with time [98]. The thickness of the nominally 6-nm-thick AlN barriers decreases by approximately 4 nm much more than the thickness of the 1-nm-thick AlN barriers (<1 nm) (see Figure 6.7, red). The ND thickness variation is less affected than the AlN barrier thickness, showing only a slight total decrease of approximately 1 nm for the nominally 6-nm-thick barrier sample after 40 ND stacks and an almost constant ND thickness of 5 nm for the 1-nm-thick barriers, except for the first and last ND. Despite the deviation between the nominal and the real ND and barrier thicknesses, the nominal thicknesses are retained for the further description in this thesis.

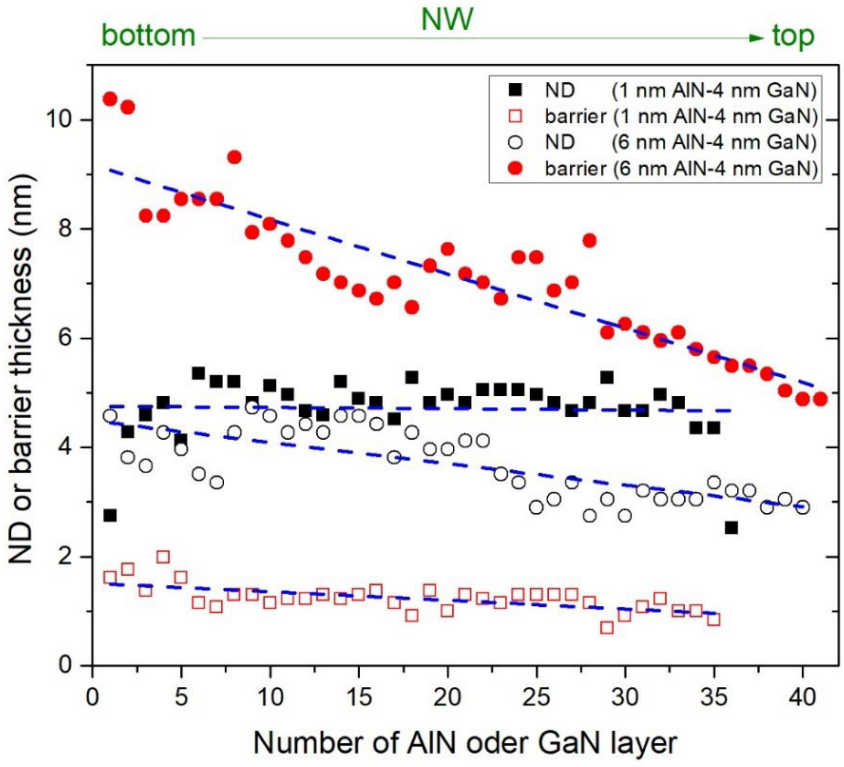

Figure 6.7: Systematically measure of the NDs thickness along one NW for the 6-nm and 1-nm-thick AlN barriers.

Figure 6.8 shows a color-coded mapscan of the Al concentration [dark red for “100 % Al” (pure AlN), dark blue for “-20 % Al”, while 0% Al represents pure GaN] within a section of a NW with nominally 6-nm-thick AlN barriers. In growth direction, the AlN-GaN and the GaN-AlN interfaces exhibit different color gradients. The GaN-AlN interfaces (the upper parts of the blue regions) exhibit longer color gradients in comparison to the AlN-GaN interfaces (the bottom parts of the blue regions). However, the color gradients of the Al profile can be interpreted either as an interdiffusion of Al and Ga ions, a beam spread due to the high specimen thickness [102], an interface roughness, an electron beam that was not parallel to the interfaces caused by the cone-shape of the NWs, or an interface bowing near the lateral side-facets of the NWs with the AlN shell. Reference [102] investigated similar NW-ND structures and assigned such interface gradients to an alloy intermixing ($GaN/Al_{0.5}Ga_{0.5}N$), as the authors otherwise could not explain the deviation between their theoretically estimated electric field strengths for GaN/AlN NDs and the experimentally detected ND emission energies. In the here investigated samples, the Al profile is interpreted as a thickness fluctuation. This is supported by the perfect fit of the emission energies recorded for the confinement regime samples to the numeric simulations without electric field in Figure 6.3.

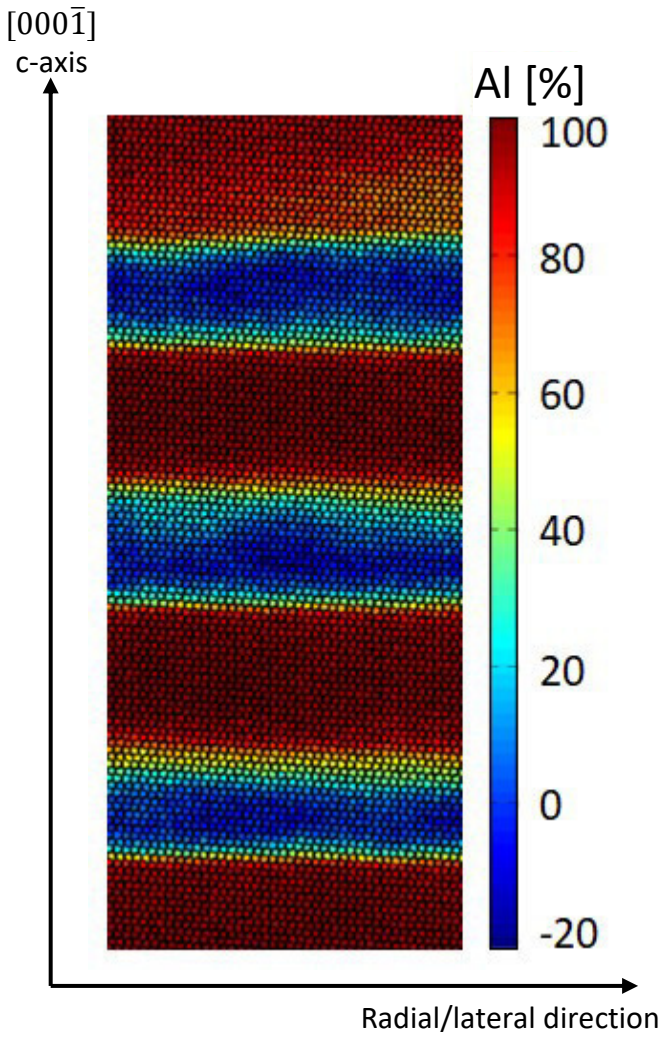

Figure 6.8: Color coded Al concentration dark red for "100 % Al" representing pure AlN, dark blue for "-20 % Al", while 0 % represents pure GaN) in a section of a NW with nominally 6-nm-thick AlN barriers.

6.1.2.2 Nanodisc thickness fluctuations

The STEM analyses in chapter 6.1.2.1 showed an interface roughness of about 1 to 2 monolayers (ML). This roughness was attributed to ND thickness fluctuations in the order of 1 ML which is for 1 to 2 monolayers equivalent to alloy intermixing as only two neighboring metal ions have to switch their places in both cases. Additionally to the interface roughness, a constant ND thickness gradient along the stack of 40 NDs was determined especially for the sample with nominal barrier thicknesses of 6 nm. However, these two different types of thickness fluctuations will be called: the normal and the QD-like ML fluctuation. The normal ML fluctuation is caused by the ND thickness variation along the whole NW while the QD-like ML fluctuation is

associated with the rough interfaces between the GaN and AlN layers within a single ND.

6.1.2.2.1 Normal monolayer fluctuation

In order to estimate the energetic impact of a ND thickness fluctuation of 1 to 2 MLs, numeric simulations of the emission energies of IFGARD QW structures are used and compared to experimental data recorded for the samples with nominally varied ND thicknesses from 4 down to 1 nm, see Figure 6.3. Table 6.1 lists the calculated emission energies. Here in this table, the numerically determined emission energy variation by the ML fluctuations is applied to the experimental data too. For the experimental data, the emission energies at 500 µW excitation power were used, as this reduces the effect of built-in fields in the 4 nm thick ND sample (compare chapter 6.1.3). Figure 6.9 illustrates the corresponding FWHM broadening that can be caused by these ML fluctuations. Due to the exponential raise of the confinement energy of confined charge carriers in smaller NDs, the FWHM broadening due to ML fluctuations is asymmetric, with a bigger broadening at the high energy side of the ensemble luminescence peaks. The exponential raise of the confinement energy with reduced ND thickness also causes a much larger influence of the ML fluctuation on thinner (2- or 1-nm-thick) NDs if compared to thicker (3- and 4-nm-thick) NDs.

Table 6.1: Energetic influence of 1 and 2 ML fluctuations on the ND luminescence estimated from numeric calculations (compare Figure 6.3) and applied to the experimental data.

nominal GaN (1 nm AlN)	1 nm 4 ML	2 nm 8 ML	3 nm 12 ML	4 nm 16 ML
numeric				
E_{-2ML} (eV)	4.667	3.820	3.625	3.547
E_{-1ML} (eV)	4.323	3.745	3.600	3.536
E (eV)	4.089	3.695	3.579	3.525
E_{+1ML} (eV)	3.929	3.660	3.562	3.517
E_{+2ML} (eV)	3.820	3.637	3.547	3.509
experimental (at 500 µW exc.)				
E_{-2ML} (eV)	4.612	3.857	3.657	3.387
E_{-1ML} (eV)	4.268	3.782	3.631	3.375
E (eV)	4.034	3.732	3.610	3.365
E_{+1ML} (eV)	3.874	3.697	3.593	3.356
E_{+2ML} (eV)	3.765	3.674	3.579	3.349

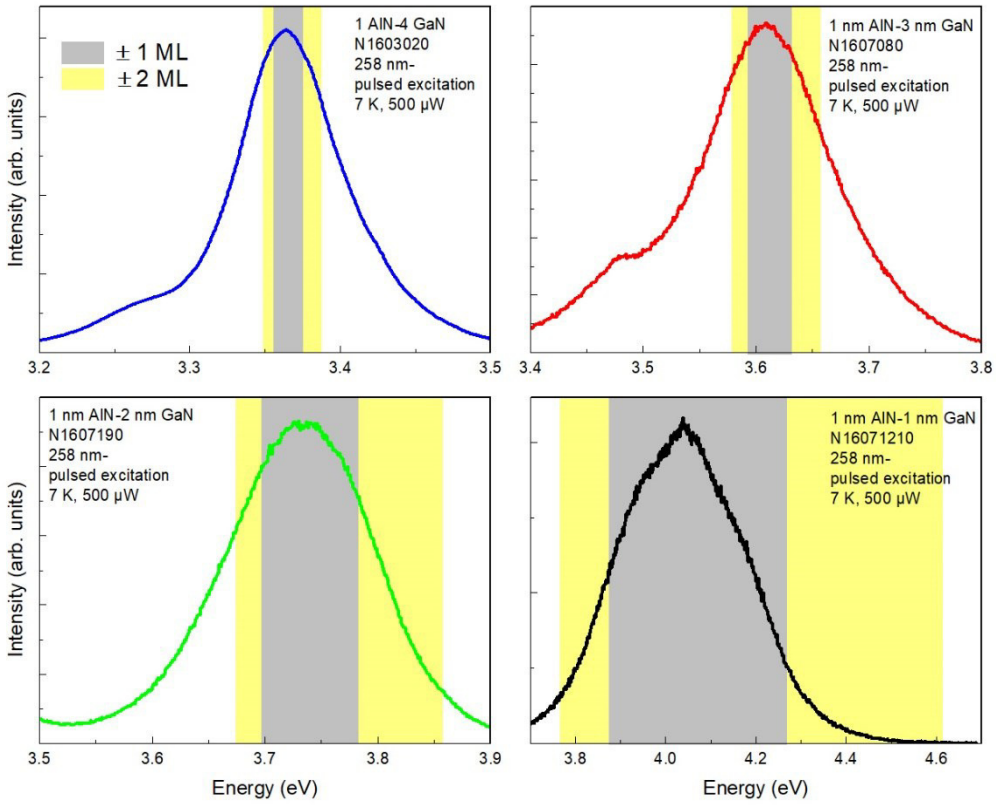

Figure 6.9: Impact of 1 (gray) and 2 (yellow) ML fluctuations on the ND emission peak. The values for the ML fluctuations stem from the numeric calculations in Figure 6.3.

However, the ML fluctuations cannot totally explain the remaining, comparably small FWHM of the 3- and 4-nm-thick NDs. For these NDs, the impacts of lateral nanowire surface states and QD-like ML fluctuations have to be considered. Especially surface states need to be taken into account as for NWs the surface-to-volume ratio is huge if compared to bulk material (see 6.1.2.3). Strain effects can be ruled out, as NWs benefit from a negligible residual strain contribution [103], [104] due to the small interface to the substrate and their extreme aspect ratio.

6.1.2.2.2 Quantum dot-like monolayer fluctuations

Additionally to the normal ML fluctuations explained in section 6.1.2.2.1, a ND thickness fluctuation can also exhibit quantum dot (QD)-like properties. This QD-like behavior was first reported by Arita et al. [105] for thin, single GaN/AlGaN QWs grown by MOCVD on sapphire (0001) substrates. As the QD-like behavior resulted from thickness fluctuations of a QW, these QDs do not need low growth temperatures [105] like QDs produced by the Stranski Krastanov method. The

differentiation between such QD-like ML fluctuations and the normal ML fluctuations will be revisit when interpreting the TRPL results. The emission energy of QD-like ML fluctuations strongly depends on the lateral and vertical dimensions of the ND thickness fluctuation changing the confinement of the electronic states. Therefore, the luminescence of the QD-like ML fluctuations is going to be spread over the ND luminescence. Nevertheless, in order to trap the charge carriers in the QD-like ML fluctuations, the charge carriers have to have a smaller energy within the QD-like ML fluctuations than within the ND and therefore, their luminescence must be concentrated on the low energy side of the emission peak. Hence, the maximum and the high energy side of the emission is dominated by the true ND emission, which (considering the large lateral dimension of the NWs) will exhibit quantum well like luminescence properties (see chapter 6.2).

6.1.2.3 Surface states

Surface states originate from the interruption of the crystal lattice periodicity at the boundaries of the crystal. Therefore, they can occupy energetic levels within the band gap that are forbidden in the continuous crystal lattice. The excitons bound to those surface states lay energetically below the free excitons. In the investigated NDs, their energetic position depends on the positon of the surface state in the forbidden zone of GaN, which can also be interpreted as a binding energy, like for the case of donor or acceptor bound excitons. Surface states are typically found in NWs where they have a high impact on the emission peaks due to the comparably large surface-to-volume ratio. The intensity ratio of the surface bound excitons to the ND excitons depends on the diameter of the investigated NWs. With decreasing NW diameter, the intensity of the surface bound excitons increases relative to the ND excitons. Already Brandt et al. [103] found, that the broadening of the emission peak of an ensemble of NWs is related to the different surface bound excitons of each individual NW.

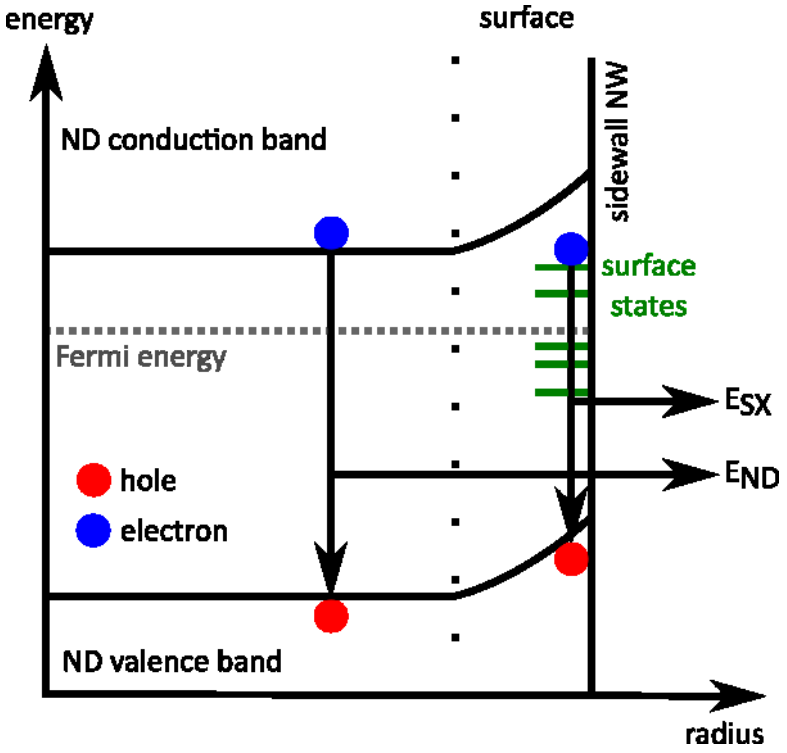

Figure 6.10: Cross section through a NW illustrating the energy vs. radius of the NW. The valence and conduction band as well as the fermi energy, the surface and the sidewall of the NW is sketched. The crystal lattice symmetry break at the sidewall leads to surface states within the bandgap, highlighted in green. The electrons (blue) and holes (red) occupy either the ND conduction band and valance band states with the emission energy E_{ND} or the electrons occupy the surface states within the bandgap (green) and recombine with a hole in the valance band with the emission energy E_{SX}.

Figure 6.10 sketches the energetic states that can be found along the radius of a ND. As illustrated, some surface states are located below the fermi energy and are occupied by electrons. Those occupied surface states induce a band edge bending to higher energies by the negative charges of the bound electrons. The band edge bending is similar to the situation at a Schottky barrier [106], [107] besides the absence of a metal causing the band bending within the semiconductor by its high work function.

By comparing the normalized low and high excitation power spectra of the confinement regime samples the saturating luminescence of the surface bound excitons and QD like states becomes distinguishable from the ND luminescence. This comparison is presented in Figure 6.11, where the saturating luminescence of those states is marked by blue hachures, being energetically positioned at the energetically lower flank of the peak as it was expected due to the band diagram in Figure 6.10. The compared spectra have been smoothed by a FFT-smoothing and normalized to

the maximum peak value. At 3.47 eV the GaN guard layer luminescence is visible in all spectra.

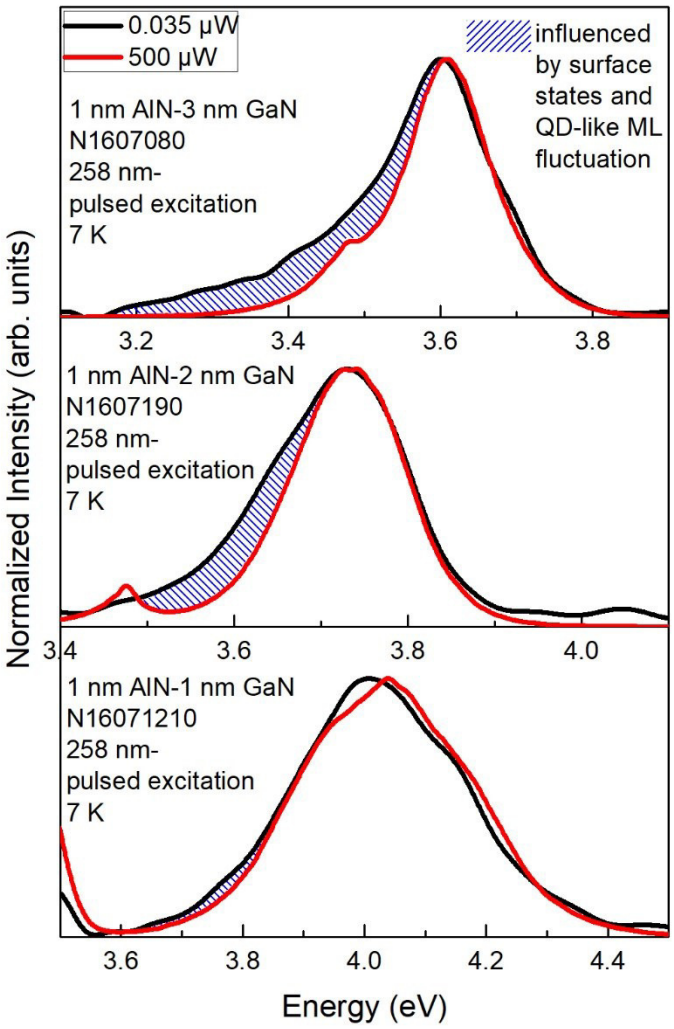

Figure 6.11: Comparison of the sample spectra at low (black) and high (red) excitation powers with normalized intensities. The dashed area decreases for high excitation powers relative to the high energy sides of the peaks. This can be explained by a saturated filling of the surface states and QD like states with excited charge carriers.

The saturation of the low energy side of the ND luminescence for high carrier injection and therefore the smaller contribution of this low energy area to the peak at high excitation powers, mimics a slight blue-shift of the luminescence peak (as will be discussed for Figure 6.14) besides a decreasing FWHM of 0.04 eV, 0.035 eV, 0.01 eV for the samples with 3, 2, 1 nm ND thickness. The saturation effect is similar to a band filling effect in semiconductors for high excitation powers while the smaller FWHM reduction of only 0.01 eV for the thinnest 1-nm-thick NDs represents the

increasing domination of the normal thickness fluctuations for the overall peak broadening (see 6.9).

6.1.2.4 Spectral separation between the influence of monolayer fluctuations and surface states

The recorded spectra of the NW ensembles are a superposition of hundreds of stacked NDs each broadened by ND thickness fluctuations (ML fluctuations) and surface states besides possibly involved, energetically higher excited states of the NDs also contributing to the total FWHM of each sample.

Figure 6.12 summarizes the different fractions contributing to the FWHM of the samples within the confinement regime. The figure illustrates the measured FWHM (black) and the calculated (red) broadening a normal ML fluctuation of 1 ML is expected to produce. The green squares represent the deviation between the experimental and the theoretical values showing the already discussed decreasing influence of normal ML fluctuations with increasing ND thickness. The negative value for the thinnest 1-nm-thick ND indicates, that the FWHM broadening for ND thicknesses up to around 1.5 nm can be fully explained by the dominating effect of the ND-thickness fluctuation called normal ML fluctuation. For thicker NDs, the contributions of surface states and QD-like ML fluctuations rise, quantified by the blue marked area.

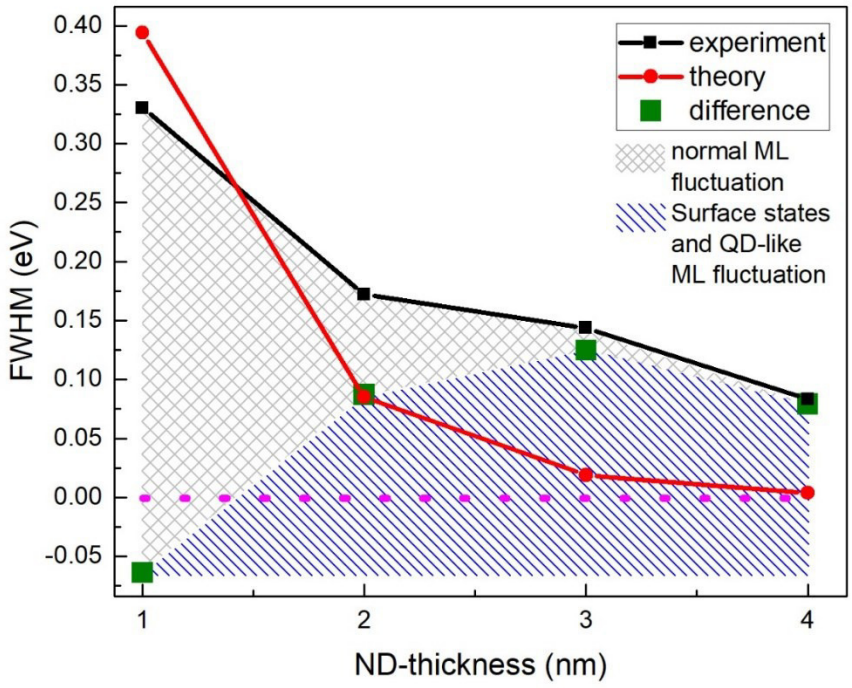

Figure 6.12: Influence of the different broadening mechanisms – normal ML fluctuation (gray), surface states and QD like ML fluctuation (blue) – on the FWHM. The black squares represent the measured FWHM and the red dots the calculated FWHM caused by 1 ML of normal ML fluctuation. The green squares mark the deviation between the experimental and calculated values representing the fraction of the broadening caused by QD-like fluctuations and surface states.

6.1.3 Power dependent photoluminescence [45]

One powerful and at the same time uncomplicated method to investigate the electric field strengths built-into the NDs as a consequence of the QCSE, is to record the power dependence of the photoluminescence spectra as such built-in fields would be screened by higher numbers of charge carriers excited in the samples. Therefore, Figure 6.13 shows the power dependent PL spectra for all investigated samples. Besides the already discussed features, like the GaN guard layer peak and the GaN ND luminescence, an increase of the absolute as well as integrated intensities and for some of the spectra a shift to higher emission energies with higher excitation power is observable. For a better overview, the energetic shift of the peak maxima, the development of the FWHM, and the increase of the integrated intensity with the excitation powers are plotted in Figure 6.14, Figure 6.15 and Figure 6.16, respectively.

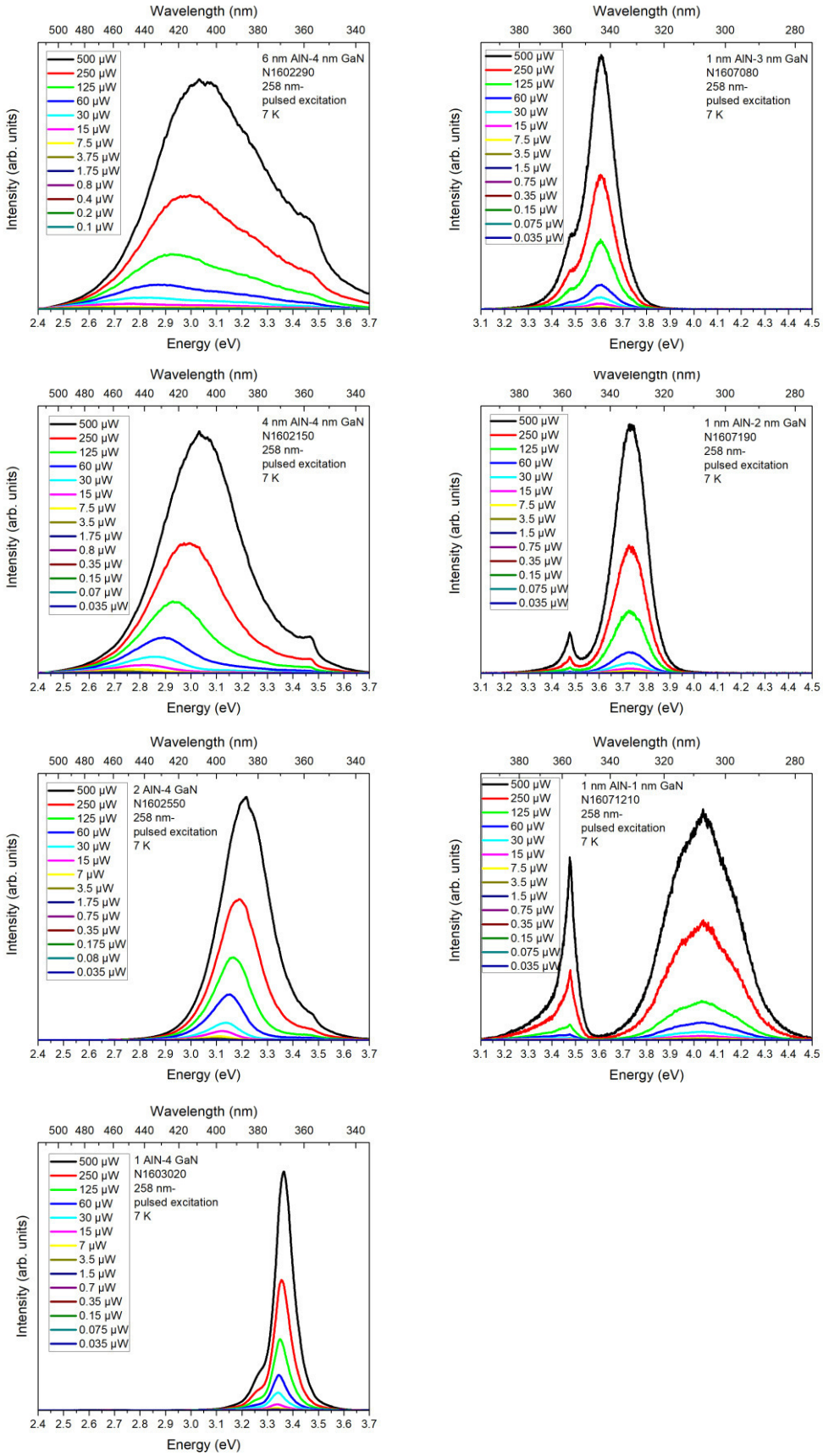

Figure 6.13: Power dependent µ-PL spectra for the QCSE (left column) and the confinement regime (right column) samples.

Figure 6.14 reveals the influence of the excitation-pump power being varied more than 4 orders of magnitude from 0.035 µW up to 500 µW on the energetic position of the respective emission peak maximum of the ND luminescence stemming from the different samples. On the right, vertical axis (blue), the total emission-energy shift is noted. This total shift represents (for the samples of the QCSE regime) the achieved QCSE screening by the excited charge carriers. However, in the case of the samples within the confinement regime, this is only a virtual shift of the maxima caused by the shrinking of the FWHM due to saturation of the QD-like ML fluctuations and surface states at the low energy flank of the peaks. Gray hachures divide the IFGARD samples with negligible QCSE [with (virtual) total emission-energy shifts < 15 meV] from those sample curves still being affected by the QCSE into the confinement and QCSE regime, respectively. The QCSE regime lays energetically below the bulk-like GaN luminescence of the guard layers and the total emission-energy shift reduces with decreasing AlN-barrier widths from 904 meV down to 42 meV. In comparison, the samples within the confinement regime show a noticeably smaller total emission-energy shift between 14 meV and 11 meV, representing a purely virtual effect.

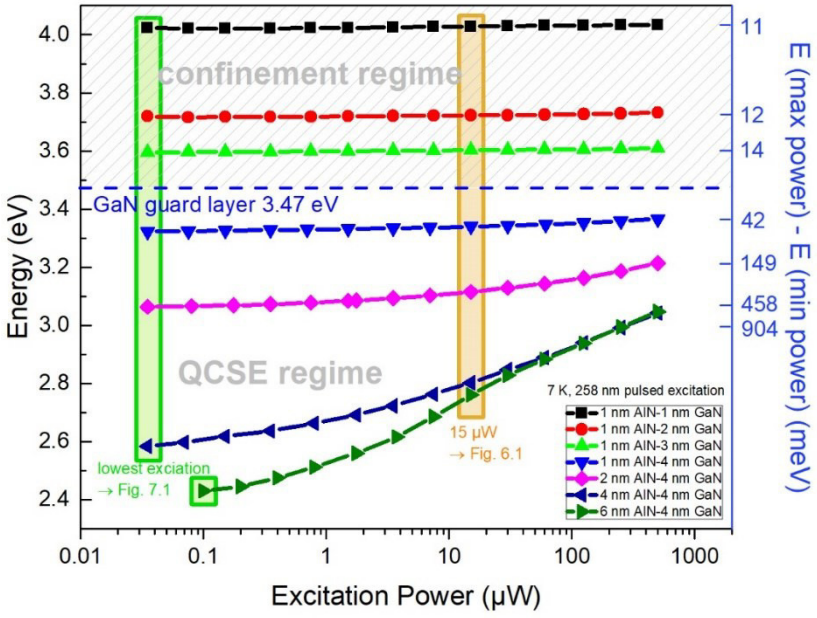

Figure 6.14: ND emission peak positions are plotted for excitation powers between 0.035 µW and 500 µW. The total emission energy shift between the lowest (min) and highest (max) excitation power is given on the right, vertical axis (blue) representing the achieved polarization field screening by excited charge carriers for the samples within the QCSE regime only.

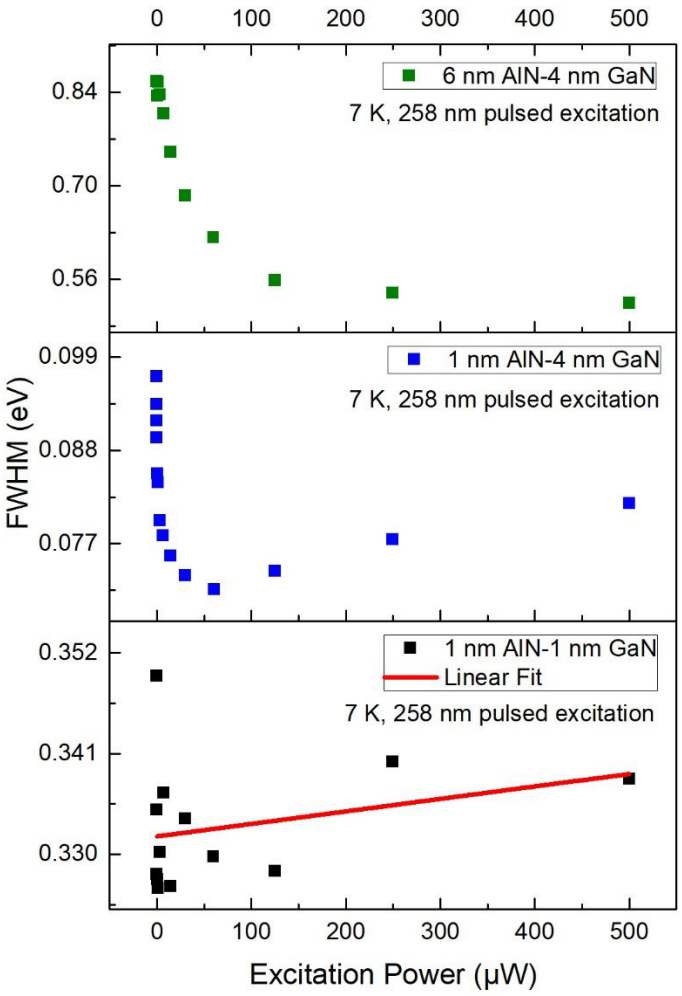

Figure 6.15: FWHM vs. excitation power for the 6-nm and 1-nm-thick AlN barriers samples in the QCSE regime and the 1-nm-thick GaN ND sample in the confinement regime showing three different trends over excitation power.

Interestingly, the FWHM dependence on the excitation powers, which is exemplarily shown for the 6 nm AlN with 4 nm GaN NDs, the 1 nm AlN with 4nm GaN NDs, and the 1 nm AlN with 1 nm GaN NDs samples in Figure 6.15 reveals very different dominant luminescence processes within the samples of the different regimes (QCSE vs. confinement). For the 6 nm AlN with 4 nm GaN NDs sample, the FWHM continuously narrows from 855 meV down to 524 meV, which is attributed to the free carrier screening of the built-in field with higher excitation powers. With reduced QCSE, thicker NDs emitting at the low energy side of the ensemble peak shift to higher emission energies, which leads to the reduction of the FWHM. The FWHM of the 1 nm AlN with 4nm GaN NDs sample, within the QCSE regime shows a different power dependence. First, the FWHM continuously decreases, before it starts raising

again for excitation powers exceeding >61 µW. The first decrease of the FWHM is caused by screening of the built-in field combined with a filling of the surface states and QD-like ML fluctuations on the low energy side of the peak. After 61 µW, the localized states are completely filled. Consequently, the increase of the FWHM above 61 µW of excitation power can be interpreted as a band-filling effect of the ND states by excited charge carriers [119], [120] further increasing the FWHM until the maximum excitation power of 500 µW is reached. Such an asymmetric filling effect of the surface states and QD-like ML fluctuations on the low energy side of the peak can also mimic a shift to higher emission energies of the peak maximum, as it is found for the samples in the confinement regime. For the confinement regime, the FWHM power dependence of the 1 nm AlN with 1 nm GaN NDs sample is exemplarily shown in Figure 6.15. Here, a spread of values around an approximately constant FWHM is visible. Nevertheless, the linear fit shows a slight slope of 14 meV/mW, which indicates a peak broadening due to the band filling of the ND states.

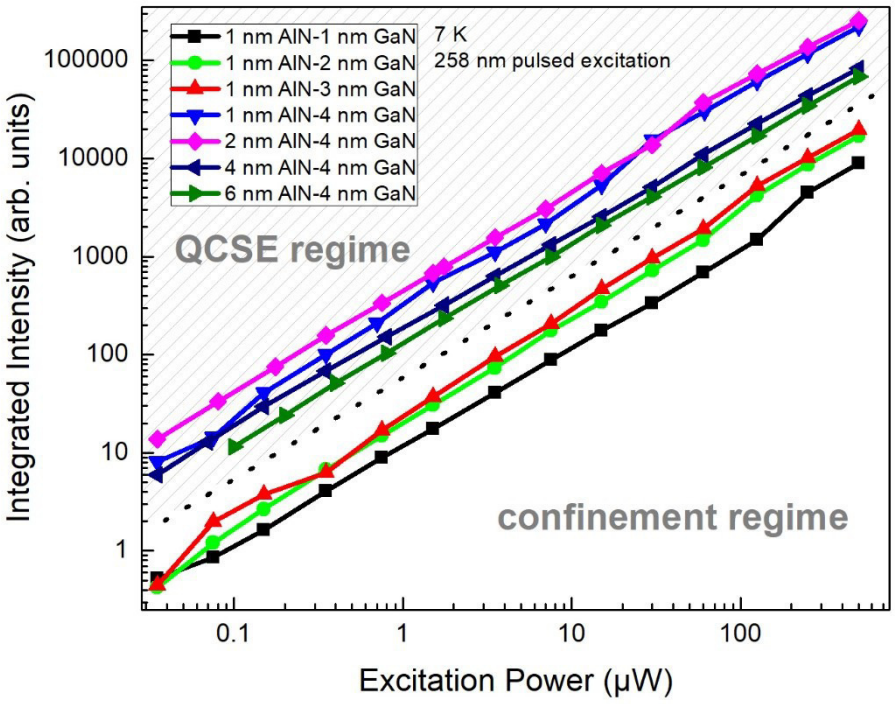

Figure 6.16: Integrated intensity vs. excitation power for the QCSE and confinement regime. The linear dependency in this double logarithmic plot proves the dominance of radiative recombination processes in all of the samples.

In Figure 6.16 the integrated intensities of the ND luminescence in all samples is plotted vs. the excitation power. However, for the 3-nm-thick ND sample (confinement regime) and the 4-nm-thick ND sample with 1 nm AlN (QCSE regime) the ND luminescence can hardly be separated from the GaN guard layer luminescence for the integration. Hence, for consistency, the integrated intensity for the whole spectra for all samples is considered, which includes the GaN guard layer luminescence. Except for the sample with 1-nm-thick AlN, the samples within the QCSE regime exhibit an increasing integrated intensity with decreasing barrier thickness, as it would be expected due to the smaller built-in electric field strengths and therefore higher excitonic oscillator strengths. However, this 1-nm-thick barrier sample shows the highest absolute intensity (see Figure 6.1) in the QCSE regime. In the confinement regime, the integrated intensity drops with decreasing ND thickness as it is also observed for the absolute intensity (see Figure 6.1), which is justified by the decreasing excitation volume of the 40 NDs in each NW. By weighting the confinement regime samples with the thicknesses of their NDs, the samples exhibit identic integrated intensities, shown in Figure 6.17. Please note, that several months lay between the production of the two series of samples, hence, both series where not measured with identically adjusted measurement setups. Therefore, this weighting method does not perfectly fit to the sample with 4-nm-thick NDs too.

In the raw data for the 2-nm and 3-nm-thick confinement regime samples, a deviation from the linear trend for the high excitation range (125-500 µW) was visible. This is a pure measurement artefact produced by the detecting CCD. At very short integration times (<0.1 s), the CCD exhibits in fact a longer effective integration time, which is not correctly displayed by the setup any more. This has been corrected during the normalization of the intensities in regard to the individual integration times of the recorded spectra.

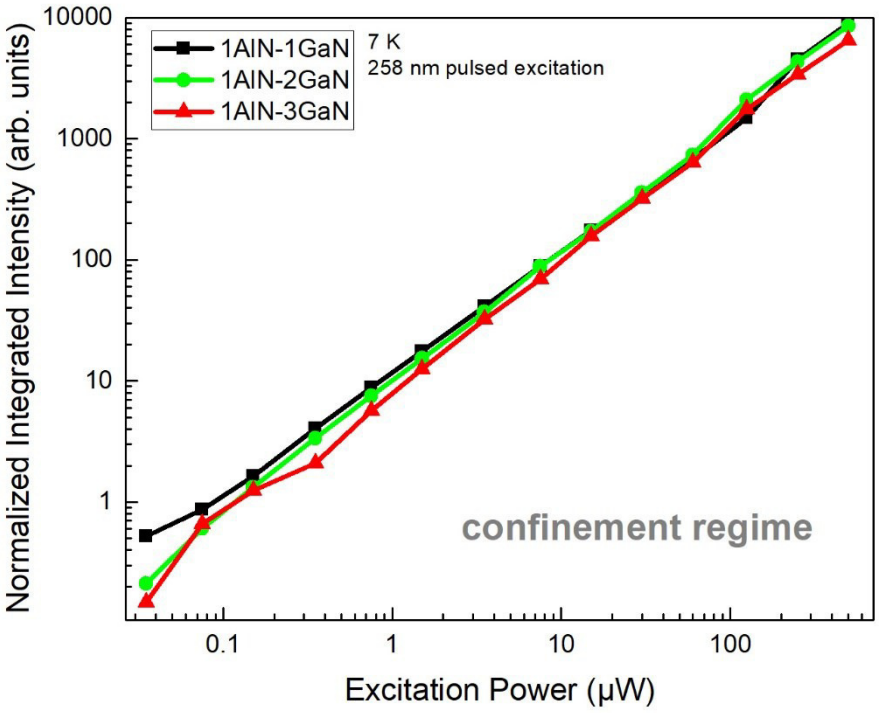

Figure 6.17: Integrated intensity vs. excitation power for the confinement regime samples. The integrated intensity is weighted by the ND thicknesses.

In Refs. [110], [111] the integrated intensity dependence on the excitation powers had been used to evaluate, weather radiative or non-radiative recombinations dominate the electron-hole annihilation process. For this purpose, the proportionality of the integrated intensity I to the injected carrier density J with a power index F can be used $I \sim J^F$. And under the assumption of a fixed spot size for the laser excitation, the injected carrier density J is directly proportional to the excitation power P~J, leading to: $I \sim P^F$. Hence, F depicts the nature of the involved recombination processes and enables a differentiation whether the recombination process is dominated by radiative recombinations for F=1 or non-radiative, Shockley–Read–Hall recombinations for F>1 [110], [111].

The index F was linearly fitted for all intensity trends in the double log plot of Figure 6.16. The determined values for the exponent F are listed in Table 6.2.

Table 6.2: F for all samples.

thickness AlN (nm)-GaN (nm)	F
1-1	1.022 ± 0.014
1-2	1.091 ± 0.008
1-3	1.091 ± 0.015
1-4	1.089 ± 0.012
2-4	1.035 ± 0.007
4-4	0.991 ± 0.004
6-4	1.016 ± 0.003

The values for F are almost equal 1. This result shows that the radiative recombination dominates at 7 K [110].

6.1.4 Temperature dependent photoluminescence

Temperature dependent PL measurements were carried out to investigate the energy, intensity and FWHM as a function of temperature. Such investigations are suitable to identify the influence of localized states originating from excitons bound to ML fluctuations, surface states or defects. Whether such bound exciton states form non-radiative defect centers is indicated by the temperatures at which thermal quenching appears [112], [113].

Figure 6.18 illustrates the temperature dependent PL spectra from 5 K up to 300 K for all samples within the confinement regime. Although being placed below one of the GaN guard layers, the ND luminescence dominates the spectra in all samples up to room temperature. The GaN guard layer luminescence is only weakly visible except for the sample with 1-nm-thick NDs as the excitable ND volume is much smaller. Nevertheless, at room temperature all samples show a ND luminescence with the most pronounced for the sample with the thinnest 1-nm-thick NDs.

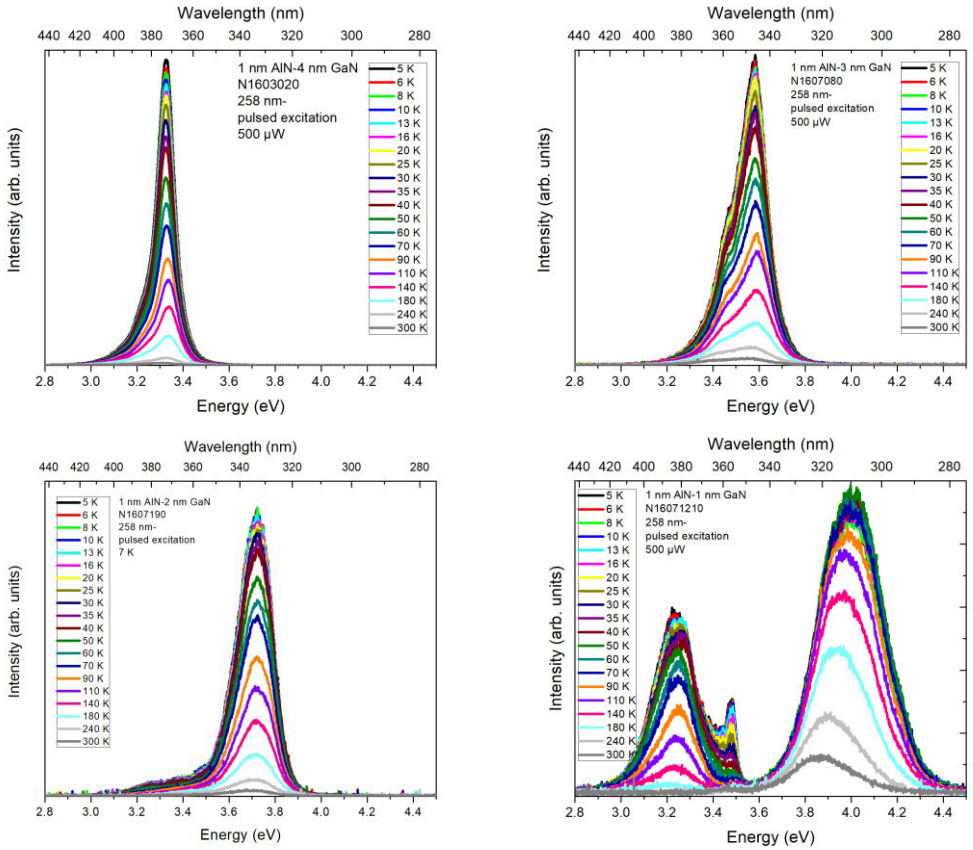

Figure 6.18: Temperature dependent PL for the confinement regime samples and the 4-nm-thick GaN NDs sample with 1-nm-thick AlN barriers of the QCSE regime.

Besides the GaN ND and GaN guard layer luminescence, an additionally peak at 3.2 eV in the 1-nm-thick NDs arises. The origin of this peak could not be finally clarified. In Ref. [65] such a luminescence was assigned to structural defects resulting from the fusion of some NWs and in Ref. [114] it was called a sub-bandgap emission without any further explanations. Noticeable is, that this pronounced luminescence is quite stable with temperature up to 180 K, which is untypical for a defect luminescence. Furthermore, this emission band was not visible in the previously shown power dependent measurements (see Figure 6.13), illustrating that this emission strongly depends on the excited position on the sample. As this luminescence does not appear in each spectrum, the origin is not discussed any further.

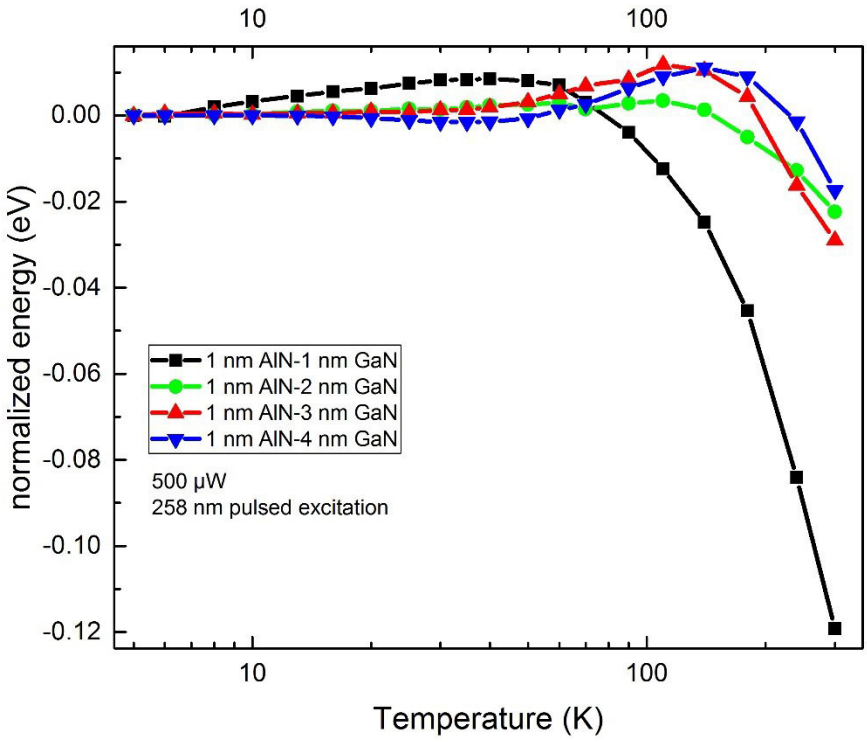

Figure 6.19: Emission energy peak shift with temperature for the confinement regime samples and the 4-nm-thick GaN NDs with 1-nm-thick AlN barriers of the QCSE regime.

Figure 6.19 exhibits the energy shift as a function of temperature for all confinement regime samples. For clarification, the energy shift values at 5 K had been set to 0. In this illustration, different behaviors of the emission energy-temperature trends become obvious. A more detailed presentation is given in Figure 6.20 with the energy vs. temperature accompanied by the FWHM. Furthermore, a fit in regard to the Varshni equation is shown and the characteristic temperature T_c is marked. The Varshni equation describes the energy shift with temperature and T_c the temperature at which the emitted energy follows its Varshni dependency. Hence, above the characteristic temperature T_c the carriers are delocalized [115]. Consequently, T_c can be used to estimate the overall localization depth by k_B*T_c (k_B is the Boltzmann constant). All relevant values, extracted from the fits within Figure 6.20, are listed in Table 6.3.

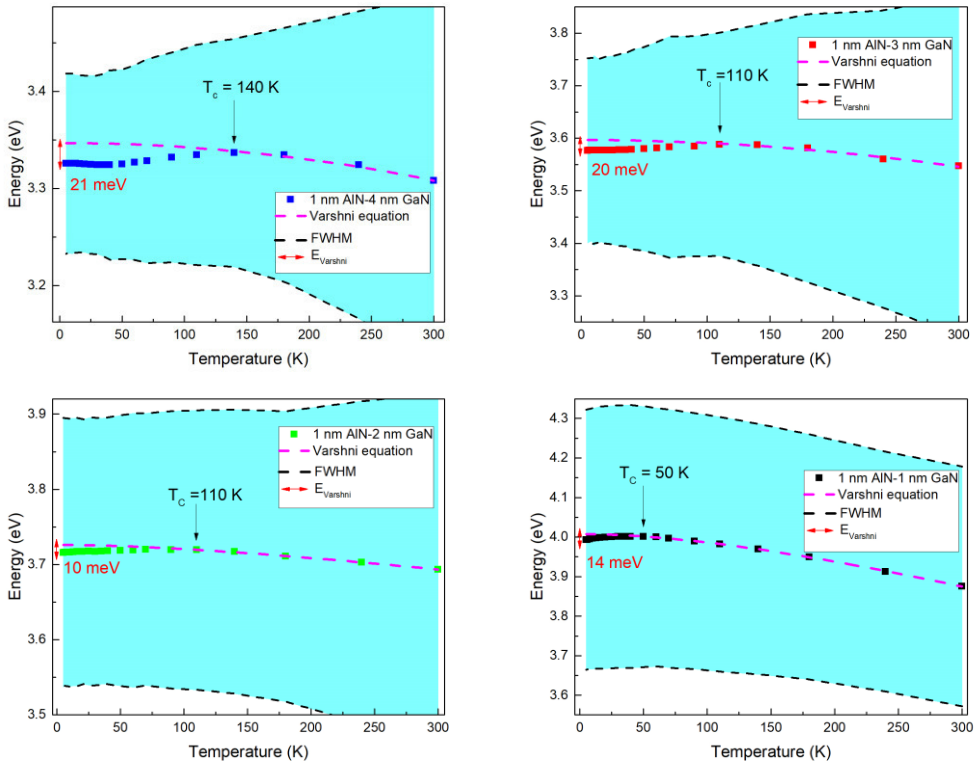

Figure 6.20: Illustration of the emission energy vs. temperature (squares) accompanied by the FWHM (blue tube) and the Varshni shift fit (pink, dashed line) for the confinement regime samples and the 4-nm-thick GaN NDs with 1-nm-thick AlN barriers representative for the QCSE regime. Furthermore, the absolute offsets at the ordinate between the extended Varshni shift fits and the experimental values are depicted in red.

The 4-nm-thick NDs sample is the only one, showing a distinct “s-shape” (decrease-increase-decrease of the emission energies with increasing temperatures [112], [113], [116]–[118]) in Figure 6.20. This s-shaped behavior is a specific characteristic of localized states [112], [113], [116]–[118] – here, surfaces states and QD-like ML fluctuations. The decrease in the emission energy of 1.5 meV in the temperature range between 5-35 K is caused by thermally excited excitons, which are than able to overcome small potential barriers and get trapped by nearby lower localized states. The further enhancement of the thermal excitation provokes an increase of the emission energy by 13 meV up to 140 K. This increase is due to the excitation of excitons from the lower localized states into the higher ND states. The afterwards decrease of about 29 meV up to 300 K is than induced by the temperature dependency of the bandgap [116] (Varshni shift). The samples within the confinement regime do not show such an s-shape (they don't show a decrease in the energy ones the temperature increases). They form a kind of plateau, which is most

pronounced for the 3-nm-thick NDs sample, gets smaller for the 2-nm-thick NDs and completely disappears for the 1-nm-thick NDs. T_c shifts to lower temperatures for smaller ND thicknesses, while the offsets at the ordinate to the fitted Varshni equation become smaller too. However, a differentiation between the localization depths of different types of localized states – surface states, defects, and QD-like ML fluctuations – is not possible. This approximation leads to localization depths of 12, 10, 10 and 4 meV for the investigated 4, 3, 2 and 1-nm thick NDs, respectively. Although localized states influence the optical properties, such small localization depths do not significantly affect the optical properties at room temperature. Additionally, the total energy shift with temperature gets seven times larger for the thinnest NDs (1 nm: 120 meV, 2 nm: 22 meV, 3 nm: 29 meV, 4 nm: 17 meV). This is associated with a decrease of the localization depth of localized states as the Varshni shift starts earlier, at lower temperatures [119].

The FWHM of each sample increases with temperature, except for the 1-nm-thick NDs exhibiting a slight decrease (30 meV). The changes in the FWHM for each sample are marked as a blue band around the emission peak energy values in Figure 6.20. For the 4-nm-thick NDs, the FWHM is relatively small starting with 93 meV expanding to 180 meV. The 3-nm-thick NDs show a FWHM change of 176 meV to 324 meV, whereas the FWHM of the 2-nm-thick NDs increases from 179 meV up to 234 meV, but the 1-nm-thick NDs have a comparably large FWHM of 334 meV at 5 K that decreases down to 305 meV. The comparatively large FWHM difference between 5 K and 300 K of 150 meV for the 3-nm-thick NDs compared to the small FWHM variations of 65 meV and 55 meV for the 4-nm- and 2-nm-thick NDs is an artefact due to the strong GaN guard layer luminescence being energetically close to the investigated ND luminescence (compare Figure 6.18) showing a different temperature behavior with a higher energy shift between 5 K and 300 K (29 meV for ND and approximately 86 meV for GaN). However, the 1-nm-thick-NDs sample is the only sample showing a decrease in the FWHM of 30 meV within the temperature range from 5 K to 300 K.

Table 6.3: Different values obtained from the temperature dependent PL for all samples comprising 1nm-thick AlN barriers.

GaN ND (nm)	4	3	2	1
T_C (K)	140	110	110	50
difference between data and Varshni equation (meV)	21	20	10	14
total energy shift (5 K-300 K) (meV)	17	29	22	118
FWHM (5 K-300 K) (meV)	93-180	176-324	179-234	334-305

The observation of a pronounced s-shape as well as the increasing FWHM from low to high temperatures are characteristic for so called energetically deep fluctuations in the band structure potential landscape. Such potential fluctuations might be attributed to ND thickness fluctuations, alloy fluctuations and/or the presence of an electric field [113], [115]. Among the four samples, only the 1-nm-AlN-4-nm-GaN NDs are expected to comprise a residual electric field; for the confinement regime samples only ML fluctuations and surface states can cause potential fluctuations. Hence, the absence of an s-shaped emission peak shifting for the confinement regime samples indicates, that the s-shape dependency of the emission peak energies with raising temperatures is caused by built-in electric fields. Furthermore, the decrease of T_c down to 50 K for the 1-nm-thick NDs shows the strong decrease of the localization depth for thinner NDs.

6.1.4.1 Integrated intensity dependent on temperature

The investigation of the integrated intensity as a function of temperature allows to analyze, whether the IFGARD samples within the confinement regime show a stability improved behavior at elevated temperatures compared to the samples containing a residual electric field within the QCSE regime. This would automatically mean, that the ideal IFGARD is also less affected by non-radiative recombination centers than conventional, polar quantum well structures.

Figure 6.21 illustrates the absolute integrated intensities over temperature for 4-, 3-, 2- and 1-nm-thick NDs with an AlN barrier thickness of 1 nm. Please note, that the

integrated intensity at low temperatures decreases with a decreasing ND thickness due to the decreasing excitation volume of the thinner NDs, as discussed in the context of Figure 6.1 and Figure 6.17, and, that these measurements had been performed (in contrast to the power dependent integrated intensity measurements) within one run, hence a ND thickness normalization of the graph with a logarithmic scaling is presented in Figure 6.21 b).

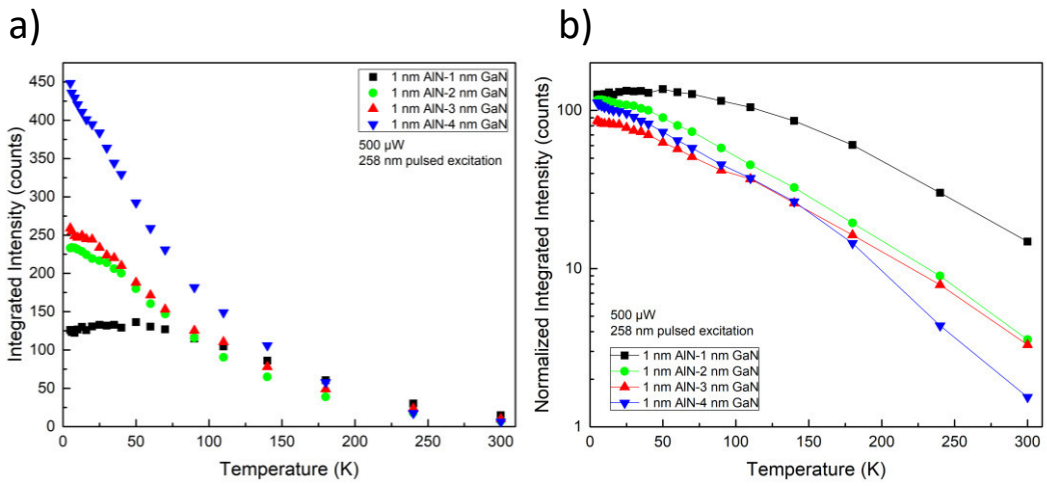

Figure 6.21: Integrated intensity as a function of temperature for all samples comprising 1-nm-thick AlN barriers. The decreased excitation volume of thinner NDs is accounted for in the right plot with a logarithmic intensity scaling.

In Figure 6.21 left, for the 4-nm-thick NDs, the integrated intensity strictly decreases very fast with increasing temperatures. For the 3nm-thick NDs, the total reduction of the integrated intensity over temperature is less pronounced while, in the case of the 2-nm-thick NDs a plateau is formed up to the 10 K mark. However, the 1nm-thick NDs feature a completely different trend of their intensity with raised temperatures. The intensity increases up to a temperature of around 50 K before the intensity starts to decrease. In Figure 6.21 right, the normalization to the ND thickness (excited volume) illustrates the increased luminescence efficiency of the thinner NDs with raised temperatures.

Another illustration of the integrated intensity as a function of temperature is given in Figure 6.22. Here, the intensity is normalized to the maximum for each sample in order to compare the relative intensity variations with raised temperature. The thinnest 1-nm-thick NDs feature a considerably improved intensity stability as, e.g., the green lines (marking a 50 % intensity drop) intersect the samples curve at

approximately 168 K. In comparison, the QCSE regime sample (1 nm AlN-4 nm GaN, having an already strongly reduced electric field) exhibit the 50 % drop at 72 K only. The drastically improved temperature stability again demonstrates the absence of residual electric fields within the IFGARD samples in the confinement regime. Nevertheless, the thermal quenching of the integrated intensity is attributed to phonon-assisted non-radiative recombination centers with decreased influence on the 1-nm-thick ND IFGARD sample [120].

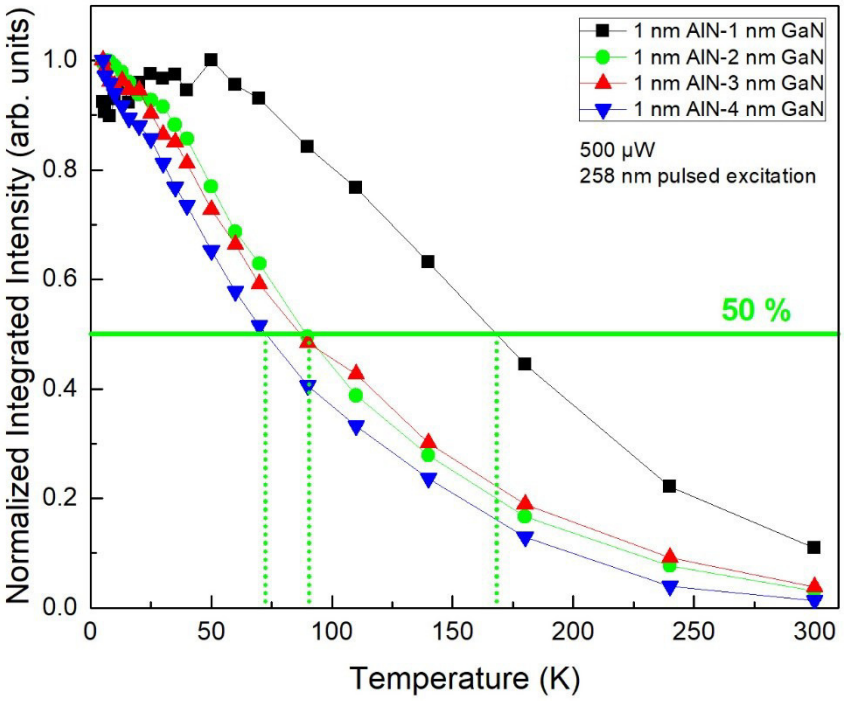

Figure 6.22: Integrated Intensity normalized to the individual maximum values as a function of Temperature for all samples with 1-nm-thick AlN barriers. An intensity drop to 50 % is marked by the green line.

6.2 Time-resolved photoluminescence

This chapter deals with the decay behavior of excitonic complexes in IFGARD NDs, which is investigated by means of time resolved photoluminescence (TRPL) studies.

First, temperature dependent TRPL measurements of the 1-nm-thick ND sample are discussed in chapter 6.2.1 in order to proof if even the exciton decay times are as well of high temperature stability like the integrated intensity in chapter 6.1.4. As this

investigation finds multiple time constants, the multiexponential decay transients are determined at energetic positions spread along ND luminescence peaks of several samples in the second chapter 6.2.2. Here, for the first time within III-Nitride QWs/NDs, a triexponential decay is found in the confinement regime samples, which is caused by the absence of built-in electric fields. An explanation of the found triexponential decay in the samples is suggested in chapter 6.2.3. The last chapter 6.2.4 directly compares the decay transients of all samples with each other.

6.2.1 Temperature dependent time-resolved photoluminescence

Chapter 6.1.4 showed an improved temperature stability for the integrated intensity of the 1-nm-thick GaN NDs compared to the thicker 2-, 3- and 4-nm thick GaN NDs (Figure 6.22). This chapter (6.2.1) investigates whether this increased temperature stability mirrors a stable decay time over temperature for the 1-nm-thick GaN NDs.

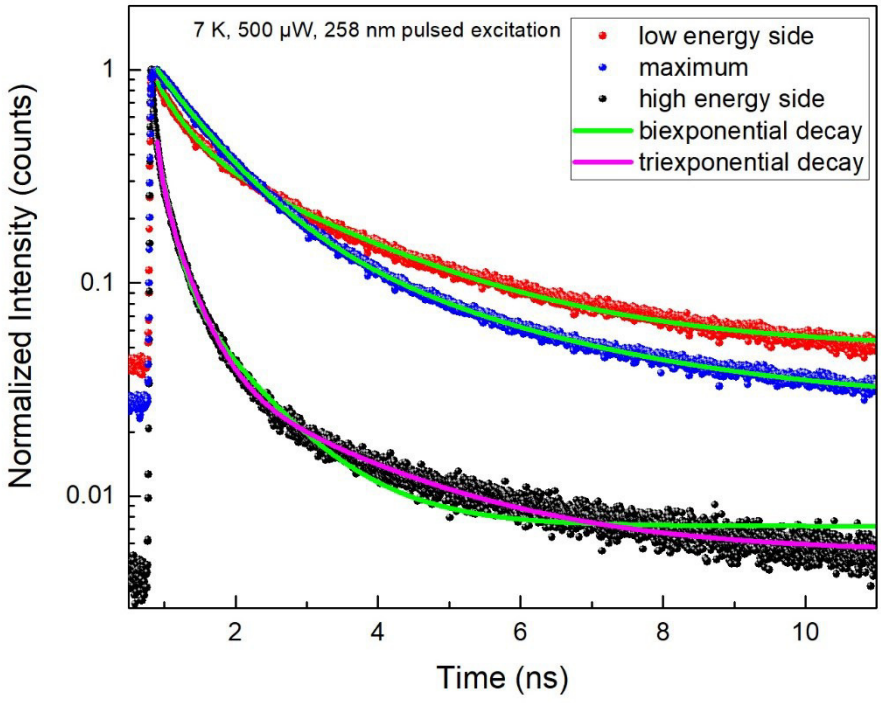

Figure 6.23: Comparison between the decay transients taken at the maximum (blue), the low (red) and high (black) energy side of the 1-nm-thick NDs luminescence peak. While the low energy side follows a biexponential decay process (green fits), the high energy side needs to be described by a triexponential decay process (purple fit).

Figure 6.23 compares the decay transients of the low energy flank (red), the maximum (blue) and the high energy flank (black) of the 1-nm-thick NDs' luminescence peak. The high and low energy flank transients were recorded at the FWHM. While the transients at the low-energy side and at the maximum fit well to biexponential decays (green fits), the high-energy side reveals a triexponential decay (purple fit). The additional third decay component occurs above an emission energy of 4.1 eV as will be shown in chapter 6.2.2, Figure 6.26.

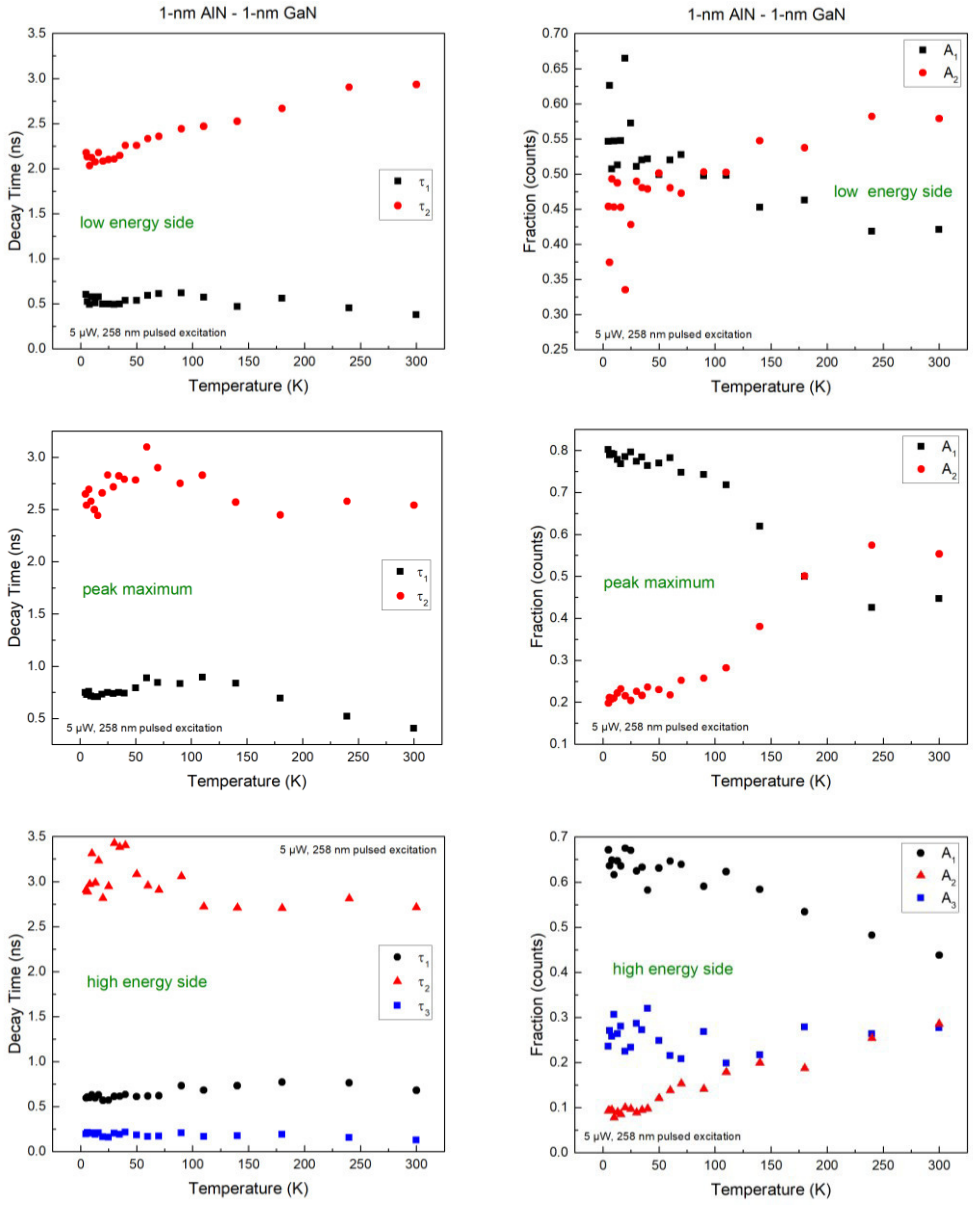

Figure 6.24: Decay times τ_1, τ_2, and τ_3 as well as photon count fractions as a function of temperature for the 1-nm thick NDs with 1-nm thick AlN barriers at the low energy side (top), at the luminescence peak maximum (center), and at the high energy side (bottom).

Figure 6.24 illustrates the decay times at the low energy side of the luminescence peak, at the maximum, and at the high energy side recorded with a constant excitation power of 5 µW for a varying temperature between 5 K and 300 K. Except for the peak maximum, the data were recorded at the energetic positions of the FWHM. In Figure 6.24, different trends of the decay times are visible, whereas when considering the different fractions of the decay times (Figure 6.24 right), the mean tendency of the fraction trends does not change for the different energetic positions. For a direct comparison of each decay time depending on energetic position and temperature in the 1-nm AlN – 1-nm GaN ND sample, see Figure 6.25.

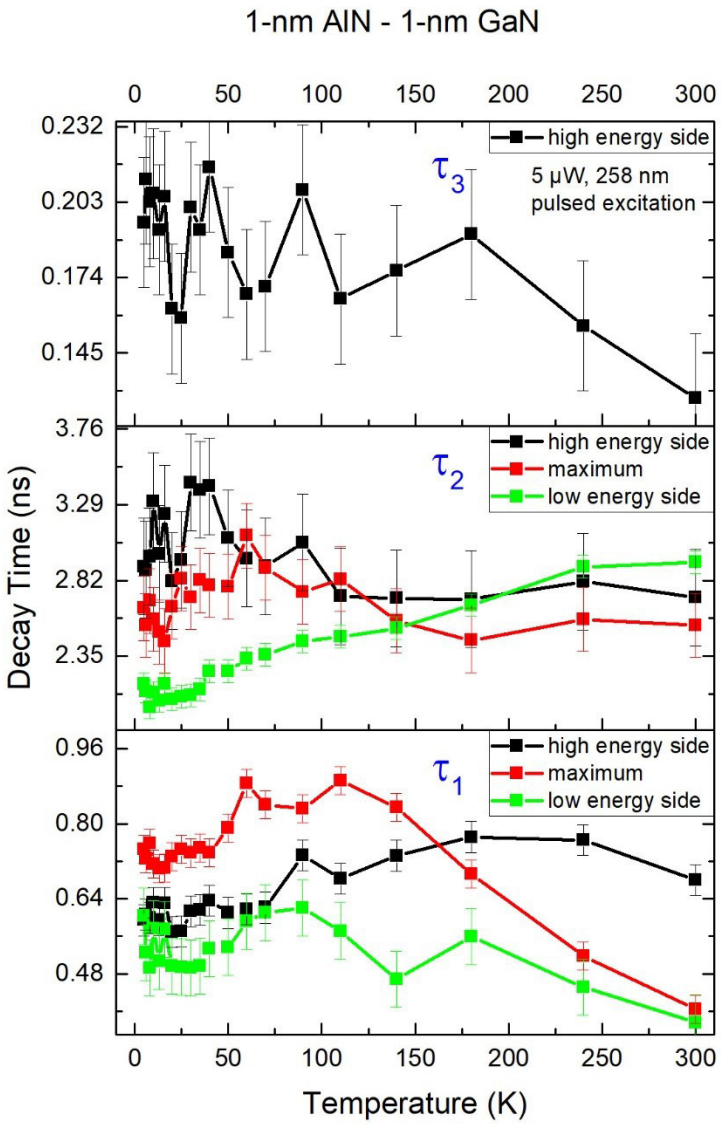

Figure 6.25: Direct comparison of the decay times τ_1, τ_2, and τ_3 as a function of temperature depending on the different 1-nm-thick ND luminescence positions (low energy side-green, maximum-red, and high energy side-black). As illustrated in Figure 6.23, τ_3 only appears on the high energy side. τ_1 and τ_2 are present at all positions showing different trends.

At the ***low energy side (green),*** two decay times are observable (see Figure 6.23 and Figure 6.24). τ_2 shows an increase with increasing temperature from 2.2 ns to 2.9 ns. An increase of decay times with increasing temperature is a typical behavior for radiative recombination centers [120] while for non-radiative centers a decrease of the decay time with temperature would be expected [121]. The decay time τ_1 is almost constant at 0.5 ns $\pm$0.1 ns over the whole temperature range. A small jitter of the decay time over temperature is assigned to the accuracy of the data.

At the peak ***maximum*** of the emission (red), τ_2 is (with 2.5 ns) slower than at the low energy side (with 2 ns). After a small enhancement of 0.5 ns up to 60 K, the decay time decreases by 0.5 ns followed by an approximatively constant decay time of 2.5 ns above 100 K.

τ_1 at the maximum is 0.2 ns slower (0.7 ns$\pm$0.1 ns) compared to the low energy side (0.5 ns$\pm$0.1 ns) and shows a further increase by 0.2 ns (0.9 ns$\pm$0.1 ns) with temperatures up to 110 K. Above 110 K, τ_1 starts to decrease down to 0.4 ns.

As the decay time τ_1 gets very small with 0.4 ns for 300 K and the fraction (Figure 6.24) of this decay time decreases with temperature leading to the assumption of increasing non-radiative decay rates. However, such a considerable decrease in the decay time is not observable for τ_2 indicating that almost all of the luminescence at room temperature (chapter 6.1.4) can be assigned to ND excitons provoking τ_2.

The observable behavior of τ_2 at the ***high energy side*** is similar to that at the emission peak maximum, except that the decay time starts with a slower decay time of 2.9 ns and ends with 2.75 ns. The slowdown of the low temperature τ_2 at the three energy positions might look like energetically higher ND exciton states become continuously more involved, however, a finer energetic resolution (presented in the following chapter 6.2.2) evidences a more complex behavior of the low temperature time constants.

Remarkably, at the high energy side of the luminescence peak, τ_1 increases up to a temperature of approximately 170 K in contrast to τ_1 at the luminescence peak maximum.

τ_3 stays almost constant at 0.18 ns over the whole temperature range indicating a recombination combined with fast relaxation processes independent on

temperature. This assumption of an involved relaxation process is supported by the circumstance, that τ_3 contributed only 25 % of the photon counts to Figure 6.24 although it is three times faster than τ_1, which contributed 65 % of the photon counts.

Independent of the energetic position, the trends of the photon-count fractions of each decay time do not change (Figure 6.24). The fast decay time τ_1 has a larger fraction compared to the slower τ_2 time (same trend as in Figure 6.26). With increasing temperatures τ_1 loses photon counts in favor of τ_2. This shows, that τ_1 related, radiative exciton recombinations are not as temperature stable as the τ_2 related indicating that excitons with lifetime τ_1 can be thermally delocalized, probably into energetically higher states provoking τ_2.

Very interesting is the comparison to Ref. [112], where the authors investigate the radiative and non-radiative contributions to decay times belonging to decay processes of QW and QD states. They show a constant behavior of the decay time for the QD states, as it is visible for τ_1 on the low energy side in the here investigated samples. Additionally, they differentiated the radiative and non-radiative contributions under the assumption that the non-radiative contributions increase with temperature. Due to their approach, the authors expect a linear increase of the decay time with temperature for the radiative recombination time of QW states. Exactly the same trend is observable for τ_2 (probably being ND exciton states) in the here investigated samples on the low energy side. For the high energy side, the investigated sample shows a triexponential decay, which prevents a comparison to Ref. [112]. In Summary, τ_1 and the slower decay time τ_2 can be assigned to radiative QD/surface states and ND states, respectively. With the wording introduced in chapter 6.1, the multiexponential decay transients probably originate from excitons in ND states, normal ML fluctuations, and surface states and QD-like ML fluctuations.

Coming back to the initial question, the decay times for the 1-nm-thick GaN NDs show a high temperature stability as expected due to the high temperature stability of the integrated intensity in chapter 6.1.4. While the following chapter primarily investigates the distribution of the decay times along the ensemble luminescence

with higher energetic resolution it also investigates, whether the same complex multiexponential decay behavior can be found in the other samples.

6.2.2 Decay times as a function of the emitted ND luminescence

Investigating the TRPL transients at different emission energies within the broadness of the ND luminescence can assure the identification (given in chapter 6.2.1) of the different excitonic complexes that create the multiexponentiality of the recorded transients. Besides, multiexponentiality of transients as well as changing decay rates for different energetic positions within broad QW luminescence is commonly assigned to the influence of built-in electric fields [123]. However, in this thesis, the field-free confinement regime samples allow a field-free investigation of multiexponential decay rates in c-plane GaN/AlN QWs for the first time.

The results are discussed for the confinement and the QCSE regime samples separately.

6.2.2.1 Confinement regime

Figure 6.26 a) shows the different decay times τ_1, τ_2 and τ_3 for different emission energies along the 1-nm-thick ND luminescence peak recorded with two different excitation powers. The different excitation powers do not significantly influence the decay times, which is contrary to what is found for the QCSE regime samples, presented later in Figure 6.28. Therefore, this excitation power independence is attributed to the absence of a built-in electric field. The third decay time τ_3 may be attributed to the recombination of excitons in ND states that additionally relax into surface states and QD-like ML fluctuations assigned to τ_1 (see Figure 6.29). The relaxation process from these τ_3-related ND excitons affects τ_1 by re-filling of the attributed states. In Figure 6.26 b), the behavior of the contributing photon-counts fraction of each decay time as a function of the emission energy is plotted. As expected, the fast decay time τ_1 has a larger fraction compared to the slow decay time τ_2. Above 4.1 eV, where the third decay time τ_3 gets detectable, the fraction of τ_1 decreases abruptly, whereas the fraction of τ_2 starts to smoothly decrease earlier, independent of the appearance of τ_3. Another possibility to show the interaction

between τ_1 and τ_3 is exhibited in Figure 6.26 c) and d) with τ_3 being subtracted from τ_1 and A_3 is summed to A_1 producing continuous trends. This representation nicely illustrates that the third decay time τ_3 includes a relaxation process from ND states into surface states and QD-like ML fluctuations.

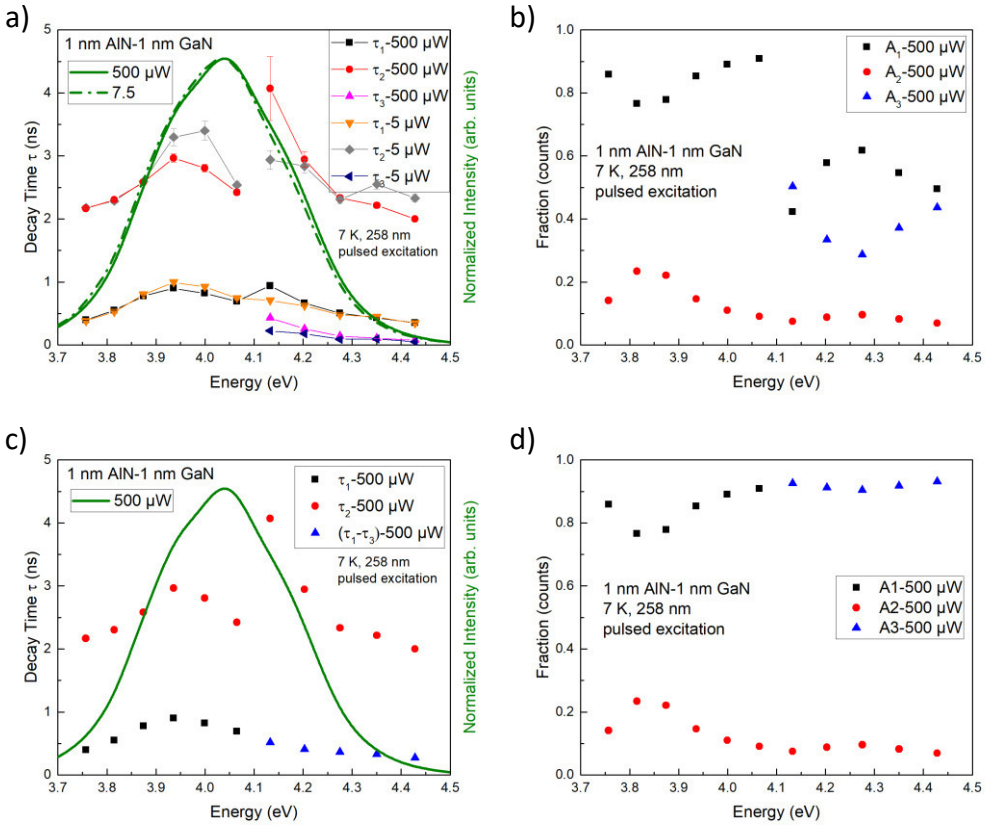

Figure 6.26: a) Evolution of the decay times τ_1, τ_2, and τ_3 along the 1-nm-thick NDs' luminescence (green) for low and high excitation powers. b) Fractions of the total counts A_1, A_2 and A_3 for the decay times τ_1, τ_2, and τ_3, respectively. c) and d) show in principle the same as a) and b) with the difference, that τ_3 is subtracted from τ_1 and A_3 is summed to A_1 to demonstrate a refilling by τ_3.

The assignment of τ_2 to NDs states made in chapter 6.2.1 is supported by comparing the energy dependence of τ_2 for all samples within the confinement regime in Figure 6.27. For the 1-nm-thick NDs (Figure 6.27 top), τ_2 shows an abrupt increase in the decay time above 4.1 eV, which is interpreted as the energy at which the next, 1-ML-thicker ND state band begins. Within each ND state band, the τ_2 gradually decreases, as relaxation from energetically higher excitons in the same ND band to energetically lower states arises. Exactly this characteristic gets less pronounced for the 2-nm-thick NDs and completely disappears for the 3-nm-thick NDs in Figure 6.27. Additionally, the occurrence of the τ_3 time shifts to lower energies relative to the individual ND

luminescence peak maximum. This systematic trend just reflects the decreasing influence of the ML fluctuations on the ND emission energies (Figure 6.11 and Figure 6.12). But this does not mean, that there exists no ML fluctuation anymore, only that this clear separation between two different ND-state bands is not resolvable anymore.

Former publications, like Refs. [112], [122] also reported an additional decay process on the high energy side, changing the transients of QW luminescence from monoexponential to biexponential at the low and the high energy side, respectively. However, a change from a biexponential to a triexponential decay, as presented here, in this investigation, has never been reported for nitride heterostructures before. The absence of the electric field enables tracking of the multiple lifetimes as the decay and relaxation time variations with emission energy are not dominated by the QCSE anymore. That this observation is indeed enabled by the absence of electric fields in contrast to what is possible in conventional nitride heterostructures [112], [122] can be substantiated by comparing the confinement regime samples with the QCSE regime samples in the following chapter 6.2.2.2.

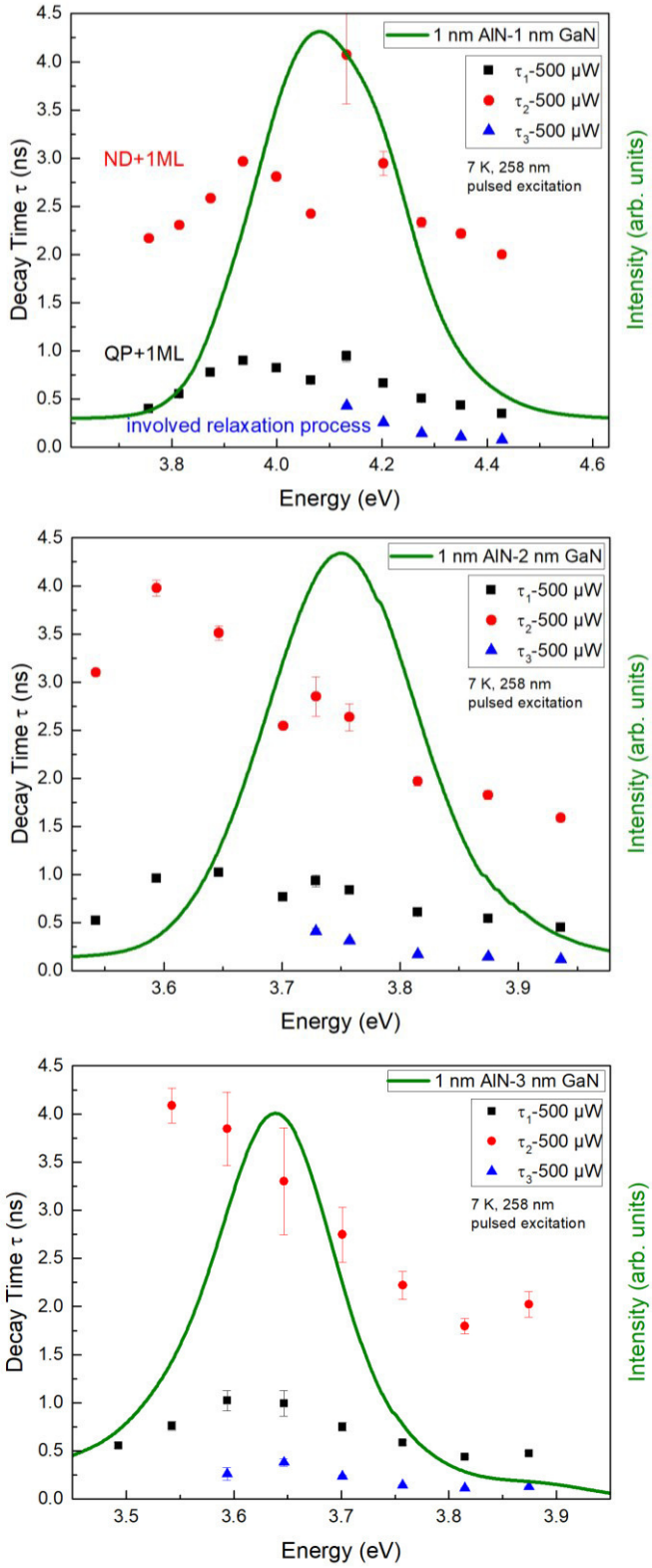

Figure 6.27: Decay times vs. emission energy for the 1-nm-thick NDs, at top, the 2-nm-thick NDs, at center, and the 3-nm-thick NDs, at bottom within the confinement regime. The abrupt increase of τ_2 reduces for the 2-nm-thick NDs and disappears for the 3-nm-thick NDs, while the energetic position of the occurrence of $\tau_3$shifts to lower energies relative to the emission peak maxima demonstrating the decreased influence of the ML fluctuations on the ND luminescence broadness.

6.2.2.2 Quantum-confined Stark effect regime

With the presence of a built-in field (in the QCSE regime samples) the behavior of the decay times becomes different to the one presented in chapter 6.2.2.1 for the confinement regime samples.

In Figure 6.28 a) the decay times τ_1 and τ_2 vs. the emission energy along the broad ND luminescence peak are plotted for low and high excitation powers. The exemplarily shown data belong to the4-nm-thick GaN NDs with 2-nm-thick AlN barriers. Both decay times, τ_1 and τ_2, gradually increase with decreasing emission energy for the high as well as for the low excitation power. Remarkably, the ordering of the data points for high/low excitation powers switches between the high and low energetic flank of the peak as the built-in field screening with high excitation powers seems to be effective for the emission stemming from the lower energy side only [122]. This surprising finding is explained by Figure 6.28 b), where the emission energy shift of the emitting excitonic states caused by the charge carrier screening is artificially removed. Besides, that the built-in field screening effect on the decay times becomes less effective energetically closer to the GaN guard layer luminescence at 3.47 eV is expected.

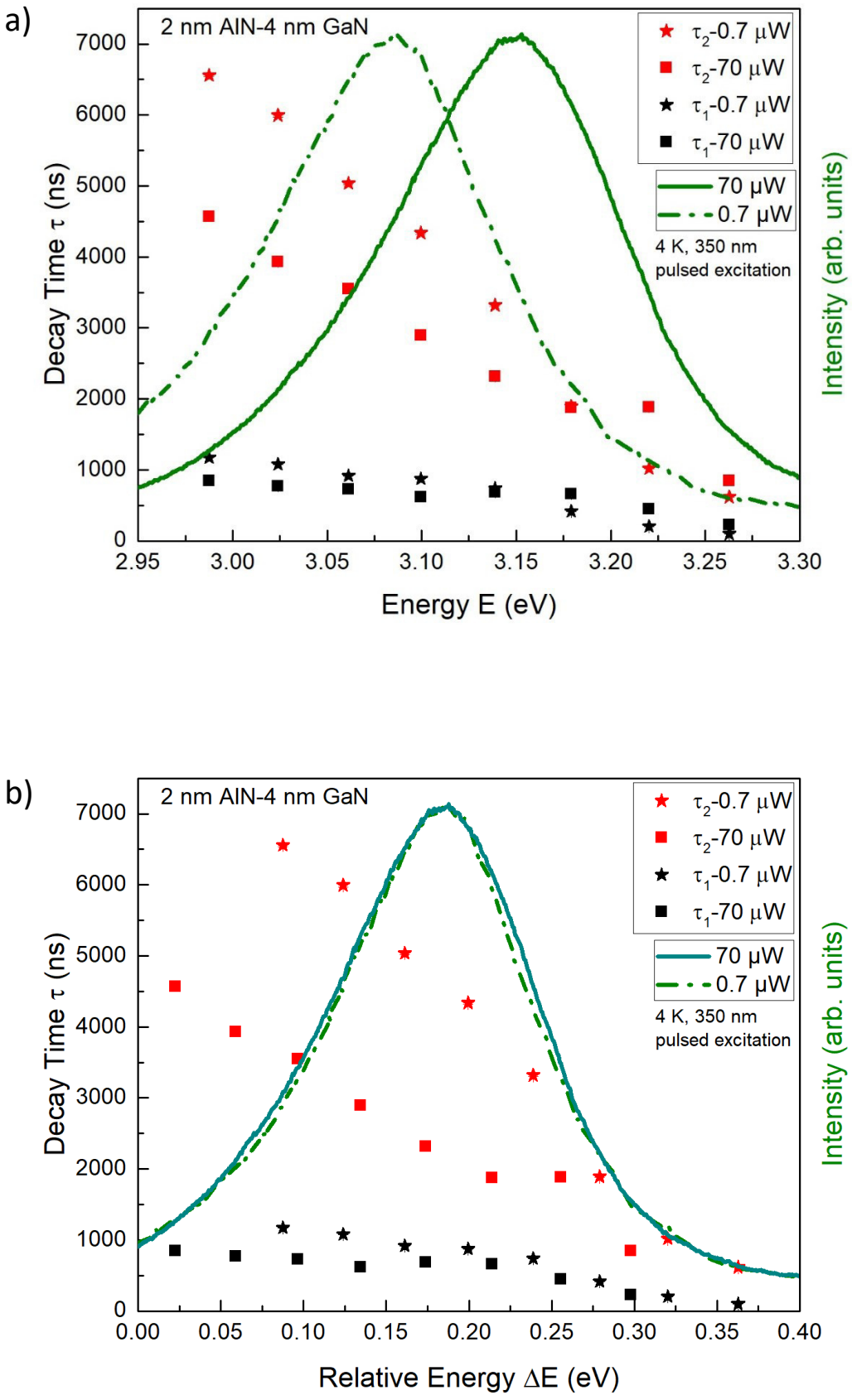

Figure 6.28: Decay time τ_1 (black) and τ_2 (red) along the 2 nm AlN-4 nm GaN NDs luminescence (green spectra) for high (squares) and low (stars) excitation powers, a) and the same data points artificially shifted to compensate the charge carrier screening of the emission energy, b).

The overall increase of the decay times with decreasing emission energy is typically assigned to localized excitons in QWs resulting from alloy fluctuations and monolayer fluctuations of the ND thicknesses [83], [112], [113], [119], [121]–[130]. According to these references, the decay time trend originates from the (at the high energy side) involved non-radiative relaxation processes into the exciton states that emit at the energetically lower side of the peak. However, an additional impact of the ND thickness is expected, as excitons in thicker NDs with QCSE emit at lower energies, but at the same time exhibit a larger electron-hole separation. Another explanation attributes the decay time trends to the pulsed excitation of the TRPL measurements: "at short delay times, the electric field created by the photo injected carriers partially screens the existing piezoelectric field, resulting in an increase in the carrier's wave-function overlap and a blue shift of the transition energy. At longer delay times, as the carriers recombine, the field screening reduces, and the wave-function overlap is reduced and the transition redshifts [122]." However, such a behavior should lead to higher than biexponential decays due to the gradually reducing electron-hole overlap with time. That the decay time trend is related to the built-in fields (either direct or via the QCSE in ML fluctuations) can be investigated in the samples within the confinement regime that do not exhibit a built-in electric field. Here, the confinement regime samples in Figure 6.26 do not show such a continuous decay time decrease, which on the other hand once more indicates the absence of built-in fields in the confinement regime samples.

In InGaN QWs small decay rates are commonly assigned to compositional fluctuations of In and large decay rates to thickness variations of the InGaN layers [120], both being able to localize excitons in three dimensions. Hence, the experimental results for the QCSE regime samples would also follow these commonly used explanations for the InGaN system with two different, localized states. However, the STEM analyses (Figure 6.9 and Figure 6.3) did not show significant alloy fluctuations within the NDs. Thus, the common assignment of the slow lifetime component to excitons localized in alloy fluctuations is not an option for the investigated GaN/AlN NDs. Nevertheless, the QD-like ML fluctuations and surface states are able to localize excitons. However, the confinement regime samples without built-in electric fields

investigated in chapter 6.2.2.1 do not show the same continuous decay rate trends, which facilitates the assignment of the slow decay time to two-dimensional non-localized exciton states of the NDs.

In order to additionally check the assignment of the decay rates to two different localized states the localization depth can be determined by a weak exciton localization model [119]. In this model the decay time behavior vs. emission energy can be fitted by:

$$\tau = \frac{\tau_{rad}}{1+e^{\left(\frac{E-E_m}{E_0}\right)}}. \qquad (6.3)$$

With τ being the decay time, τ_{rad} the radiative decay time, E the emission energy, E_m the energy of the mobility edge and E_0 the exciton localization depth. Excitons occupying energy levels above the mobility edge E_m represent free exciton states of a ND and below the mobility edge localized exciton states [112]. In this model τ_{rad} equals the pure radiative decay time, assumed to be present at the lowest emission energy of the low temperature luminescence peak only [83] (as discussed above, at higher emission energies, non-radiative relaxation processes into energetically lower states are involved). By fitting equation 6.3 to the decay times in Figure 6.29, the activation energy E_0 of each decaying excitonic complex is accessible. The determined activation energy of 46 meV for τ_1 is independent of the excitation power whereas for τ_2 the activation energy strongly depends on the excitation power: being 52 meV for low excitation and 117 meV for high excitation powers. These totally different power dependencies of the activation energies for the two decay times indicate that they have two fundamentally different origins instead of two similar localized states origins. However, the determined activation energies assign τ_1 to excitons localized in potential fluctuations [127], while τ_2 might be related to normal ML fluctuations, as with increasing numbers of excited charge carriers, the polarizing field strengths of the ND excitons is reduced resulting in an increased electron-hole coulomb interaction. In this interpretation, the power dependent activation energy of τ_2 translates into the dissociation energy of the ND excitons (within the normal ML fluctuations) into free electrons and holes. Therefore, τ_1 might be assigned to QD-like ML fluctuations [131] (compare Figure 6.30). As these shallow localization centers are

expected to exhibit only few states, the increased excitation power leads to a delocalization of the excitons from the QD-like ML fluctuations into the ND states before charge carrier screening can significantly alter their delocalization energy. Consequently, the decay time τ_1 does not show different localization energies for high and low excitation power.

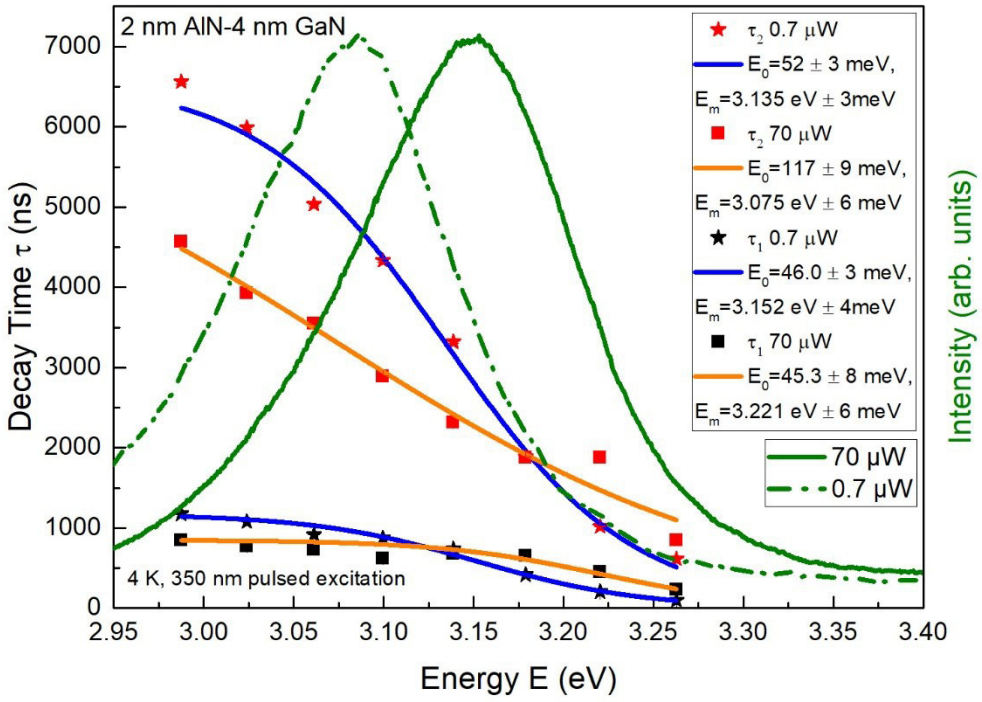

Figure 6.29: Determination of the localization depths within the 4-nm-thick GaN NDs with 2-nm-thick AlN barriers by fitting the decay times τ_1 and τ_2 with a weak exciton localization model [119] *(equation 6.3). The fits were performed on the decay times τ_1 and τ_2 for low and high excitation powers separately, delivering the same localization depth for τ_1 but different depths for τ_2, which shows that the origins of the two recombinations are fundamentally different.*

Finally, the mobility edge E_m for the ND states decreases by approximately the same amount, their dissociation energy increases with higher amounts of built-in field screening charge carriers: As the electron-hole separation is reduced, the electron-hole Coulomb attraction increases, which might cause this abnormal mobility edge reduction. However, the shift of the mobility edge to higher energies for the QD-like monolayer fluctuations follows the total emission energy blue shift in the samples due to the gradual removement of the Stark redshift by the screening charge carriers.

In conclusion, the interpretation given in chapter 6.1 is confirmed: Built-in fields lead to a localization of excitons, which was lifted in the QCSE regime sample for the ND excitons by higher excitation powers screening the built-in field.

6.2.3 Multiexponential decay process

In the previous subchapters multiexponential decay transients in the investigated samples were analyzed. Such multiexponential decay transients originate from multiple recombination pathways of different excitons in a sample emitting within the given energetic window of the TRPL setup. This chapter visualizes the given interpretations of the origin of the decay processes.

In general, Decay transients show a decay in the form of

$$A(t) = \sum_{i=1}^{n} A_i e^{\frac{-t}{\tau_i}} \text{, with n } \epsilon \text{ N.} \tag{6.1}$$

Each summand describes one recombination pathway (e.g., QD-like and ND excitons). However, one pathway can involve several recombination channels

$$e^{\frac{-t}{\tau_i}} = \prod_{k=1}^{m} e^{\frac{-t}{\tau_{i,k}}} \text{, with m } \epsilon \text{ N,} \tag{6.2}$$

like the radiative recombination of a ND exciton besides its relaxation into energetically lower ND states. Hence, τ_i represents the effective lifetime of the excitons of type "i".

In the confinement regime samples, three decay processes are detected. The identified recombination pathways within the NDs are summarized in Figure 6.30. In this figure, the band edge diagram of the 1-nm thick NDs is sketched. Corresponding to the discussed ML fluctuations in the previous chapters (6.1.2.2 and 6.2.2), the normal ML (ND+1ML) and the QD-like ML (QD+1ML) fluctuation is sketched with τ_2 and τ_1, respectively. τ_3 describes the combined recombination and relaxation originating from the primary ND thickness (in this case 1 nm) into the ND+1ML or QD-like ML fluctuations. The gray areas represent the ND states as a quasi-band. Whereas for the ND states more excited states are reachable, for the QD electrons only the ground state is expected due to its flat potential well. For the holes this is expected

to be different due to two effects: first of all, their larger effective mass causes less confinement within QDs that confine electrons well and second, the comparatively small energetic distances between the A and B band edges will probably allow more than one excited hole state within the QDs, if the dimensions of the QD are large enough. The picture distinguishes between the recombination processes on the low energy (a) and high energy (b) side of the ND luminescence peak as well as for higher temperatures (c).

At the ***low energy*** flank of the luminescence peak, τ_2 originates from the recombination of excitons in the normal +1ML fluctuations and τ_1 from the QD-like ML fluctuations. The recombination process of the QD-like ML fluctuations is expected to be faster due to the stronger charge carrier confinement (at least of the electron wave function).

At the ***maximum and high energy*** side, more recombination and relaxation channels have to be considered. As illustrated in Figure 6.30 (b), the charge carriers in the primary ND are able decay radiatively or relax into the normal ML fluctuations and QD-like ML fluctuation. Hence, as visible from equation 6.2: $\frac{1}{\tau_3} = \frac{1}{\tau_{2,ND}} + \frac{1}{\tau_r}$.

Figure 6.30 (c) sketches the decay processes at the low energy side for ***higher temperatures***, in order to explain the temperature dependent results in section 6.2.1. For the +1ML ND states, higher temperatures thermally excite charge carriers into energetically higher states within the +1ML ND states band, leading to a continuous increase of τ_2 with temperature [Figure 6.24 a)].

For the charge carriers in the QD-like +1ML fluctuations, no free, energetically higher states within reach exist. Hence, τ_1 on the low energy side is independent from temperature [Figure 6.24 a)].

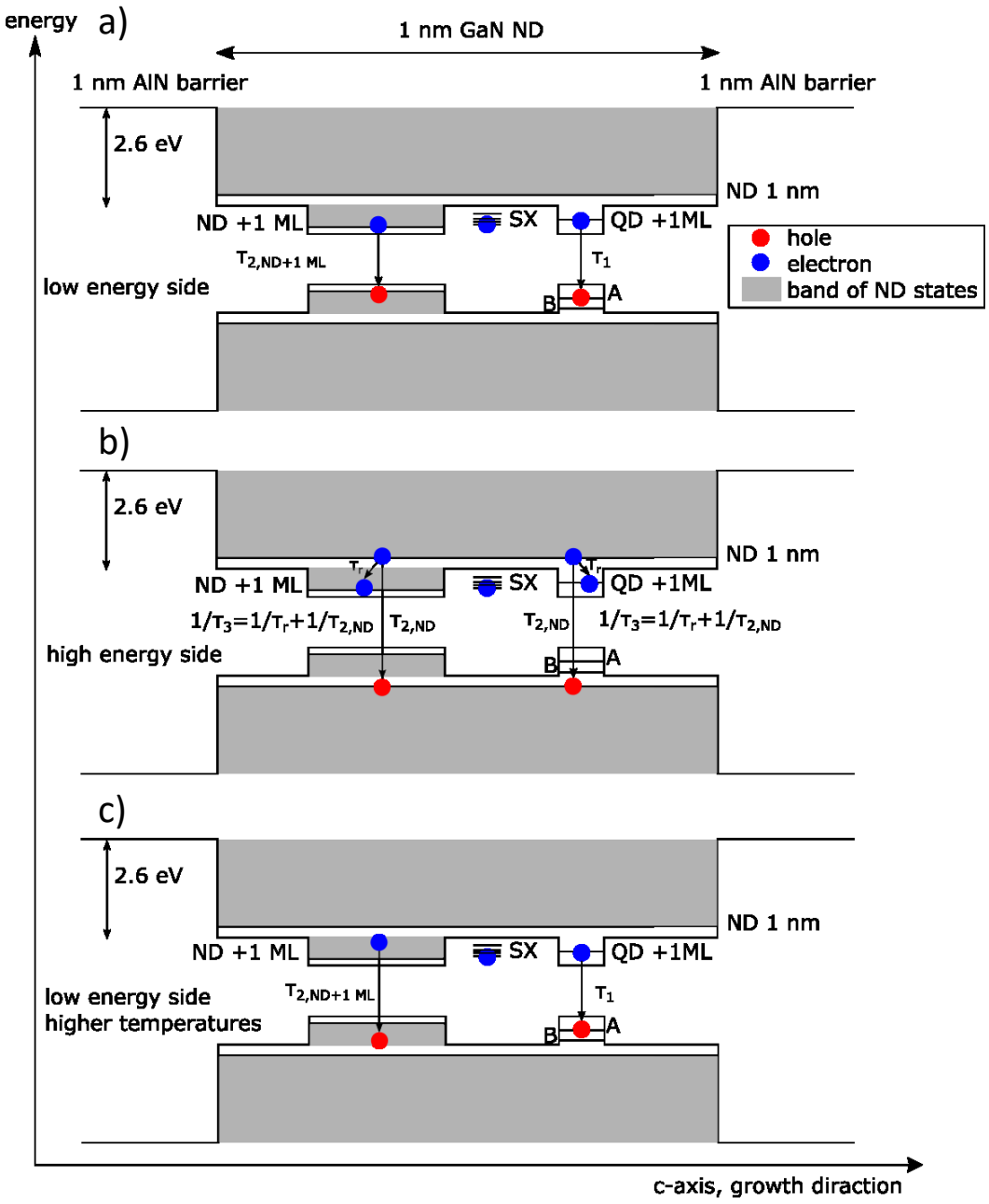

Figure 6.30: Different recombination pathways in a 1-nm-thick ND for the low a) and high b) energy sides of the ND luminescence peak as well as for the low energy side at higher temperatures c). The ND state bands (gray) and the QD-like single electron state together with QD-like multiple hole states due to the energetically close A, B valance bands in combination with the small effective hole mass. While at the low energy side two recombination processes, τ_1 and τ_2 originating from the normal and QD-like ML fluctuations are detectable, on the high energy side three recombination processes are determined. At the high energy side, a combined recombination and relaxation process τ_r from the primary ND into ML fluctuations and QD-like fluctuations is assumed leading to τ_3. T Charge carriers in the normal ML fluctuations on the energetically lower side can be thermally excited fluctuate, which is not possible for charge carriers in QD-like ML fluctuation as no free states exist.

6.2.4 Fundamental differences in the transients for the quantum-confined Stark effect- and confinement regime [45]

The previous chapters identified the origin of multiexponential decay transients in the investigated samples and determined fundamental differences in the decay behavior for the QCSE and confinement regime samples series. Finally, this chapter directly compares the recorded decay transients of all samples taken just at the luminescence maxima in order to demonstrate the immense, global influence of the built-in electric field strengths on the overall decay characteristics of excitons in the NDs.

Figure 6.31 a) shows the decay transients of the samples within the QCSE regime and Figure 6.31 b) of those within the confinement regime. The legends of Figure 6.31 comprise the results of the biexponential decay fits at the luminescence peak maxima (equation 6.1). Bold letters highlight the dominant decay time, which corresponds to the decay time with significantly more counts. The biexponentiality originates from surface states and QD-like ML fluctuations besides the normal ND states as explained in detail in the previous chapters.

Regardless of the nature of the emitting excitons and the involved recombination paths, for the samples within the QCSE regime, the shorter excitonic lifetimes decrease for decreasing AlN-barrier thicknesses from 7.34 µs down to 40 ns by more than 2 orders of magnitude in accordance with the built-in field reduction determined in chapter 6.1.1. Hönig et al. [40] predicted the same amount of increase in the electron-hole oscillator strength within IFGARD GaN/AlN quantum dots. If the ND thickness is afterwards decreased from 4 nm to 3 nm (constant AlN barrier thickness of 1 nm), the decay time drops further down to approximately 0.7 ns and stays constant for all three confinement regime samples when changing the ND thickness further down to 2 nm and 1 nm; as all confinement regime samples feature very similar transients in Figure 6.31 (b).

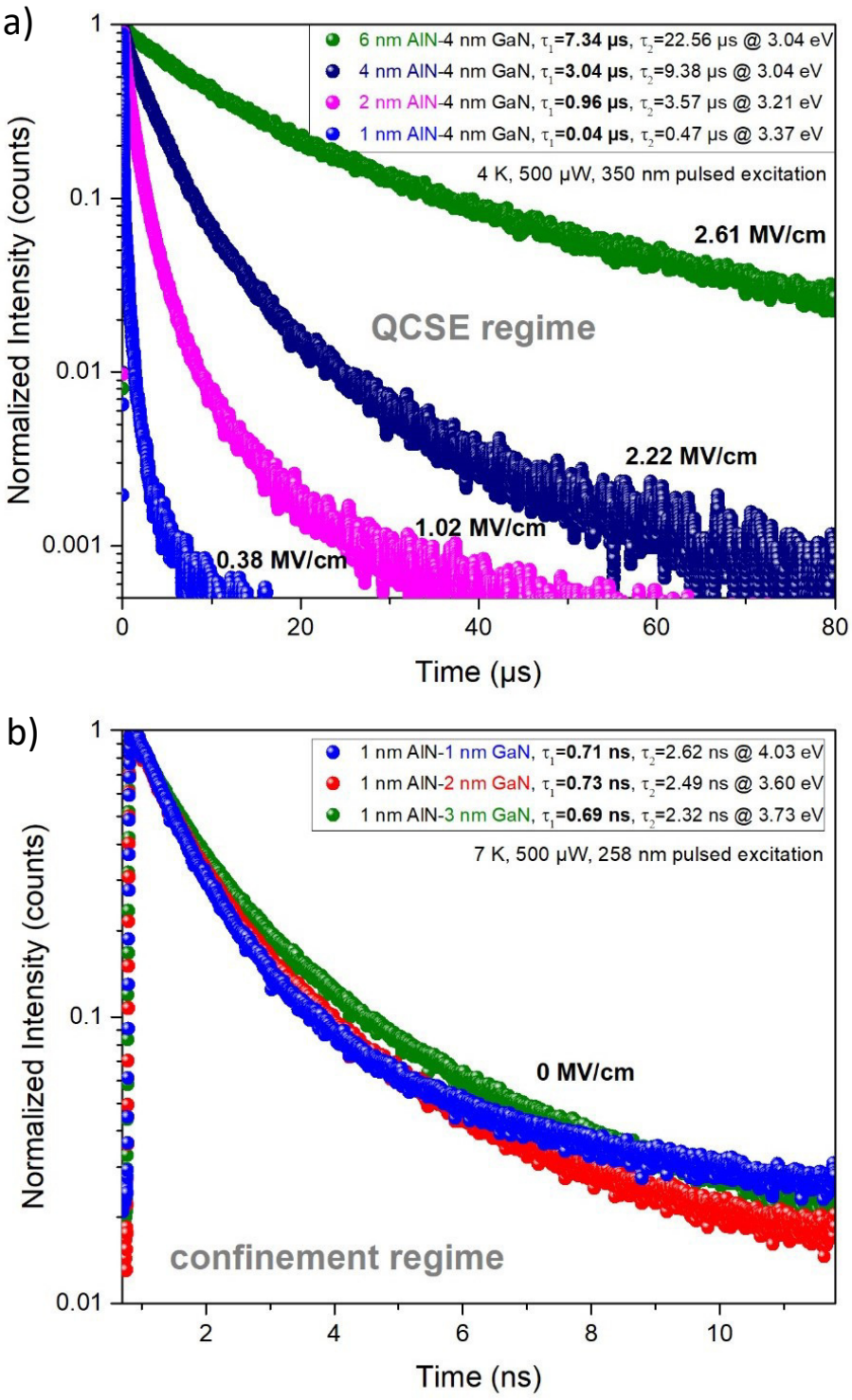

Figure 6.31: Time-resolved photoluminescence (TRPL) transients show the correlation between the decreasing exciton decay times for reduced electric field strengths (chapter 6.1.1) in the equally sized NDs of the QCSE regime samples (a), besides the fast, constant decay times in absence of built-in fields within the differently sized NDs of the confinement regime samples. The exciton lifetime fits results (see equation 6.1) are noted in the respective legends. Lifetimes with significantly more counts are bold. All TRPL transients displayed here, are recorded at the ND luminescence maxima at low temperatures but with high excitation power.

The overall decrease of the decay time from 7.34 µs down to 0.7 ns (in Figure 6.31), the latter being comparable to the exciton lifetimes of excitons in InAs/GaAs quantum dots [132], proves the vanishing electric field strength within the NDs of the confinement regime samples. The approximately constant decay times for the confinement regime samples under triplication of the ND thickness from 1 nm to 3 nm are in perfect accordance to the numerically predicted, approximately constant electron-hole overlap of 93 % shown in Figure 6.3. In contrast to the results of Langer et al. [9], who demonstrated the dependence of the exciton lifetime on the thickness of non-IFGARD/conventional, unstrained GaN/Al(0.24)Ga(0.76)N quantum wells, all of our samples within the confinement regime show the exciton lifetime of approximately 0.7 ns, which is close to the approximately 0.5 ns Langer et al. [9] determined for their 1-nm-thick quantum well only. Please be aware, that the conventional GaN/Al(0.24)Ga(0.76)N quantum wells investigated by Langer et al. [9] incorporate only a fourth of the field strength found in conventional GaN/AlN quantum wells, but also only a fourth of the potential well deepness.

The simple comparison of decay transients presented in this chapter nicely demonstrates the immense beneficial impact of IFGARD on the recombination dynamics in GaN NDs.

6.3 IFGARD nanodiscs in comparison with “conventional” structures

This chapter compares the presented experimental IFGARD emission energies in this work to experimental data for conventional GaN QWs published in the scientific literature.

The existing literature about GaN/AlN QWs is not as comprehensive as for GaN/AlGaN QWs. But, as the GaN/AlGaN QWs do only differ in approximately proportionally smaller potential walls and crystal polarizations relative to the corresponding Ga fraction in the AlGaN, publications dealing with GaN/AlGaN QWs can be consulted, if non-polar GaN/AlGaN quantum wells had been investigated. Together with the publications that experimentally investigated polar c-plane

GaN/AlN QWs [29], [89]–[91], [98], [99], [101], enough data exists to prove the IFGARD to be functional. Therefore, Figure 2.1 comprises experimentally recorded (all unconnected symbols) and numerically predicted (black line connecting small squares) emission energies as a function of ND/QW thickness from this IFGARD investigation (black squares, red dots) complemented with the data published in Refs. [29], [89]–[91], [98], [99], [101] (green squares, red triangles, red crosses). The conventional GaN/AlN QW data points (red triangles and crosses) reach emission energies below the bulk GaN luminescence at 3.47 eV by following an approximately linear trend. Green and black squares, however, represent unpolar GaN QWs/NDs, which follow the converging trend of the emission energies for increasing QW/ND thicknesses that is predicted by the numeric simulation for [0001], polar IFGARD-GaN/AlN QWs (black line connecting small squares) with perfectly shielded zero built-in field strength. Besides, also the data for the nominally semi-polar [11-22] GaN/AlN QWs in Ref. [101] exhibit emission energies with a much flatter slope, being qualitatively and quantitatively very close to the emission energies in our thicker confinement regime samples. By comparing experimental data to simulations in Ref [104], the electric field strength within these [11-22] GaN QWs was determined to lay between +0.6 MV/cm and -0.55 MV/cm, with the QWs being fully strained on AlN and fully strained on GaN, respectively. Their x-ray diffraction study of these [11-22] GaN QWs, however, indicates a strain state intermediate between fully relaxed (on GaN) and fully strained (on AlN). Hence, as they claim that the electric field is between 0.6 and -0.55 MV/cm and that the emission energies of the thicker QWs are close to the data for the confinement regime samples, in Ref. [104], the 8 to 12 ML thick QWs presumably exhibit no built-in electric field strength as it is the case for the confinement regime samples. However, be aware that for the calculations in Ref. [104] the material parameters of Ref. [98] have been used, which neglect the elastic constant E_{44} as well as the piezoelectric constant e_{15}.

Figure 6.32 nicely illustrates, that the presented IFGARD is able to compete with the semi- and non-polar growth approaches to overcome the issues coming along with the QCSE, but it has the advantage to not being reliant on any special growth procedure. Additionally, the common use of the confinement effect to compensate the QCSE is not necessary. Even larger QWs would emit with adequate efficiency.

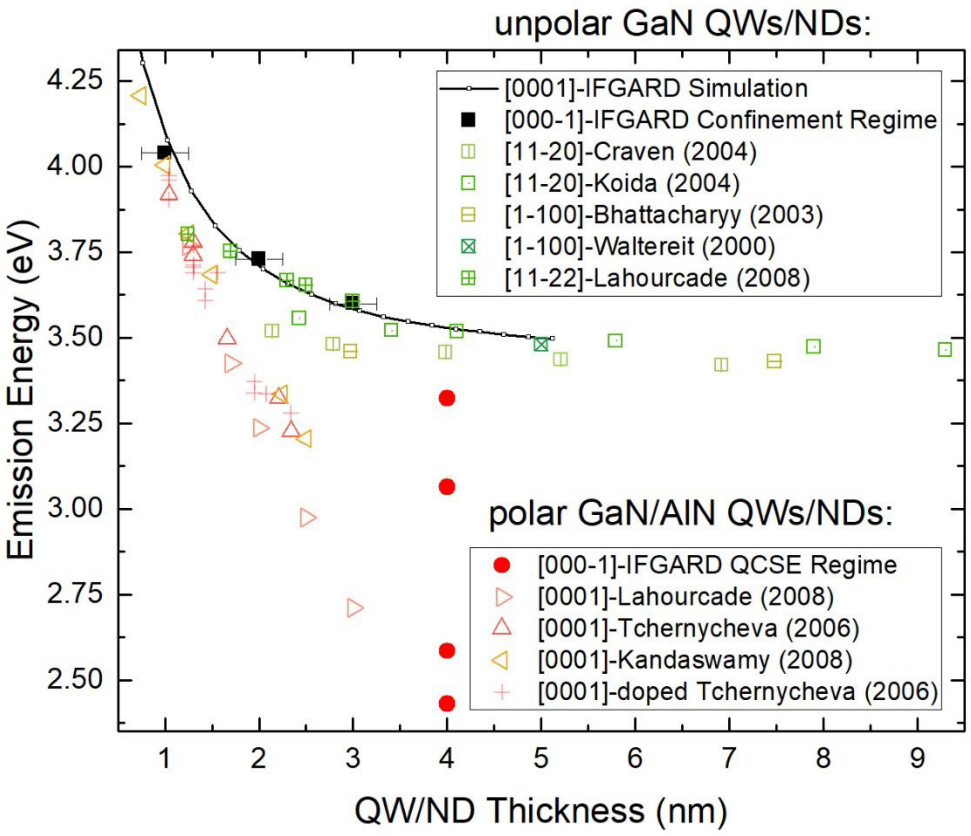

Figure 6.32: Direct comparison of the experimentally determined emission energies for the different ND samples in the confinement regime (black squares) and the QCSE regime (red dots) to numeric results for GaN/AlN IFGARD quantum wells (black line) exhibiting totally shielded polarization fields (built-in field strength = 0 MV/cm). Published values for pure GaN QWs with nonpolar growth directions are included as greenish squares [29], [89]–[91], [101] *and confirm the converging trend that is predicted for GaN QWs without built-in fields. While the conventionally grown [0001], fully polar GaN/AlN QWs* [98], [99], [101] *(reddish triangles) emit at much lower emission energies for well widths exceeding 1 nm. Even doping in the order of* $5 \cdot 10^{19}/cm^3$ *(red crosses) does not significantly alter the emission energies of the polar GaN/AlN QWs.*

7 Conclusion

In this thesis, the successful application of an approach to defeat the quantum-confined Stark effect (QCSE) by a novel semiconductor design, named Internal-Field-Guarded-Active-Region Design (IFGARD), was demonstrated with real-world heterostructures, for the first time. GaN nanowires (NWs) containing 40x GaN nanodiscs (NDs) each embedded in AlN barriers realized the IFGARD, grown in the workgroup of Martin Eickhoff by PAMBE along the most polar $[000\bar{1}]$ c-axis of the wurtzite crystal structure. Due to the lateral growth of AlN, the NWs exhibit a cone-shape besides an AlN shell. As evidenced in this thesis, despite the IFGARD of the NDs, the cone-shape of the NWs induces a residual, built-in electric field in the NDs due to the different net interface charges of adjacent interfaces. The cone-shape angle gets smaller with reduced AlN barrier thickness until the cone-shape turns into a straight shape where the IFGARD is able to fully annihilate any built-in fields. In sum, this discovery facilitates a unique tuning capability of the large inherent fields within c-plane, pure GaN/AlN quantum well or quantum dot structures. Furthermore, using two complementary sample series the behavior of excitons influenced by a pure 1-dimensional confinement could be investigated in such c-plane structures undisturbed by the QCSE. Figure 7.1 summarizes the most important measurement results.

The optical properties of the IFGARD NDs were investigated by micro-photoluminescence (μ-PL) and time-resolved photoluminescence (TRPL) measurements, which led to the second discovery of triexponential decay processes of excitonic complexes in field-free c-plane GaN/AlN ND excitons, never shown before.

The triexponential behavior was traced back to different types of bound as well as unbound ND excitons and their relaxation channels, as due to the absence built-in fields only, a change from biexponential to triexponential decay when scanning the ND luminescence from the low to the high energy side was detectable for the first time. Hence, the IFGARD will most probably stimulate further discoveries as it facilitates the possibility to investigate trapped charge carriers and their vicinity-interplay in a field-free environment in group-III-nitride heterostructures grown in c direction, which was not accessible before.

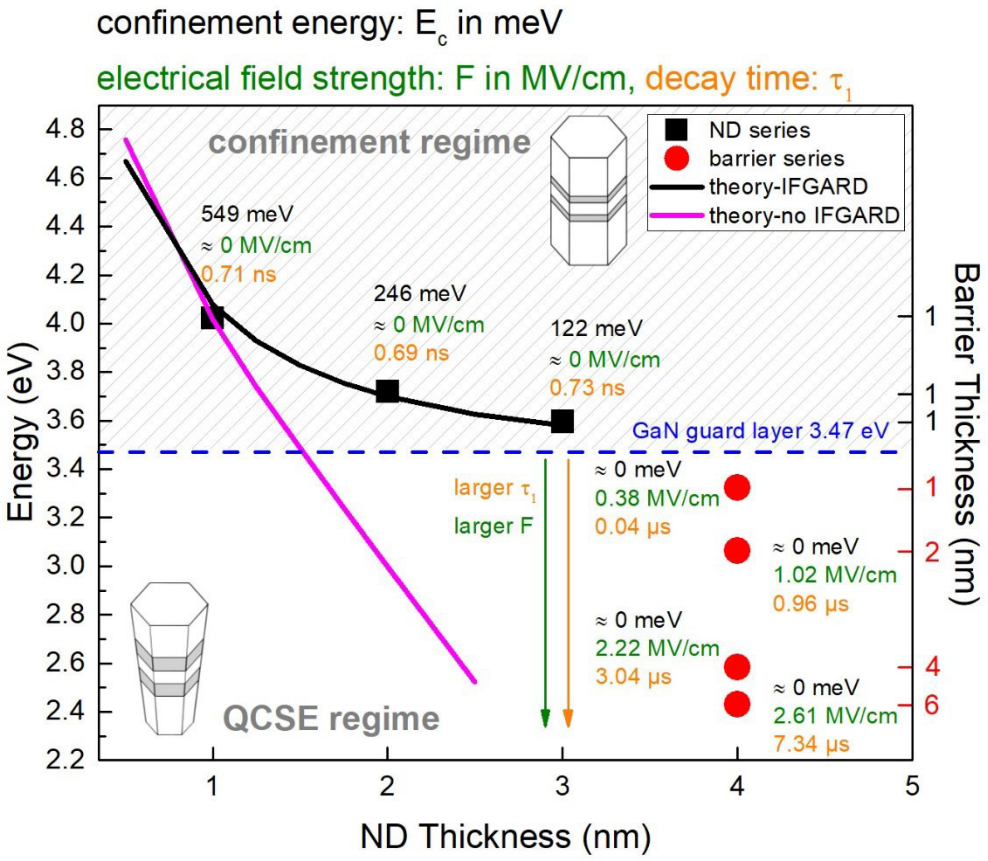

Figure 7.1: This Figure summarizes the most important results used for the proof of the successful tuning and annihilation of the QCSE in the investigated IFGARD nanodiscs (NDs) within a plot of the nanodisc emission energies vs. the barrier and nanodisc thicknesses separating the confinement regime, marked by black squares and the QCSE regime (red dots) from each other. It shows the determined, residual built-in electric field strengths (green values), the exciton confinement energies (black values), and the dominant decay times (orange values). Additionally, the geometric nanowire structure in the respective pure confinement or QCSE regime are sketched, including the comparison with numeric calculations of QWs without or full (black vs. pink) built-in electric fields.

Finally, a tremendously improved temperature stability of the luminescence stemming from the thinnest, field-free, only 1-nm-thick GaN/AlN NDs was demonstrated showing the promising capabilities of the new IFGARD design, not only for UV-photonics but all photonic applications by utilizing originally polar heterostructures without their inherent electric fields.

7.1 Outlook

7.1.1 Interesting aspects and discussion for a real device

One of the most interesting questions after evidencing the successful application of IFGARD is, "**is this concept relevant for the photonic industry?"** To answer this question, this outlook discusses some of the aspects of the IFGARD that seem to be disadvantageous, like the right choice of the substrate, the absorption in the top guard layer, and other aspects that give a competitive edge for electrical devices.

7.1.1.1 The right substrate

During the introduction of the IFGARD (chapter 4) the importance of the lower guard layer to be of the same material as the QWs is explained. In terms of the here investigated NWs, the deviating substrate material Si from the GaN NDs material was explained to be negligible due to the small interface area between the substrate and the NWs (see chapter 5 Samples). For QWs, this would not be the case anymore. In the case of GaN QWs, the use of GaN substrates would be appropriate leading to higher production costs compared to the use of, e.g., cheaper Si substrates. Besides that, investigating the influence of space charges at a Si to GaN interface on an IFGARD will be a task for future work. Another possibility is, to use laser-lift off methods to lift of the IFGARD structure from a cheaper substrate after the growth [82].

7.1.1.2 The absorption of photons in the top guard layer

Another aspect that creates doubts, is the top guard layer consisting of the same material as the QW. The guard layer absorbs photons generated in the underlying QW, which should decrease the efficiency of IFGARD devices. The theoretic predictions claim that as long as the dimension of the guard layer in the direction of the emitted photons does not exceed the wavelength of the photons, the gain resulting from the boosted excitonic oscillator strength due to the IFGARD, does compensate those absorption losses. This was evidenced in this work for a top guard layer thickness of approximately $1/10^{th}$ of the emitted wavelengths. But, "How thick need the guard layers to be to still guarantee the function of IFGARD?" Numeric

simulations for predicting the spontaneous polarization in wurtzite crystals considered the second next neighbor interaction of the atoms [131]. Consequently, the guard layer should be at least two monolayers thick (= *c*, lattice parameter of the wurtzite crystal, Figure 2.3) for perfectly flat layers without thickness fluctuations.

Considering a guard layer thinner than the QW has additional advantages. If the guard layer is smaller than the QW itself, the band gap of the guard layer would be larger if compared to the underlying QW and could not absorb its photons. In the first samples series, presented in this work, a top guard layer thickness of 20 nm was chosen since it was expected to show the observed luminescence at 3.47 eV close to bulk GaN. Thus, a clear separation between the guard layer and the ND luminescence was feasible for most of the samples.

7.1.1.3 The advantage of low current operation of a device

In the scientific III-nitrides community it is a widespread belief that the QCSE is not a problem for, e.g., the LED industry as the built-in electric field can be screened just by injecting a large amount of charge carriers into the photon emitting region of a device. This requires large current densities lead through the active region of, e.g., an LED structure resulting in a high temperature of the device itself that reduces the service life of the LED and making it necessary to add effective cooling mechanisms. On the other hand, screening of the QCSE by charge-carriers causes an undesired wavelength shift of the emitted photons as a function of the applied current densities, in the case of, e.g., light density dimming without using a pulsed operating mode, which is often undesired too as it causes a stroboscopic effect. Summarizing already these aspects: An LED structure based on a heterostructure that is plagued by the QCSE needs to be designed for very specific electrical operation conditions and is therefore very unflexible in its design. Another aspect is the efficiency droop resulting from Auger recombinations, becoming significant with high carrier concentrations within the active region for, e.g., InGaN based LEDs [133]–[135]. Here, it is a well-known phenomenon that with increasing current the efficiency first increases and after reaching a maximal efficiency, decreases again with further enhancement of the applied current [136]–[138]. Thus, again it is a delicate trade-off

between high current densities for screening the QCSE but not so high current densities for not having the Auger droop kicking in. All those disadvantages due to the QCSE can be eliminated by the IFGARD giving back much more flexibility in designing, e.g., photon emitting devices at specific emission energies, which are purely tuned by the band gap of the utilized active region material and the confinement energy in quantum-sized heterostructures. Furthermore, by being able to change the material compositions in each of the IFGARD layers separately, more advanced band edge landscapes become realizable.

8 Publications and conference contributions

Articles:

1. **Green (In,Ga,Al)P-GaP light-emitting diodes grown on high-index GaAs surfaces**

   N. N. Ledentsov, V. A. Shchukin, J. Lyytikäinen, O. Okhotnikov, Yu. M. Shernyakov, A. S. Payusov, N. Yu. Gordeev, M. V. Maximov, S. Schlichting, F. Nippert, and A. Hoffmann,

   Applied Physics Letters **105**, 181902 (2014)

2. **Green (In,Ga,Al)P–GaP Light–Emitting Diodes grown on high–index GaAs surfaces**

   N. N. Ledentsov, V. A. Shchukin, J. Lyytikäinen, O. Okhotnikov, N. A. Cherkashin, Yu. M. Shernyakov, A. S. Payusov, N. Yu. Gordeev, M. V. Maximov, S. Schlichting, F. Nippert, and A. Hoffmann,

   Proc. of SPIE Vol. 9383 93830E-1

3. **Molecular nitrogen acceptors in ZnO nanowires induced by nitrogen plasma annealing**

   C. Ton-That, L. Zhu, M. N. Lockrey, and M. R. Phillips, B. C. C. Cowie, A. Tadich, and L. Thomsen, S. Khachadorian, S. Schlichting, N. Jankowski, and A. Hoffmann,

   Physical Review B **92**, 024103 (2015)

4. **Growth and structure of In0.5Ga0.5Sb quantum dots on GaP(001)**

   E. M. Sala, G. Stracke, S. Selve, T. Niermann, M. Lehmann, S. Schlichting, F. Nippert, G. Callsen, A. Strittmatter , and D. Bimberg,

   Applied Physics Letters **109**, 102102 (2016)

5. **Electronic excitations stabilized by a degenerate electron gas in semiconductors**

   C. Nenstiel, G. Callsen, F. Nippert, T. Kure, M. R. Wagner, S. Schlichting, N. Jankowski, M. P. Hoffmann, S. Fritze, A. Dadgar, A. Krost, A. Hoffmann and, F. Bechstedt,

   (Submitted to Advanced Science Nov 2017)

6. **Tuning of the Quantum-Confined Stark Effect in Wurtzite $[000\bar{1}]$ Group-III-Nitride Nanostructures by the Internal-Field-Guarded-Active-Region Design**

   S. Schlichting, G. M. O. Hönig, J. Müßener, P. Hille, T. Grieb, J. Teubert, J. Schörmann, M. R. Wagner, A. Rosenauer, M. Eickhoff, A. Hoffmann, and G. Callsen,

   (arXiv:1707.06882, July 2017. To be submitted to Communications Physics.)

Talks:

1. **Influence of antimony doping on optical and structural properties of ZnO nanowires**

   Sarah Schlichting, Thomas Kure, Alexander Franke, Eswaran Senthil Kumar, Faezeh Mohammadeigi, Simon Watkins, Axel Hoffmann

   DPG Spring Meeting 2014, Dresden, Germany

2. **Luminescence properties of green (InGaAl)P-GaP LED grown on different orientated GaAs substrates**

   S. Schlichting, N. N. Ledentsov, V. A. Shukin, J. Lyytikäinen, O. Okhotnikov, Yu. M. Shernyakov, A. S. Payusov, N. Yu. Gordeev, M. V. Maximov, C. Nenstiel, F. Nippert, and A. Hoffmann

   DPG Spring Meeting 2015, Berlin, Germany

3. **Luminescence properties of green (InGaAl)P-GaP LED grown on different orientated GaAs substrates**

   S. Schlichting, N. N. Ledentsov, V. A. Shukin, J. Lyytikäinen, O. Okhotnikov, Yu. M. Shernyakov, A. S. Payusov, N. Yu. Gordeev, M. V. Maximov, C. Nenstiel, F. Nippert, and A. Hoffmann

   NEWLED Meeting 2015, Rome, Italy

4. **Γ-to-X Bandgap Cross-Over in (In,Ga,Al)P Epilayers Grown on (100) and High-Index GaAs Substrates**

   S. Schlichting, C. Nenstiel, F. Nippert, T. Kure, N. N. Ledentsov, V. A. Shchukin, J. Lyytikäinen, O. Okhotnikov, Yu. M. Shernyakov, A. S. Payusov, N. Yu. Gordeev, M. V. Maximov, and A. Hoffmann

   Photonics West 2016, San Fracisco, USA

5. **Enhanced UV emission of polar III-nitride heterostructures by effective suppression of the quantum confined Stark effect**

   M. R. Wagner, S. Schlichting, J. Müßener, P. Hille, J. Teubert, J. Schörmann, M. Eickhoff, A. Hoffmann, G. Callsen and G. M. O. Hönig

   ICNS, 2017

6. **QCSE tuning in polar GaN/AlN heterostructures**

   G. M. O. Hönig, S. Schlichting, M. R. Wagner, J. Müßener, P. Hille, J. Teubert, J. Schörmann, M. Eickhoff, A. Hoffmann and G. Callsen

   Photonics West 2018, San Francisco, USA

Poster:

1. **Origin of Doping Related Raman Modes in Sb Doped ZnO Nanowires via DFT Calculations**

   Sarah Schlichting, Thomas Kure, Alexander Franke, Sevak Khachadorian, Roland Gillen, Markus R. Wagner, Eswaran Senthil Kumar, Faezeh Mohammadbeigi, Simon Watkins, Janina Maultzsch and Axel Hoffmann,

   8th International Workshop on Zinc Oxide and Related Materials (IWZnO 2014), Ontario, Canada

2. **Tuning of the quantum-confined Stark effect in wurtzite [0001] nanostructures by the Internal-Field-Guarded-Active-Region Design**

   S. Schlichting, G. M. O. Hönig, M. R. Wagner, J. Müßener, P. Hille, J. Teubert, J. Schörmann, M. Eickhoff, A. Hoffmann, and G. Callsen

   CSW 2017, Berlin, Germany

9 Acknowledgment/Danksagung

„Es gibt nur zwei Arten zu leben. Entweder so als wäre nichts ein Wunder oder so als wäre alles ein Wunder.“

Albert Einstein

Nichts ist selbstverständlich und deswegen möchte ich mich an dieser Stelle bei den Menschen bedanken, die mich während meiner Doktorandenzeit an der Technischen Universität Berlin auf verschiedene Arten und Weisen unterstützt haben.

Herr Prof. Dr. Axel Hoffmann hat mich durch meine komplette Studienzeit, vom Bachelor bis zur Dissertation begleitet und betreut. Seine Tür stand immer offen, um über die Physik zu sprechen und zu diskutieren. Auch bei unerwarteten Herausforderungen konnte er immer eine Lösung finden. Herr Prof. Hoffmann gab mir genügend Freiraum, um mich selbstständig entwickeln zu können. Dazu zählte, dass ich die Möglichkeit bekam, zu verschiedenen Konferenzen zu fahren, um meine Forschungsthemen zu präsentieren und mit anderen Wissenschaftlern in Kontakt zu treten. Ebenfalls gestattete er mir, während meiner Promotionszeit, einen zweimonatigen Aufenthalt bei Osram OS in Regensburg, was keine Selbstverständlichkeit ist und wofür ich ihm sehr dankbar bin.

Die **Arbeitsgruppe** bildete eine sehr kompetente und starke Gruppe, die jederzeit bei Problemen im Labor mit ihrem Wissen zur Seite stand und half. Auch bei der Vorbereitung für Konferenzbeiträge konnte ich mich auf die Kritik meiner Kollegen verlassen und somit einen guten Beitrag liefern. Auch bei schwierigen Themen und starker zeitlicher Einschränkung standen sie hilfsbereit an meiner Seite. Ich hatte das Glück meine Promotionszeit mit engagierten, motivierten, freundlichen und sehr fachkundigen Kollegen zu verbringen, was neben der Physik selbst dazu beitrug, gerne zur Uni zu gehen.

Nadja Jankowski hat sowohl als Kollegin als auch als gute Freundin immer an meiner Seite gestanden. Seit dem Anfang meines Studiums haben wir viele Herausforderungen gemeinsam bestritten. Auch bei privaten Hürden hatte sie immer ein offenes Ohr für mich und ich konnte auf ihre Unterstützung zählen.

Herr Dr. Gordon Callsen und **Herr Dr. Gerald Hönig**, die Miterfinder von IFGARD, haben mir ihr spannendes Thema anvertraut. Jederzeit konnte ich mit ihnen über neue Ergebnisse diskutieren, trotz ihrer eigenen Tätigkeiten in anderen Institutionen.

Der **Arbeitsgruppe Bremen** danke ich für die Herstellung der Proben und der Bereitstellung von den SEM Bildern und der STEM Analyse.

Herr Prof. Dr. Andreas Waag danke ich für die Begutachtung meiner Arbeit.

Meiner gesamten **Familie** gilt ein ganz besonderer Dank. Sie stand immer hinter mir und hat mich in jeglicher Form unterstützt, um mir ein unbeschwertes und erfolgreiches Studium zu ermöglichen.

10 Bibliography

[1] B. Gil, *III-Nitride Semiconductors and Their Modern Devices*. Oxford University Press, 2013.

[2] S. Nakamura, S. Pearton, and G. Fasol, *The Blue Laser Diode. The Complete Story*. Springer, 2013.

[3] S. Nakamura and S. Fasol, *The blue laser diode-GaN light emitters and lasers*. Springer, 1997.

[4] G. Hönig *et al.*, "Manifestation of unconventional biexciton states in quantum dots," *Nat. Commun.*, vol. 5, p. 5721, 2014.

[5] G. Callsen *et al.*, "Steering photon statistics in single quantum dots: From one-to two-photon emission," *Phys. Rev. B*, vol. 87, no. 24, p. 245314, Jun. 2013.

[6] M. Holmes, S. Kako, K. Choi, P. Podemski, M. Arita, and Y. Arakawa, "Measurement of an Exciton Rabi Rotation in a Single GaN/Al(x)Ga(1-x)N Nanowire-Quantum Dot Using Photoluminescence Spectroscopy: Evidence for Coherent Control," *Phys. Rev. Lett.*, vol. 111, no. 5, p. 57401, Jul. 2013.

[7] A. Schliwa, G. Hönig, and D. Bimberg, "Electronic Properties of III-V Quantum Dots," in *Multi-Band Effective Mass Approximations*, vol. 94, M. Ehrhardt and T. Koprucki, Eds. Cham: Springer, 2014, pp. 57–85.

[8] O. Ambacher and J. Majewski, "Pyroelectric properties of Al (In) GaN/GaN hetero-and quantum well structures," *J. Phys. Condens. Matter*, vol. 14, p. 3399, 2002.

[9] R. Langer *et al.*, "Giant electric fields in unstrained GaN single quantum wells," *Appl. Phys. Lett.*, vol. 74, no. 25, p. 3827, 1999.

[10] O. Ambacher *et al.*, "Electronics and sensors based on pyroelectric AlGaN/GaN heterostructures," *Phys. Status Solidi C*, vol. 0, no. 6, p. 1878, Sep. 2003.

[11] F. Bernardini and V. Fiorentini, "Macroscopic polarization and band offsets at nitride heterojunctions," *Phys. Rev. B*, vol. 57, no. 16, p. 9427, 1998.

[12] O. Ambacher *et al.*, "Role of Spontaneous and Piezoelectric Polarization Induced Effects in Group-III Nitride Based Heterostructures and Devices," *Phys. Status Solidi B*, vol. 216, no. 1, p. 381, Nov. 1999.

[13] M. Leroux *et al.*, "Quantum confined Stark effect due to built-in internal polarization fields in (Al,Ga)N/GaN quantum wells," *Phys. Rev. B*, vol. 58, no. 20, p. 13371, 1998.

[14] N. Grandjean, B. Damilano, S. Dalmasso, M. Leroux, M. Laügt, and J. Massies, "Built-in electric-field effects in wurtzite AlGaN/GaN quantum wells," *J. Appl. Phys.*, vol. 86, no. 7, p. 3714, 1999.

[15] T. Nakaoka, S. Kako, and Y. Arakawa, "Quantum confined Stark effect in single self-assembled GaN/AlN quantum dots," *Phys. E Low-Dimensional Syst. Nanostructures*, vol. 32, p. 148, 2006.

[16] R. Cingolani *et al.*, "Spontaneous polarization and piezoelectric field in GaN/Al 0.15 Ga 0.85 N quantum wells: Impact on the optical spectra," *Phys. Rev. B*, vol. 61, no. 4, p. 2712, 2000.

[17] V. Fiorentini, F. Bernardini, F. Della Sala, A. Di Carlo, and P. Lugli, “Effects of macroscopic polarization in III-V nitride multiple quantum wells,” *Phys. Rev. B*, vol. 60, no. 12, p. 8849, Sep. 1999.

[18] C. Kindel *et al.*, “Spectral diffusion in nitride quantum dots: Emission energy dependent linewidths broadening via giant built-in dipole moments,” *Phys. Status Solidi RRL*, vol. 8, no. 5, p. 408, 2014.

[19] S. Kako, M. Miyamura, K. Tachibana, K. Hoshino, Y. Arakawa, and M. Miyamura, “Size-dependent radiative decay time of excitons in GaN/AlN self-assembled quantum dots,” *Appl. Phys. Lett.*, vol. 83, no. 5, p. 984, 2003.

[20] J. Renard, R. Songmuang, G. Tourbot, C. Bougerol, B. Daudin, and B. Gayral, “Evidence for quantum-confined Stark effect in GaN/AlN quantum dots in nanowires,” *Phys. Rev. B*, vol. 80, no. 12, p. 121305, 2009.

[21] J. Müßener *et al.*, “Probing the internal electric field in GaN/AlGaN nanowire heterostructures,” *Nano Lett.*, vol. 14, no. 9, p. 5118, 2014.

[22] C. Kindel *et al.*, “Exciton fine-structure splitting in GaN/AlN quantum dots,” *Phys. Rev. B*, vol. 81, no. 24, p. 241309(R), Jun. 2010.

[23] I. A. Ostapenko *et al.*, “Large internal dipole moment in InGaN/GaN quantum dots,” *Appl. Phys. Lett.*, vol. 97, no. 6, p. 63103, 2010.

[24] T. Bretagnon *et al.*, “Radiative lifetime of a single electron-hole pair in GaN/AlN quantum dots,” *Phys. Rev. B*, vol. 73, no. 11, p. 113304, 2006.

[25] T. Bretagnon *et al.*, “Time dependence of the photoluminescence of GaN/AlN quantum dots under high photoexcitation,” *Phys. Rev. B*, vol. 68, no. 20, p. 205301, Nov. 2003.

[26] C. Adelmann *et al.*, “Growth and optical properties of GaN/AlN quantum wells,” *Appl. Phys. Lett.*, vol. 82, no. 23, p. 4154, 2003.

[27] V. Fiorentini, F. Bernardini, and O. Ambacher, “Evidence for nonlinear macroscopic polarization in III–V nitride alloy heterostructures,” *Appl. Phys. Lett.*, vol. 80, no. 7, p. 1204, 2002.

[28] T. Paskova, *Nitrides with Nonpolar Surfaces: Growth, Properties, and Devices*. WILEY-VCH, 2008.

[29] P. Waltereit *et al.*, “Nitride semiconductors free of electrostatic fields for efficient white light-emitting diodes,” *Nature*, vol. 406, no. 6798, p. 865, 2000.

[30] M. J. Paisley, Z. Sitar, J. B. Posthill, and R. F. Davis, “Growth of cubic phase gallium nitride by modified molecular-beam epitaxy,” *J. Vac. Sci. Technol. A*, vol. 7, no. 3, p. 701, 1989.

[31] P. Hille *et al.*, “Screening of the quantum-confined Stark effect in AlN-GaN nanowire superlattices by germanium doping,” *Appl. Phys. Lett.*, vol. 104, no. 10, p. 102104, 2014.

[32] R. M. Kemper *et al.*, “Anti-phase domains in cubic GaN,” *J. Appl. Phys.*, vol. 110, no. 12, p. 123512, 2011.

[33] M. Bürger *et al.*, “Lasing properties of non-polar GaN quantum dots in cubic aluminum nitride microdisk,” *Appl. Phys. Lett.*, vol. 103, no. 2, p. 21107, 2013.

[34] S. Kako, M. Holmes, S. Sergent, M. Bürger, D. J. As, and Y. Arakawa, “Single-photon emission from cubic GaN quantum dots,” *Appl. Phys. Lett.*, vol. 104, no. 1, p. 11101, 2014.

[35] T. Schupp *et al.*, “Zinc-blende GaN quantum dots grown by vapor-liquid-solid condensation,” *J. Cryst. Growth*, vol. 323, no. 1, p. 286, 2011.

[36] S. Sergent, S. Kako, M. Bürger, D. J. As, and Y. Arakawa, “Narrow spectral linewidth of single zinc-blende GaN/AlN self-assembled quantum dots,” *Appl. Phys. Lett.*, vol. 103, p. 151109, 2013.

[37] R. M. Farrell, E. C. Young, F. Wu, S. P. DenBaars, and J. S. Speck, “Materials and growth issues for high-performance nonpolar and semipolar light-emitting devices,” *Semicond. Sci. Technol.*, vol. 27, no. 2, p. 24001, 2012.

[38] G. M. O. Pahn, G. Callsen, and A. Hoffmann, “Semiconductor device having an internal-field-guarded active region, International Patent Publication Number WO 2017/042368 A1,” International Patent Application Number WO 2017/042368, 2017.

[39] G. M. O. Pahn, G. Callsen, and S. Westerkamp, “Semiconductor device having an internal-field-guarded active region, European Patent Office Application Number EP17160160.2,” European Patent Office application number EP17160160.2, 2017.

[40] G. M. O. Hönig, S. Westerkamp, A. Hoffmann, and G. Callsen, “Shielding electrostatic fields in polar semiconductor nanostructures,” *Phys. Rev. Appl.*, vol. 7, no. 2, p. 24004, Feb. 2017.

[41] N. Vico Triviño *et al.*, “High quality factor two dimensional GaN photonic crystal cavity membranes grown on silicon substrate,” *Appl. Phys. Lett.*, vol. 100, no. 7, p. 71103, 2012.

[42] D. M. Mead, “Wave Propagation in Continuous Periodic Structures: Research Contributions From Southampton, 1964-1995,” *J. Sound Vib.*, vol. 190, no. 3, p. 495, 1996.

[43] E. Chávez-Ángel *et al.*, “Reduction of the thermal conductivity in free-standing silicon nano-membranes investigated by non-invasive Raman thermometry,” *APL Mater.*, vol. 2, no. 1, p. 12113, 2014.

[44] J. F. Muth *et al.*, “Absorption coefficient, energy gap, exciton binding energy, and recombination lifetime of GaN obtained from transmission measurements,” *Appl. Phys. Lett.*, vol. 71, no. May 2016, p. 2572, 1997.

[45] S. Schlichting *et al.*, “Tuning of the Quantum-Confined Stark Effect in Wurtzite [000-1] Group-III-Nitride Nanostructures by the Internal-Field-Guarded-Active-Region Design,” *arXiv:1707.06882 [physics.app-ph]*.

[46] I. Vurgaftman, J. R. Meyer, and L. R. Ram-Mohan, “Band parameters for III–V compound semiconductors and their alloys,” *J. Appl. Phys.*, vol. 89, no. 11, p. 5815, 2001.

[47] K. Takahashi, A. Yoshikawa, and A. Sandhu, “Wide Bandgap Semiconductors Fundamental Properties and Modern Photonic and Electronic Devices.”

[48] D. J. As, “Cubic group-III nitride-based nanostructures-basics and applications in optoelectronics,” *Microelectronics J.*, vol. 40, no. 2, pp. 204–209, 2009.

[49] J. Simon *et al.*, “Direct comparison of recombination dynamics in cubic and hexagonal GaN/AlN quantum dots,” *Phys. Rev. B*, vol. 68, no. 3, p. 35312, 2003.

[50] C. Y. Cardona, *Fundamentals of Semiconductors*. Heidelberg: Springer, 2010.

[51] O. Ambacher *et al.*, “Two-dimensional electron gases induced by spontaneous and piezoelectric polarization charges in N-and Ga-face AlGaN/GaN heterostructures,” *J. Appl. Phys*, vol. 85, no. 6, pp. 3222–3233, 1999.

[52] S. Kremers, “Optische Eigenschaften von Phasenwechselmaterialien,” Technischen Universität Berlin, 2011.

[53] M. Winkelnkemper, “Electronic Structure of Nitride-based Quantum Dots.”

[54] D. Bimberg, M. Grundmann, and N. N. Ledentsov, *Quantum Dot Heterostructures*. John Wiley & Sons.

[55] S. F. Borg, *Matrix-Tensor Methods in Continuum Mechanics*. D. Van Nostrand Company, Inc., 1963.

[56] T. Hanada, “Basic Properties of ZnO, GaN, and Related Materials,” in *Oxide and Nitride Semiconductors Processing, Properties, and Applications*, Springer, 2009.

[57] G. M. O. Hönig, “Mehrteilchenzustände in Halbleiter-Quantenpunkten,” Technischen Universität Berlin, 2015.

[58] E. T. Yu, X. Z. Dang, P. M. Asbeck, S. S. Lau, and G. J. Sullivan, “Spontaneous and piezoelectric polarization effects in III–V nitride heterostructures,” *J. Vac. Sci. Technol. B*, vol. 17, no. 4, 1999.

[59] M. Winkelnkemper, “Elektronische Eigenschaften niederdimensionaler Halbleiterstrukturen mit Wurtzitstruktur,” 2004.

[60] M. Suzuki, T. Uenoyama, and A. Yanase, “First-principles calculations of effective-mass parameters of AlN and GaN,” *Phys. Rev. B*, vol. 52, no. 11, pp. 8132–8139, 1995.

[61] N. E. Christensen and I. Gorczyca, “Optical and Structural Properties of III-V nitrides under pressure,” *Phys. Rev. B*, vol. 50, no. 7, pp. 4397–4415, 1994.

[62] S. L. Levinshtein, M.E. Rumyantsev and M. . Shur, *Properties of Advanced Semiconductor Materials GaN, AlN, InN, BN, SiC, SiGe*. John Wiley & Sons, Inc., New York, 2001.

[63] F. Rol *et al.*, “Probing exciton localization in nonpolar GaN / AlN quantum dots by single-dot optical spectroscopy,” *Phys. Rev. B*, vol. 75, p. 125306, 2007.

[64] R. Maria Kemper *et al.*, “Anti-phase domains in cubic GaN,” *J. Appl. Phys.*, vol. 110, no. 12, pp. 1–6, 2011.

[65] P. Hille, “Advanced Group III-Nitride Nanowire Heterostructures - Self-Assembly and Position-Controlled Growth,” Justus-Liebig-Universität Gießen, 2017.

[66] E. Calleja *et al.*, “Luminescence properties and defects in GaN nanocolumns grown by molecular beam epitaxy,” *Phys. Rev. B - Condens. Matter Mater. Phys.*, vol. 62, no. 24, pp. 16826–16834, 2000.

[67] K. A. Bertness, A. Roshko, N. A. Sanford, J. M. Barker, and A. V. Davydov, “Spontaneously grown GaN and AlGaN nanowires,” *J. Cryst. Growth*, vol. 287, no. 2, pp. 522–527, 2006.

[68] F. Furtmayr *et al.*, “Nucleation and growth of GaN nanorods on Si (111) surfaces by plasma-assisted molecular beam epitaxy - The influence of Si- and Mg-doping,” *J. Appl. Phys.*, vol. 104, no. 3, 2008.

[69] V. Consonni, “Self-induced growth of GaN nanowires by molecular beam epitaxy: A critical review of the formation mechanisms,” *Phys. status solidi - Rapid Res. Lett.*, vol. 7, no. 10, pp. 699–712, 2013.

[70] L. Geelhaar *et al.*, “Axial and radial growth of Ni-induced GaN nanowires,” *Appl. Phys. Lett.*, vol. 91, no. 9, pp. 2005–2008, 2007.

[71] C. Chèze *et al.*, “Direct comparison of catalyst-free and catalyst-induced GaN nanowires,” *Nano Res.*, vol. 3, no. 7, pp. 528–536, 2010.

[72] Ž. Gačević, D. Gómez Sánchez, and E. Calleja, “Formation mechanisms of GaN nanowires grown by selective area growth homoepitaxy,” *Nano Lett.*, vol. 15, no. 2, pp. 1117–1121, 2015.

[73] S. P. Denbaars *et al.*, “Development of gallium-nitride-based light-emitting diodes (LEDs) and laser diodes for energy-efficient lighting and displays,” *Acta Mater.*, vol. 61, pp. 945–951, 2013.

[74] F. Furtmayr, “Nitride Nanowire Heterostructures,” Technische Universität München, 2013.

[75] R. Songmuang, T. Ben, B. Daudin, D. González, E. Monroy, and 1, “Identification of III – N nanowire growth kinetics via a marker technique,” *Nanotechnology*, vol. 21, no. 29, p. 295605, 2010.

[76] F. Furtmayr *et al.*, “Carrier confinement in GaN/Al(x)Ga(1−x)N nanowire heterostructures (0<x<1),” *Phys. Rev. B*, vol. 84, no. 20, p. 205303, 2011.

[77] A. L. Efros, “Interband absorption of light in a semiconductor sphere,” *SPIE milestone Ser.*, vol. 180, p. 71, 2005.

[78] L. Banyai, Y. Z. Hu, M. Lindberg, and S. W. Koch, “Third-order optical nonlinearities in semiconductor microstructures,” *Phys. Rev. B*, vol. 38, no. 12, p. 8142, 1988.

[79] W. Que, “Excitons in quantum dots with parabolic confinement,” *Phys. Rev. B*, vol. 45, no. 19, p. 11036, 1992.

[80] W. Shan, X. C. Xie, J. J. S. Goldenberg, W. Shan, X. C. Xie, and J. J. Song, “Time-resolved exciton luminescence in GaN grown by metalorganic chemical vapor deposition,” *Appl. Phys. Lett.*, vol. 67, no. 17, p. 2512, 1995.

[81] J. S. Im, A. Moritz, F. Steuber, V. Härle, F. Scholz, and A. Hangleiter, “Radiative carrier lifetime, momentum matrix element, and hole effective mass in GaN,” *Appl. Phys. Lett.*, vol. 70, no. 5, p. 631, 1997.

[82] B. Hahn, B. Galler, and K. Engl, “Development of high-efficiency and high-power vertical light emitting diodes,” *Jpn. J. Appl. Phys.*, vol. 53, no. 10, p. 100208, 2014.

[83] A. Reale *et al.*, “Comprehensive description of the dynamical screening of the internal electric fields of AlGaN/GaN quantum wells in time-resolved photoluminescence experiments,” *J. Appl. Phys.*, vol. 93, no. 1, p. 400, 2003.

[84] F. Della Sala *et al.*, “Free-carrier screening of polarization fields in wurtzite GaN/InGaN laser structures,” *Appl. Phys. Lett.*, vol. 74, no. 1999, p. 2002, 1999.

[85] E. Kuokstis *et al.*, “Polarization effects in photoluminescence of C-and M-plane GaN/AlGaN multiple quantum wells,” *Phys. Rev. Lett.*, vol. 81, no. 22, p. 4130, 2002.

[86] K. P. Korona, “Dynamics of excitonic recombination and interactions in homoepitaxial GaN,” *Phys. Rev. B*, vol. 65, no. 23, p. 235312, 2002.

[87] D. Volm *et al.*, “Exciton fine structure in undoped GaN epitaxial films,” *Phys. Rev. B*, vol. 53, no. 24, p. 16543, 1996.

[88] G. Callsen *et al.*, “Analysis of the exciton–LO-phonon coupling in single wurtzite GaN quantum dots,” *Phys. Rev. B*, vol. 92, no. 23, p. 235439, 2015.

[89] M. D. Craven, P. Waltereit, J. S. Speck, and S. P. DenBaars, “Well-width dependence of photoluminescence emission from a-plane GaN/AlGaN multiple quantum wells,” *Appl. Phys. Lett.*, vol. 84, no. 4, p. 496, 2004.

[90] A. Bhattacharyya *et al.*, “Comparative study of GaN/AlGaN MQWs grown homoepitaxially on (1-100) and (0001) GaN,” *J. Cryst. Growth*, vol. 251, no. 1–4, p. 487, 2003.

[91] T. Koida *et al.*, “Improved quantum efficiency in nonpolar (1120) AlGaN/GaN quantum wells grown on GaN prepared by lateral epitaxial overgrowth,” *Appl. Phys. Lett.*, vol. 84, no. 19, p. 3768, 2004.

[92] L. Rigutti *et al.*, “Origin of energy dispersion in Al(x)Ga(1 − x)N/GaN nanowire quantum discs with low Al content,” *Phys. Rev. B*, vol. 82, no. 23, p. 235308, 2010.

[93] T. Nakaoka, S. Kako, and Y. Arakawa, “Unconventional quantum-confined Stark effect in a single GaN quantum dot,” *Phys. Rev. B*, vol. 73, p. 121305(R), 2006.

[94] G. M. O. Hönig, “Mehrteilchenzustände in Halbleiter-Quantenpunkten,” Technischen Universität Berlin, 2015.

[95] G. Hönig *et al.*, “Identification of electric dipole moments of excitonic complexes in nitride-based quantum dots,” *Phys. Rev. B*, vol. 88, no. 4, p. 45309, 2013.

[96] J. Pal, G. Tse, V. Haxha, M. A. Migliorato, and S. Tomić, “Second-order piezoelectricity in wurtzite III-N semiconductors,” *Phys. Rev. B*, vol. 84, no. 8, p. 85211, Aug. 2011.

[97] J. Pal, G. Tse, V. Haxha, M. A. Migliorato, and S. Tomić, “Erratum: Second-order piezoelectricity in wurtzite III-N semiconductors [Phys. Rev. B 84, 085211 (2011)],” *Phys. Rev. B*, vol. 84, no. 8, p. 159902(E), 2011.

[98] P. K. Kandaswamy *et al.*, “GaN/AlN short-period superlattices for intersubband optoelectronics: A systematic study of their epitaxial growth, design, and performance,” *J. Appl. Phys.*, vol. 104, no. 9, 2008.

[99] M. Tchernycheva *et al.*, “Systematic experimental and theoretical investigation of intersubband absorption in GaN⁄AlN quantum wells,” *Phys. Rev. B*, vol. 73, no. 12, pp. 1–11, 2006.

[100] N. Grandjean, B. Damilano, and J. Massies, “Group-III nitride quantum heterostructures grown by molecular beam epitaxy,” *J. Phys. Condens. Matter*, vol. 13, pp. 6945–6960, 2001.

[101] L. Lahourcade *et al.*, “Interband and intersubband optical characterization of semipolar (1122)-oriented GaN/AlN multiple-quantum-well structures,” *Appl. Phys. Lett.*, vol. 93, no. 11, 2008.

[102] J. Müßener *et al.*, “Bias-Controlled Optical Transitions in GaN/AlN Nanowire Heterostructures,” *ACS Nano*, vol. 11, no. 9, pp. 8758–8767, 2017.

[103] O. Brandt, C. Pfüller, C. Chèze, L. Geelhaar, and H. Riechert, “Sub-meV linewidth of excitonic luminescence in single GaN nanowires: Direct evidence for surface excitons,” *Phys. Rev. B - Condens. Matter Mater. Phys.*, vol. 81, no. 4, pp. 1–7, 2010.

[104] B. Jenichen, O. Brandt, C. Pfueller, P. Dogan, M. Knelangen, and A. Trampert, “Macro- and micro-strain in GaN nanowires on Si(111),” *Nanotechnology*, vol. 22, p. 295714, 2011.

[105] M. Arita, F. Le Roux, M. J. Holmes, S. Kako, and Y. Arakawa, “Ultraclean Single Photon Emission from a GaN Quantum Dot,” *Nano Lett.*, vol. 17, no. 5, pp. 2902–2907, 2017.

[106] J. Richters, “Optische Eigenschaften von ZnO-Nanodrähten: Einfluss von Oberflächenbehandlungen und hohen Anregungsdichten,” Universität Bremen, 2010.

[107] S. K. Schlichting, “Einfluss der Dotierung auf die optischen und strukturellen Eigenschaften in Nanodrähten,” Technischen Universität Berlin, 2014.

[108] Z. C. Feng *et al.*, “Optical and structural investigation on InGaN/GaN multiple quantum well light-emitting diodes grown on sapphire by metalorganic chemical vapor deposition,” *SPIE*, vol. 6337, 2006.

[109] A. Satake, Y. Masumoto, T. Miyajima, T. Asatsuma, F. Nakamura, and M. Ikeda, “Localized exciton and its stimulated emission in surface mode from single-layer InxGa1-xN,” *Phys. Rev. B*, vol. 57, no. 4, pp. R2041–R2044, 1998.

[110] H. Wang *et al.*, “Influence of excitation power and temperature on photoluminescence in InGaN/GaN multiple quantum wells,” *Opt. Express*, vol. 20, no. 4, p. 3932, 2012.

[111] E. Redondo and A. Ojeda, “Influence of defects on the electrical and optical characteristics of blue light-emitting diodes based on III – V nitrides,” *J. Appl. Phys.*, vol. 81, no. 5, pp. 2442–2444, 2001.

[112] T. Lin, H. C. Kuo, X. D. Jiang, and Z. C. Feng, “Recombination Pathways in Green InGaN/GaN Multiple Quantum Wells,” *Nanoscale Res. Lett.*, vol. 12, no. 1, p. 137, 2017.

[113] Y. H. Cho *et al.*, “‘S-shaped’ temperature-dependent emission shift and carrier dynamics in InGaN/GaN multiple quantum wells,” *Appl. Phys. Lett.*, vol. 73, no. 10, pp. 1370–1372, 1998.

[114] F. Schuster *et al.*, “Self- Assembled GaN Nanowires on Diamond,” *Nano Lett.*, vol. 12, pp. 2199–2204, 2012.

[115] M. Shahmohammadi *et al.*, “Enhancement of Auger recombination induced by carrier localization in InGaN/GaN quantum wells,” *Phys. Rev. B*, vol. 95, no. 12, 2017.

[116] A. Kaschner, T. Lüttgert, H. Born, A. Hoffmann, A. Y. Egorov, and H. Riechert, “Recombination mechanisms in GaInNAs/GaAs multiple quantum wells,” *Appl. Phys. Lett.*, vol. 78, no. 10, pp. 1391–1393, 2001.

[117] J. Bai, T. Wang, and S. Sakai, “Influence of the quantum-well thickness on the radiative recombination of InGaN/GaN quantum well structures,” *J. Appl. Phys.*, vol. 88, no. 2000, p. 4729, 2000.

[118] H. Schömig, S. Halm, A. Forchel, G. Bacher, J. Off, and F. Scholz, “Probing Individual Localization Centers in an InGaN/GaN Quantum Well,” *Phys. Rev. Lett.*, vol. 92, no. 10, 2004.

[119] S. F. Chichibu *et al.*, “Impact of internal electric field and localization effect on quantum well excitons in AlGaN/GaN/InGaN light emitting diodes,” *Phys. Status Solidi Appl. Res.*, 2001.

[120] T. Lin, Z. R. Qiu, J. R. Yang, L. W. Ding, Y. H. Gao, and Z. C. Feng, “Investigation of photoluminescence dynamics in InGaN/GaN multiple quantum wells,” *Mater. Lett.*, vol. 173, pp. 170–173, 2016.

[121] V. Liuolia, S. Marcinkevičius, Y. Da Lin, H. Ohta, S. P. Denbaars, and S. Nakamura, “Dynamics of polarized photoluminescence in m-plane InGaN/GaN quantum wells,” *J. Appl. Phys.*, vol. 108, no. 2, 2010.

[122] M. Furis, A. N. Cartwright, H. Wu, and W. J. Schaff, “Room-temperature ultraviolet emission from GaN/AlN multiple-quantum-well heterostructures,” *Appl. Phys. Lett.*, vol. 83, no. 17, pp. 3486–3488, 2003.

[123] S. F. Chichibu, T. Azuhata, H. Okumura, A. Tackeuchi, T. Sota, and T. Mukai, “Localized exciton dynamics in InGaN quantum well structures,” *Appl. Surf. Sci.*, vol. 190, no. 1–4, pp. 330–338, 2002.

[124] C. Gourdon and P. Lavallard, “Exciton Transfer between Localized States in CdS(1-x)Se(x) Alloys,” *phys. stat. sol.*, vol. 153, no. 2, pp. 641–652, 1989.

[125] C. Gourdon, P. Lavallard, S. Permogorov, A. Reznitsky, Y. Aaviksoo, and Y. Lippmaa, “Picosecond Time-Resplved Luminescence of Localized Excitons in CdS(1-x)Se(x),” *J. Lumin.*, vol. 39, pp. 111–116, 1987.

[126] C. Gourdon and P. Lavallard, “Exciton Transfer Between Localized States In CdS(1-x)Se(x) Alloys: Time-Resolved Photoluminescence And Theoretical Models,” *J. Cryst. Growth*, vol. 101, pp. 767–772, 1990.

[127] P. Lefebvre *et al.*, “Recombination dynamics of free and localized excitons in GaN/Ga0.93Al0.07N quantum wells,” *Phys. Rev. B*, vol. 57, no. 16, pp. R9447–R9450, 1998.

[128] Y. Narukawa, “Recombination dynamics of localized excitons,” *Phys. Rev. B*, vol. 55, no. 4, pp. 1938–1941, 1997.

[129] Y. Zhang *et al.*, “Stokes shift in semi-polar (11-22) InGaN/GaN multiple quantum wells,” *Appl. Phys. Lett.*, vol. 108, no. 3, p. 31108, 2016.

[130] K. Okamoto, I. Niki, A. Scherer, Y. Narukawa, T. Mukai, and Y. Kawakami, “Surface plasmon enhanced spontaneous emission rate of InGaNGaN quantum wells probed by time-resolved photoluminescence spectroscopy,” *Appl. Phys. Lett.*, vol. 87, no. 7, pp. 1–4, 2005.

[131] F. Le Roux, K. Gao, M. Holmes, S. Kako, M. Arita, and Y. Arakawa, “Temperature dependence of the single photon emission from interface-fluctuation GaN quantum dots,” *Sci. Rep.*, vol. 7, no. 1, p. 16107, 2017.

[132] A. Lochmann *et al.*, “Electrically pumped, micro-cavity based single photon source driven at 1GHz,” *Electron. Lett.*, vol. 45, no. 11, p. 566, 2009.

[133] M. Binder *et al.*, “Identification of nnp and npp Auger recombination as significant contributor to the efficiency droop in (GaIn)N quantum wells by visualization of hot carriers in photoluminescence,” *Appl. Phys. Lett.*, vol. 103, no. 7, 2013.

[134] J. Iveland, L. Martinelli, J. Peretti, J. S. Speck, and C. Weisbuch, “Direct measurement of auger electrons emitted from a semiconductor light-emitting diode under electrical injection: Identification of the dominant mechanism for efficiency droop,” *Phys. Rev. Lett.*, vol. 110, no. 17, pp. 1–5, 2013.

[135] B. Galler *et al.*, “Experimental determination of the dominant type of auger recombination in InGaN quantum wells,” *Appl. Phys. Express*, vol. 6, no. 11, pp. 1–5, 2013.

[136] M. R. Krames *et al.*, “Status and Future of High-Power Light-Emitting Diodes for Solid-State Lighting,” *J. Disp. Technol.*, vol. 3, no. 2, pp. 160–175, Jun. 2007.

[137] F. Nippert *et al.*, “Determination of recombination coefficients in InGaN quantum-well light-emitting diodes by diodes by small-signal time-resolved photoluminescence,” *Jpn. J. Appl. Phys.*, vol. 55, p. 05FJ01, 2016.

[138] J. Piprek, “Efficiency droop in nitride-based light-emitting diodes,” *Phys. Status Solidi Appl. Mater. Sci.*, vol. 207, no. 10, pp. 2217–2225, 2010.

11 List of figures

Figure 2.1: Schematic illustration of a Ga-polar wurtzite crystal structure including Ga or Al atoms (positively charged, red), N atoms (negatively charged, blue), lattice constants a and c, the material specific internal lattice parameter u, the unit cell (green), a-plane, m-plane, c-plane, ABAB stacking and tetrahedron. 15
Figure 2.2: Double tetrahedrons of the wurtzite crystal structure including Ga or Al ions (positively charged, red), N ions (negatively charged, blue) and the material specific internal lattice parameter u. Coordinates for orientation: z-axis corresponds to the growth direction [0001] (c-axis). Left: ideal double tetrahedron, middel: compressively (x-y-plane) strained double tetrahedron (piezoelectric polarization), right: intrinsic deviation from the ideal double tetrahedron (constitutes the spontaneous polarization). 16
Figure 2.3: Illustration of a wurtzite crystal structure with Ga or Al ions (positively charged, red), N ions (negatively charged, blue), lattice constants a and c, central metal atom (black framed), nearest neighbors nitrogen atoms (orange framed) and second nearest neighbors (green framed). 17
Figure 2.4: Schematic illustration of a GaN QW in an AlN matrix without surface charges a), with surface charges b) illustrating the QCSE and the screening of the QCSE through a large number of charge carriers c). 19
Figure 2.5: Band structure for a) GaN and b) AlN depicted with the energy gaps for the A-valley E_A, the Γ-valley E_g, the M-L valley E_{M-L} and the energy splitting in the valance bands A, B and C. The energy values are given in Table 2.4 [60]–[62]. 23
Figure 3.1: Schematic sketch of the µ-PL set-up. 26
Figure 3.2: Schematic sketch of the ns-range TRPL set-up. 27
Figure 3.3: Schematic sketch of the µs-range TRPL set-up. 28
Figure 4.1: Left side: Conventional GaN/AlN QD structure grown along the most natural growth direction [0001]. 2D scan of the layer sequence a), a contour plot showing the sum of the piezo- and pyroelectric potential revealing a gradient illustrated by the color change from yellow to black inside the QD b), and a band edge scan through the QD center with the typical tilt c). The overlap of the electron (blue) and hole (red) wave functions as a measure of the transition probability in the QD is green. The potential gradient inside the QD b) is responsible for the charge carrier separation c) resulting in a reduced transition probability for conventional QDs. Right side: IFGARD GaN/AlN QD structure grown along the most natural growth direction [0001]. 2D scan of the layer sequence d), a contour plot showing the sum of the piezo- and pyroelectric potential exhibiting a constant electric potential illustrated by the homogeneous purple color inside the IFGARD QD e), and a band edge scan through the IFGARD QD center with the flat band edges f) resulting in an immense increase of the transition probability due to the increased overlap (green) of the electron (blue) and hole (red) wave-function [45]. 31
Figure 4.2: The sum of the piezo- and pyroelectric potential across an IFGARD QD for different layer dimensions in comparison to the conventional case without IFGARD (dashed line). The height of the GaN QD is kept constant at 3 nm, the AlN barrier thickness was varied symmetrically (red = blue number) and asymmetrically including a “stack inversion” [45]. 33
Figure 4.3: Comparison of an IFGARD QW with an electronic analogon – stacked, plate-type capacitors with distances t, h and b, and the permittivity ε. The distances between the capacitor plates are equivalent to the top barrier of 1 nm, the QW thickness of 2 nm and the

bottom barrier of 1 nm. The interface charges, resulting from the polarization, are marked with positive (+, red) and negative (-, black) mathematic signs. Green arrows represent the corresponding electric fields inside the capacitor plates, showing a field annihilation within the inner plates (QW). 34
Figure 4.4: Illustration of the IFGARD stack sequence a) in comparison to the conduction- and valence band edges b). In the IFGARD sequence a), grown along the most natural c- axis, the interface charges caused by the crystal polarization are marked with positive (+, red) and negative (-, black) signs. 35
Figure 4.5: Applicability of the IFGARD for multiple QWs with fixed or variable QW composition showing the universal validity of the IFGARD and the possibility to create potential landscapes by composition variation d). 37
Figure 5.1: Schematic sketches of the NWs with AlN barrier thicknesses of 1 nm a) and 4 nm c), each with 4-nm-thick GaN NDs. Arithmetic signs (red +, blue -) mark the positions of interface space charges. b) shows the respective band structure for 1-nm-thick barriers illustrating the flat conduction and valance band edges (black) in comparison to a conventional structure without guard layers (red), which exhibits band banding due to the QCSE (calculated with the NextNano software) [45]. d) to k) show SEM images of samples with AlN barrier thicknesses of 6 nm [d), e)], 4 nm [f), g)], 2 nm [h), i)] and 1 nm [j), k)] each with a ND thickness of 4 nm. The SEM images illustrate the changing cone-shape angle α and the coalescence of some NWs. 40
Figure 6.1: Comparison of µ-PL spectra for all investigated samples at 15 µW excitation power. In all samples, the dominant GaN ND luminescence is accompanied by the GaN-guard-layer luminescence (marked by the dashed, blue line), which divides the samples series into the so called QCSE regime and the confinement regime. 44
Figure 6.2: M Multiple phonon replicas are visible for the 1-nm-thick AlN barriers sample within the QCSE regime only. The existence of multiple LO-phonon replicas indicates built-in excitonic electric dipole moments in the QCSE regime samples. 46
Figure 6.3: Comparison between numeric (black with IFGARD, red without IFGARD) and experimental data (green) illustrating the ND emission energies dependence on the ND thickness. Note, that the numeric “IFGARD” data was calculated for infinite quantum wells, hence, the built-in field strength was perfectly shielded (zero field strength). Whereas the calculated values for structures without IFGARD show an approximately linear trend crossing the GaN guard layer luminescence at 3.47 eV, the predicted IFGARD ND emission energies converge against the GaN guard layer luminescence. The Theoretical predictions for the IFAGRD are in perfect accordance to the experimental data recorded for the samples within the confinement regime–hence, these samples are without any built-in electric field. 47
Figure 6.4: Approximation of the electric field strength for the QCSE regime samples showing the conduction and valance band edges for one ND in the z-direction with the ND thickness $l_{QND,}$ the emission energy of the ND E_{ND}, the energy of the GaN guard layer E_{GaN} and the potential drop ΔE, besides, the equation for a homogeneous electric field in a plate type capacitor. 50
Figure 6.5: Estimated electric field strength vs. barrier thickness showing a decreasing electric field strength with a decreasing barrier thickness in the QCSE regime. 51
Figure 6.6: STEM image of three coalesced NWs with 6-nm-thick AlN barriers and 4-nm-thick GaN NDs (a). b) shows a comparison of NWs with 6-nm- and 1-nm-thick barriers with 4-nm-

thick NDs each. Marked are the GaN guard layer, the GaN NDs (bright), the AlN barriers (dark), and the AlN shell. 52
Figure 6.7: Systematically measure of the NDs thickness along one NW for the 6-nm and 1-nm-thick AlN barriers. 53
Figure 6.8: Color coded Al concentration dark red for “100 % Al” representing pure AlN, dark blue for “-20 % Al", while 0 % represents pure GaN) in a section of a NW with nominally 6-nm-thick AlN barriers. 55
Figure 6.9: Impact of 1 (gray) and 2 (yellow) ML fluctuations on the ND emission peak. The values for the ML fluctuations stem from the numeric calculations in Figure 6.3. 57
Figure 6.10: Cross section through a NW illustrating the energy vs. radius of the NW. The valence and conduction band as well as the fermi energy, the surface and the sidewall of the NW is sketched. The crystal lattice symmetry break at the sidewall leads to surface states within the bandgap, highlighted in green. The electrons (blue) and holes (red) occupy either the ND conduction band and valance band states with the emission energy E_{ND} or the electrons occupy the surface states within the bandgap (green) and recombine with a hole in the valance band with the emission energy E_{SX}. 59
Figure 6.11: Comparison of the sample spectra at low (black) and high (red) excitation powers with normalized intensities. The dashed area decreases for high excitation powers relative to the high energy sides of the peaks. This can be explained by a saturated filling of the surface states with excited charge carriers. 60
Figure 6.12: Influence of the different broadening mechanisms – normal ML fluctuation (gray), surface states and QD like ML fluctuation (blue) – on the FWHM. The black squares represent the measured FWHM and the red dots the calculated FWHM caused by 1 ML of normal ML fluctuation. The green squares mark the deviation between the experimental and calculated values representing the fraction of the broadening caused by QD-like fluctuations and surface states. 62
Figure 6.13: Power dependent µ-PL spectra for the QCSE (left column) and the confinement regime (right column) samples. 63
Figure 6.14: ND emission peak positions are plotted for excitation powers between 0.035 µW and 500 µW. The total emission energy shift between the lowest (min) and highest (max) excitation power is given on the right, vertical axis (blue) representing the achieved polarization field screening by excited charge carriers for the samples within the QCSE regime only. 64
Figure 6.15: FWHM vs. excitation power for the 6-nm and 1-nm-thick AlN barriers samples in the QCSE regime and the 1-nm-thick GaN ND sample in the confinement regime showing three different trends over excitation power. 65
Figure 6.16: Integrated intensity vs. excitation power for the QCSE and confinement regime. The linear dependency in this double logarithmic plot proves the dominance of radiative recombination processes in all of the samples. 66
Figure 6.17: Integrated intensity vs. excitation power for the confinement regime samples. The integrated intensity is weighted by the ND thicknesses. 68
Figure 6.18: Temperature dependent PL for the confinement regime samples and the 4-nm-thick GaN NDs sample with 1-nm-thick AlN barriers of the QCSE regime. 70
Figure 6.19: Emission energy peak shift with temperature for the confinement regime samples and the 4-nm-thick GaN NDs with 1-nm-thick AlN barriers of the QCSE regime. ... 71

Figure 6.20: Illustration of the emission energy vs. temperature (squares) accompanied by the FWHM (blue tube) and the Varshni shift fit (pink, dashed line) for the confinement regime samples and the 4-nm-thick GaN NDs with 1-nm-thick AlN barriers representative for the QCSE regime. Furthermore, the absolute offsets at the ordinate between the extended Varshni shift fits and the experimental values are depicted in red. 72
Figure 6.21: Integrated intensity as a function of temperature for all samples comprising 1-nm-thick AlN barriers. The decreased excitation volume of thinner NDs is accounted for in the right plot with a logarithmic intensity scaling. 75
Figure 6.22: Integrated Intensity normalized to the individual maximum values as a function of Temperature for all samples with 1-nm-thick AlN barriers. An intensity drop to 50 % is marked by the green line. 76
Figure 6.23: Comparison between the decay transients taken at the maximum (blue), the low (red) and high (black) energy side of the 1-nm-thick NDs luminescence peak. While the low energy side follows a biexponential decay process (green fits), the high energy side needs to be described by a triexponential decay process (purple fit). 77
Figure 6.24: Decay times τ_1, τ_2, and τ_3 as well as photon count fractions as a function of temperature for the 1-nm thick NDs with 1-nm thick AlN barriers at the low energy side (top), at the luminescence peak maximum (center), and at the high energy side (bottom). 78
Figure 6.25: Direct comparison of the decay times τ_1, τ_2, and τ_3 as a function of temperature depending on the different 1-nm-thick ND luminescence positions (low energy side-green, maximum-red, and high energy side-black). As illustrated in Figure 6.23, τ_3 only appears on the high energy side. τ_1 and τ_2 are present at all positions showing different trends. 79
Figure 6.26: a) Evolution of the decay times τ_1, τ_2, and τ_3 along the 1-nm-thick NDs' luminescence (green) for low and high excitation powers. b) Fractions of the total counts A_1, A_2 and A_3 for the decay times τ_1, τ_2, and τ_3, respectively. c) and d) show in principle the same as a) and b) with the difference, that τ_3 is subtracted from τ_1 and A_3 is summed to A_1 to demonstrate a refilling by τ_3. 83
Figure 6.27: Decay times vs. emission energy for the 1-nm-thick NDs, at top, the 2-nm-thick NDs, at center, and the 3-nm-thick NDs, at bottom within the confinement regime. The abrupt increase of τ_2 reduces for the 2-nm-thick NDs and disappears for the 3-nm-thick NDs, while the energetic position of the occurrence of $\tau_3$shifts to lower energies relative to the emission peak maxima demonstrating the decreased influence of the ML fluctuations on the ND luminescence broadness. 85
Figure 6.28: Decay time τ_1 (black) and τ_2 (red) along the 2 nm AlN-4 nm GaN NDs luminescence (green spectra) for high (squares) and low (stars) excitation powers, a) and the same data points artificially shifted to compensate the charge carrier screening of the emission energy, b). 87
Figure 6.29: Determination of the localization depths within the 4-nm-thick GaN NDs with 2-nm-thick AlN barriers by fitting the decay times τ_1 and τ_2 with a weak exciton localization model [119] (equation 6.3). The fits were performed on the decay times τ_1 and τ_2 for low and high excitation powers separately, delivering the same localization depth for τ_1 but different depths for τ_2, which shows that the origins of the two recombinations are fundamentally different. 90
Figure 6.30: Different recombination pathways in a 1-nm-thick ND for the low a) and high b) energy sides of the ND luminescence peak as well as for the low energy side at higher temperatures c). The ND state bands (gray) and the QD-like single electron state together

with QD-like multiple hole states due to the energetically close A, B valance bands in combination with the small effective hole mass. While at the low energy side two recombination processes, τ_1 and τ_2 originating from the normal and QD-like ML fluctuations are detectable, on the high energy side three recombination processes are determined. At the high energy side, a combined recombination and relaxation process τ_r from the primary ND into ML fluctuations and QD-like fluctuations is assumed leading to τ_3. T Charge carriers in the normal ML fluctuations on the energetically lower side can be thermally excited fluctuate, which is not possible for charge carriers in QD-like ML fluctuation as no free states exist. 93
Figure 6.31: Time-resolved photoluminescence (TRPL) transients show the correlation between the decreasing exciton decay times for reduced electric field strengths (chapter 6.1.1) in the equally sized NDs of the QCSE regime samples (a), besides the fast, constant decay times in absence of built-in fields within the differently sized NDs of the confinement regime samples. The exciton lifetime fits results (see equation 6.1) are noted in the respective legends. Lifetimes with significantly more counts are bold. All TRPL transients displayed here, are recorded at the ND luminescence maxima at low temperatures but with high excitation power. 95
Figure 6.32: Direct comparison of the experimentally determined emission energies for the different ND samples in the confinement regime (black squares) and the QCSE regime (red dots) to numeric results for GaN/AlN IFGARD quantum wells (black line) exhibiting totally shielded polarization fields (built-in field strength = 0 MV/cm). Published values for pure GaN QWs with nonpolar growth directions are included as greenish squares [29], [89]–[91], [101] and confirm the converging trend that is predicted for GaN QWs without built-in fields. While the conventionally grown [0001], fully polar GaN/AlN QWs [98], [99], [101] (reddish triangles) emit at much lower emission energies for well widths exceeding 1 nm. Even doping in the order of $5 \cdot 1019cm3$ (red crosses) does not significantly alter the emission energies of the polar GaN/AlN QWs. 98
Figure 7.1: This Figure summarizes the most important results used for the proof of the successful tuning and annihilation of the QCSE in the investigated IFGARD nanodiscs (NDs) within a plot of the nanodisc emission energies vs. the barrier and nanodisc thicknesses separating the confinement regime, marked by black squares and the QCSE regime (red dots) from each other. It shows the determined, residual built-in electric field strengths (green values), the exciton confinement energies (black values), and the dominant decay times (orange values). Additionally, the geometric nanowire structure in the respective pure confinement or QCSE regime are sketched, including the comparison with numeric calculations of QWs without or full (black vs. pink) built-in electric fields..... 100

12 List of tables

Table 2.1: Lattice parameters a and c and internal lattice parameter u of AlN and GaN [51]. 15
Table 2.2: Elastic stiffness coefficients in GPa for wurtzite AlN and GaN [40], [56]. 21
Table 2.3: Pyroelectric polarization in C/m^2 and piezoelectric modules $e_{33,\ 31,\ 15}$ in C/m^2 for wurtzite AlN and GaN [40]. 22
Table 2.4: Band structure relevant energies in eV for the A-valley E_A, the Γ-valley E_g, the M-L valley $E_{M\text{-}L}$ and the energy splitting in the valance band resulting from the crystal field E_{cf} and spin-orbit interaction E_{so} for GaN and AlN [40], [53], [61] [40], [62]. 23
Table 5.1: List of samples with the sample description, the sample number and the corresponding barrier (t = b) and QW thicknesses. 39
Table 5.2: NW diameter and length scales for different AlN thicknesses and a constant GaN ND thickness of 4 nm 42
Table 6.1: Energetic influence of 1 and 2 ML fluctuations on the ND luminescence estimated from numeric calculations (compare Figure 6.3) and applied to the experimental data. 56
Table 6.2: F for all samples. 69
Table 6.3: Different values obtained from the temperature dependent PL for all samples comprising 1nm-thick AlN barriers 74